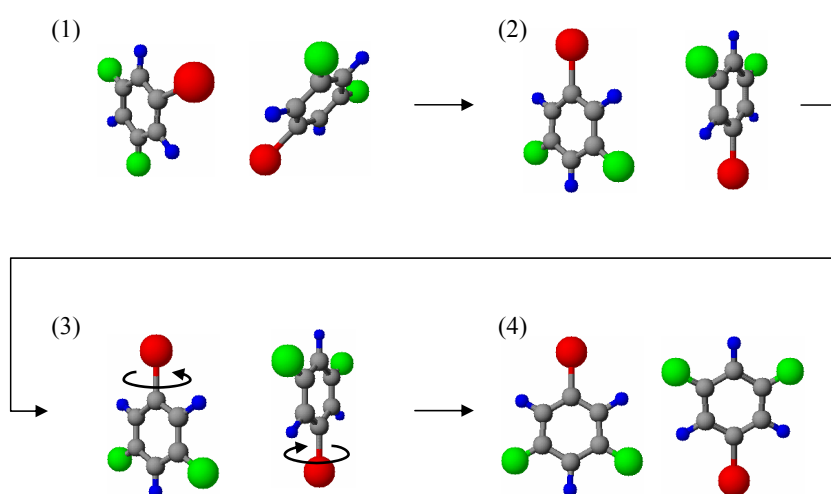


Control of molecular rotation using pulsed lasers

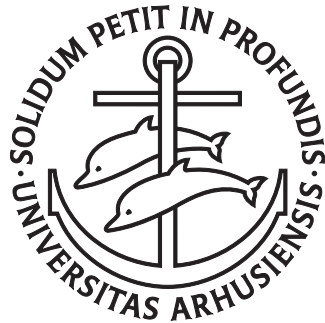


PhD thesis

Simon Stenfeldt Viftrup
Department of Physics and Astronomy
University of Aarhus

August 2007

Control of molecular rotation using pulsed lasers



PhD thesis

Simon Stenfeldt Viftrup
Department of Physics and Astronomy
University of Aarhus

August 2007

Preface

This thesis has been submitted to the Faculty of Science at the University of Aarhus, in order to fulfill the requirements for the PhD degree. The work presented has been carried out at the Department of Physics and Astronomy in the years 2003 to 2007 under the supervision of Henrik Stapelfeldt from the Department of Chemistry.

Acknowledgements

First and foremost I would like to thank Henrik Stapelfeldt for being an excellent supervisor. He has always been helpful and encouraging, despite being increasingly busy the last years.

During my eight years at the University of Aarhus I have been fortunate to work with many colorful and brilliant people, however, one person stands out. Anders Mouritzen, with his tranquil manner, has always been a great inspiration, a helpful friend and in general a pleasure to work with.

For good company and fruitful discussions in the lab I would like to thank (in order of appearance): Mikael Poulsen, Christer Bisgaard, Emmanuel Péronne, Tine Ejdrup, Lotte Holmegaard and Vinod Kumarappan. With these people many dark late hours have been spent in the basement during acquisition of the results presented in this thesis. The invaluable laser support from Jan Thøgersen is also greatly appreciated.

I would like to thank the technical staff at the Institute of Physics and Astronomy, in particular Torben Thomsen and Karsten Rasmussen for great guidance and support. I am also grateful for the wonderful items that the mechanical workshop at the Department of Chemistry has constructed for the lab. The work from the skilled Per Strand is especially memorable.

Our collaborators Tamar Seideman and Edward Hamilton from Northwestern University, IL, USA are greatly acknowledged for improving my understanding of alignment beyond the boundary of the experiments.

I acknowledge Thomas Poulsen, from the Center for Catalysis at the Department of Chemistry, for his indispensable help with the synthesis of a new exotic molecule. Mikael Johansson, from the Department of Chemistry, is also acknowledged for his speedy structure and polarizability calculations.

Finally, I would like to thank my friends, my girlfriend and my family for showing interest in my work and my well-being and for supporting me through these hectic years.

List of Publications

The work presented in this thesis has led to the following publications:

- I *Nonadiabatic alignment of asymmetric top molecules: Rotational revivals*
M. D. Poulsen, E. Péronne, H. Stapelfeldt, C. Z. Bisgaard, S. S. Viftrup, E. Hamilton and T. Seideman. *J. Chem. Phys.* **121**, 783 (2004).
- II *Observation of enhanced field-free molecular alignment by two laser pulses*
C. Z. Bisgaard, M. D. Poulsen, E. Péronne, S. S. Viftrup and H. Stapelfeldt. *Phys. Rev. Lett.* **92**, 173004 (2004).
- III *Alignment of symmetric top molecules by short laser pulses*
E. Hamilton, T. Seideman, T. Ejdrup, M. D. Poulsen, C. Z. Bisgaard, S. S. Viftrup and H. Stapelfeldt. *Phys. Rev. A* **72**, 043402 (2005).
- IV *Alignment enhancement of a symmetric top molecule by two short laser pulses*
C. Z. Bisgaard, S. S. Viftrup and H. Stapelfeldt. *Phys. Rev. A* **73**, 053410 (2006).
- V *Role of rotational temperature in adiabatic molecular alignment*
V. Kumarappan, C. Z. Bisgaard, S. S. Viftrup, L. Holmegaard and H. Stapelfeldt. *J. Chem. Phys.* **125**, 194309 (2006).
- VI *Control of rotational wave-packet dynamics in asymmetric top molecules*
L. Holmegaard, S. S. Viftrup, V. Kumarappan, C. Z. Bisgaard, H. Stapelfeldt, E. Hamilton and T. Seideman. *Phys. Rev. A* **75**, 051403(R) (2007).
- VII *Aligning molecules with long or short laser pulses*
V. Kumarappan, S. S. Viftrup, L. Holmegaard, C. Z. Bisgaard, H. Stapelfeldt. Accepted by *Physica Scripta*.
- VIII *Holding and spinning molecules in space*
S. S. Viftrup, V. Kumarappan, S. Trippel, H. Stapelfeldt, E. Hamilton and T. Seideman. Submitted to PRL (2007).
- IX *3-dimensional alignment by the combination of a long and a short laser pulse*
S. S. Viftrup, V. Kumarappan, C. Z. Bisgaard, H. Stapelfeldt, E. Hamilton and T. Seideman. In preparation.

In addition the author participated in the following work:

- X *Photoelectron angular distributions from fixed in space CS₂ molecules*
V. Kumarappan, L. Holmegaard, S. S. Viftrup, H. Stapelfeldt. In preparation.

Outline

- Chapter 1** A brief introduction to alignment is given and my contributions to the field are outlined.
- Chapter 2** The theory of laser-induced molecular alignment is outlined. The laser-molecule interaction is described quantum mechanically and a classical model for alignment is presented.
- Chapter 3** The experimental setup and the detection system is described. A newly implemented vacuum system and ancillary electronics and software is explained in detail.
- Chapter 4** Experimental results on nonadiabatic alignment are presented. Alignment revivals for both symmetric top and asymmetric top molecules are shown and control of rotation of an asymmetric top molecules is demonstrated.
- Chapter 5** In this chapter we show experimentally that the alignment by a single non-adiabatic alignment pulse can be significantly enhanced by using two properly timed pulses.
- Chapter 6** Experiments on very cold adiabatically aligned molecules are displayed. Alignment of all three molecular axis to space-fixed axis (three dimensional alignment) is demonstrated.
- Chapter 7** A new approach for three dimensional alignment, combining adiabatic and nonadiabatic alignment, is suggested and experiments revealing spinning molecules are presented.
- Chapter 8** Preliminary results indicating manipulation of internal rotation are shown and discussed.

Contents

1	Introduction	1
2	Theory of alignment	5
2.1	Adiabatic alignment	6
2.1.1	Pendular states	7
2.2	Nonadiabatic alignment	8
2.2.1	δ -kick model	8
2.2.2	Quantum mechanical description	9
3	Experimental setup	11
3.1	Vacuum system	11
3.2	Optical setup	15
3.2.1	Pump pulses	16
3.2.2	Probe pulses	17
3.2.3	Beam overlap and pulse timing	19
3.3	Electronics	20
3.4	Data acquisition and analysis	22
4	Experimental Results I: Nonadiabatic alignment	25
4.1	Early time alignment dynamics	25
4.2	Long time alignment dynamics: Rotational revivals	29
4.2.1	Symmetric top molecule	29
4.2.2	Asymmetric top molecule	32

5	Experimental Results II: Two-pulse nonadiabatic alignment	39
5.1	Initial experiments on iodobenzene	40
5.2	Detailed experiments on <i>tert</i> -butyliodide	41
6	Experimental Results III: Adiabatic Alignment	51
6.1	One Dimensional Adiabatic Alignment	51
6.2	Three Dimensional Adiabatic Alignment	56
7	Experimental Results IV: 3D alignment by combining adiabatic and non-adiabatic alignment	65
7.1	Preliminary experiments on 3,4-dibromothiophene	66
7.2	Experiments on 3,5-difluoroiodobenzene	69
7.2.1	Early dynamics	70
7.2.2	3D alignment revivals	72
7.2.3	Theoretical calculation	73
7.2.4	Importance of 1D alignment prior to the kick pulse	74
7.2.5	Kick pulse alignment dependency	78
7.2.6	Elliptically polarized Nd:YAG pulse	79
7.2.7	3D alignment comparison	80
8	Perspectives	83
9	Summary	91
A	Schematic drawing of the new vacuum system	93
B	LabVIEW	95
C	Determination of the rotational constants of 3,5-difluoroiodobenzene	101

CHAPTER 1

Introduction

The orientation of molecules influences essentially all bimolecular and photochemical reactivity. For bimolecular reactions this is apparent since molecules in general are not spherically symmetric. A classic example is the S_N2 reaction where relative molecular orientation play a deciding factor for the reactivity. The substitution of I with OH in methyl iodide [CH₃I] is an example for such a reaction:



The reaction rate is highest if the OH⁻ attacks methyl iodide along the C-I bond axis from the carbon end. Due to the high influence of molecular orientation in bimolecular and photochemical reactivity, development and application of techniques for controlling molecular orientation has been a topic of great importance and activity in molecular sciences for decades.

Two different techniques utilizing electrostatic fields have been used to control molecular orientation. In the hexapole focusing technique [1] a single rotational state is selected in a static electric field from a hexapole. Molecules in a single rotational state, with their angular momentum vector precessing in the applied electric field, will in general be oriented, however, the angular confinement of a single state can only be modest. Alternatively, in a parallel-plate capacitor like setup, molecules have been oriented by strong electrostatic fields. If the applied field is sufficiently strong, molecules with a permanent dipole moment will be forced into confined librational motion with their dipole moment preferentially pointing in the direction of the field. This approach is nicknamed "Brute force" orientation [2, 3]. In order for the interaction en-

ergy to be higher than the rotational energy, and thus obtain angular confinement, both of these methods require rotationally cold molecules and therefore demand supersonic expansion jets.

A significant advance in the ability to obtain orientational control of molecules was triggered in the mid 90s when it was realized that moderately intense electromagnetic fields from pulsed lasers can align molecules along axes fixed in space [4, 5]. The alignment results from interaction between the induced electric dipole moment and the laser field. Contrary to the static field approaches mentioned above the laser based approach is very general and applies to any nonspherical top molecule, since only an anisotropic polarizability is required [6, 7]. Due to the oscillatory nature of a laser field, the molecules are not oriented and only an axis is confined. Hence, opposed to orientation, no "head" versus "tail" order is established in laser induced alignment. The rapid progress in laser induced alignment techniques over the past ten years has broadened the scope of spatially oriented molecules from the original focus on chemical reaction dynamics to new applications such as ultrafast electron or x-ray imaging [8–10], extreme nonlinear optics [11, 12], molecular separation techniques [13], and femtosecond time-resolved photoelectron spectroscopy [14]. The vast majority of studies to date have focussed on linear molecules, but the growing range of applications of alignment in complex molecular systems is currently shifting attention to the nonlinear polyatomic domain, where complete control over the rotational motions requires one to go beyond alignment. In the limit of micron-sized particles, this task has already been accomplished by optical tweezer type techniques which allow mesoscopic objects to be held and rotated about any axis of choice [15].

My work in the Femtolab group started with studies of one dimensional alignment of symmetric and asymmetric top molecules, in particular the alignment dynamics observed long after the alignment pulse turn off [16–18]. Hereafter it turned towards developing and improving alignment techniques, specifically investigating new methods using two synchronized laser pulses to improve the alignment [19–21]. The last half of my ph.d. has concentrated on control of molecular rotation in asymmetric top molecules. By varying the fluence in a picosecond pulse, control over two different rotations has been achieved in a near prolate asymmetric top molecule [22]. At low fluence the rotation resembles that of a symmetric top molecule whereas at higher fluences a different rotation, unique to asymmetric tops, was observed. Access to control of a third molecular rotation was achieved by combining a nanosecond and a femtosecond laser pulse. By fixing one molecular axis to a space axis using the nanosecond pulse we were able to induce rotation of the molecule, about the fixed axis, with the femtosecond pulse. This technique not only opens up for angular confinement of all three molecular axis and isolation of a spinning like rotation, but also offers interesting possibilities for studying and controlling torsion of flexible molecules. Preliminary experiments on biphenyl has been undertaken and our findings suggest control of rotation about the internuclear axis connecting the two benzene rings. They also indicate

that the dihedral angle (the angle between the two phenyl planes) has been distorted in the interaction with the laser pulses.

CHAPTER 2

Theory of alignment

The interaction between a molecule and a nonresonant, nonionizing laser pulse is well described by the dipole interaction. Since the electric field of nearinfrared light oscillates much faster than the period of rotation for molecules the interaction with the permanent dipole moment averages to zero [4]. The induced dipole moment, however, oscillates with the field and the interaction is reduced to the polarizability interaction:

$$\hat{H}_{int} = -\frac{1}{2} \vec{\epsilon} \alpha \vec{\epsilon} \quad (2.1)$$

where $\vec{\epsilon} = \hat{\epsilon} \varepsilon(t) \cos(\omega t)$ is the electric field vector and α is the polarizability tensor of the molecule in space fixed coordinates. Due to molecular structure the polarizability of a molecule is in general anisotropic, and the induced dipole will therefore depend on the relative orientation between the molecule and the electric field. It is this orientational dependency that allows us, through the polarizability interaction, to manipulate molecular orientation.

The total rotational Hamiltonian of the molecule will be a sum of the interaction Hamiltonian and the field-free rotational Hamiltonian:

$$\hat{H}_{total} = \hat{H}_{int} + \hat{H}_{ff} = \hat{H}_{int} + \frac{\hat{J}_x^2}{2I_{xx}} + \frac{\hat{J}_y^2}{2I_{yy}} + \frac{\hat{J}_z^2}{2I_{zz}} \quad (2.2)$$

where x, y, z are molecule-fixed coordinates. There are two different regimes in laser induced alignment, identified by the duration of the interaction. When the laser pulse is long compared to molecular rotation, the molecules undergo adiabatic transition

from field-free states to field-dressed states. They will align during the interaction and return to their initial state afterwards. Alignment under these conditions is termed adiabatic alignment. By contrast, when the laser pulse is short compared to molecular rotation, a time-dependent rotational wave packet is induced and alignment will occur after the interaction with the pulse.

2.1 Adiabatic alignment

In adiabatic alignment the alignment laser pulse is turned on and off slowly compared to the natural rotational period(s) of the given molecule. According to the adiabatic theorem [23], molecules that are initially located in the n 'th eigenstate of the field-free Hamiltonian will be transferred to the n 'th eigenstate of the field-dressed Hamiltonian (Eq. (2.2)). The field-dressed states are directional superpositions of the field-free states and are termed pendular states since the aligned molecular axis, in a classical mechanics sense, librate around the direction of the applied field [4]. The molecular alignment will follow the intensity profile of the laser pulse and the molecules will return to their initial state after the interaction. Based on quantum mechanical calculations Ortigoso *et al.* [24] reported that complete adiabatic alignment behavior is expected with pulse durations of 5 times longer than the rotational period of the molecules. More recent studies by Torres *et al.* [25] predict adiabatic behavior already at pulse durations near that of the molecular rotational period.

For a linear or symmetric top molecule in a linearly polarized laser field the interaction potential is [26]:

$$\hat{H}_{int} = -\frac{1}{4} \varepsilon^2(t) [(\alpha_{\parallel} - \alpha_{\perp}) \cos^2 \theta + \alpha_{\perp}] \quad (2.3)$$

where α_{\parallel} and α_{\perp} is the polarizability along and perpendicular to the principal molecular symmetry axis, $\varepsilon^2(t)$ is the intensity of the laser pulse and θ is the polar Euler angle between the polarization axis of the laser field and the principal molecular symmetry axis (The Euler angles presented in this thesis follows the definitions of Zare [27]). For molecules where $\alpha_{\parallel} > \alpha_{\perp}$ this is a double well potential where the energy is minimized for $\theta = 0$ or π (see Fig. 2.1). The alignment will therefore be along the polarization axis of the laser field, however, the molecules are equally likely to point in either direction along this axis. Due to the adiabatic transition the occupation of the field-dressed states is the same as the initial rotational state distribution. Since the lowest lying pendular states are more confined than higher lying states the initial distribution, and hence the rotational temperature, is a critical alignment parameter [29]. The degree of alignment will depend on the initial rotational energy, the intensity of the laser pulse and the polarizability of the molecule.

For an asymmetric molecule, characterized by three distinct moments of inertia,

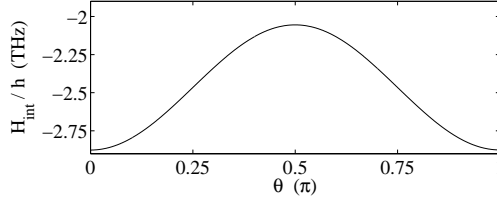


Figure 2.1: Interaction potential for methyl iodide at an intensity of $1 \times 10^{12} \text{ W/cm}^2$. Calculated from $\alpha_{\parallel} = 9.1 \text{ \AA}^3$ and $\alpha_{\perp} = 6.5 \text{ \AA}^3$ [28].

in a linearly polarized laser field the interaction is [7]:

$$\hat{H}_{int} = -\frac{1}{4} \varepsilon^2(t) [\sin^2 \theta (\alpha_{xx} \cos^2 \chi + \alpha_{yy} \sin^2 \chi) + \alpha_{zz} \cos^2 \theta] \quad (2.4)$$

where α_{ii} , $i = x, y, z$ are the components of the polarizability tensor along the principal molecular axes and χ is the Euler azimuthal angle about the molecular z -axis. For non perfectly aligned molecules ($\theta \neq 0, \pi$) rotation about the z -axis is not free and lowest energy is obtained by having the axis of second highest polarizability in the plane spanned by the molecular axis of highest polarizability and the polarization vector of the laser field.

When an asymmetric top molecule is placed in a elliptically polarized laser field the interaction will depend on all three Euler angles. The expression is rather involved and will not be shown here, rather the reader is referred to [30]. In general, the energy is minimized for molecules with their most polarizable axis aligned along the major polarization axis and the axis with second highest polarizability along the minor polarization axis. For rigid molecules the confinement of two axis will automatically result in confinement of the third.

2.1.1 Pendular states

Since the polarizability interaction, at the high intensities used in adiabatic alignment, cannot be regarded as perturbation, the time independent Schrödinger equation must be solved numerically to obtain the pendular states. With each pendular state written as a superposition of the field-free states

$$|\psi^i\rangle = \sum_n C_n |n\rangle \quad (2.5)$$

the time independent Schrödinger equation

$$(\hat{H}_{int} + \hat{H}_{ff})|\psi^i\rangle = E_{\psi^i}|\psi^i\rangle \quad (2.6)$$

can be solved numerically to find the expansion coefficients for each pendular state.

The expectation value of $\cos^2 \theta$ is a commonly used measure for characterizing the degree of alignment. With the pendular states at hand this value can be readily computed, however, if comparison with experiments is to be made, the initial state distribution must be accounted for. As the precise state distribution is usually unknown a Boltzmann distribution is often used as an approximation:

$$w_i(T_{rot}) = \frac{e^{-E_i/kT_{rot}}}{\sum_j e^{-E_j/kT_{rot}}}, \quad (2.7)$$

where E_i is the field-free energy of the i 'th initial state. The temperature averaged value of $\langle \cos^2 \theta \rangle$ can then be found:

$$\langle \cos^2 \theta \rangle_T = \sum_i w_i(T_{rot}) \langle \psi^i | \cos^2 \theta | \psi^i \rangle \quad (2.8)$$

2.2 Nonadiabatic alignment

Nonadiabatic alignment can be understood as the creation of a rotational wave packet through excitation of a broad superposition of rotational eigenstates [5]. The bandwidth of femtosecond lasers is sufficiently wide to coherently excite such a wave packet via a series of Raman transitions. Theoretically, the alignment dynamics is correctly described by numerical solution of the time dependent Schrödinger equation. I start, however, by introducing a simple classical model since it provides useful physical insight.

2.2.1 δ -kick model

A classical model for understanding the alignment dynamics after interaction with a short linearly polarized laser pulse (kick pulse) has been proposed by Averbukh and co-workers [31, 32]. If the pulse is very short compared to molecular rotation the molecules can be considered as stationary during the interaction. A linear molecule exposed to a linearly polarized laser pulse, will experience a torque due to the polarizability interaction (Eq. (2.3)):

$$\vec{\tau} = \vec{r} \times \vec{F} = \vec{r} \times (-\nabla \hat{H}_{int}) \quad (2.9)$$

Since the interaction potential solely depend on θ , only the $\hat{\theta}$ vector-component from the gradient ($\nabla \hat{H}_{int}$) is nonzero. Furthermore, the cross product with \vec{r} results in a torque directed along the $\hat{\phi}$ vector. When accounting for the minus sign it is seen that

the torque will rotate the molecules towards the polarization axis of the laser pulse. The resulting torque is:

$$\vec{\tau} = -\frac{1}{4} \varepsilon^2(t) (\alpha_{\parallel} - \alpha_{\perp}) \sin 2\theta_0 \hat{\phi} \quad (2.10)$$

where θ_0 is the angle between the laser pulse polarization and the molecular axis at the time of the interaction. The angular velocity can be found through the angular momentum:

$$\vec{\omega} = \frac{1}{I} \vec{L} = \frac{1}{I} \int \vec{\tau} dt = -P \sin 2\theta_0 \hat{\phi} \quad (2.11)$$

where all constants have been collected in the kick strength parameter

$$P = \frac{1}{4} \frac{\int \varepsilon^2(t) dt}{I} (\alpha_{\parallel} - \alpha_{\perp}) \quad (2.12)$$

with I being the inertia of the molecule. From Eq. (2.11) it can be seen that molecules initially located at small angles, where $\sin 2\theta_0 \sim 2\theta_0$, will have angular velocities proportional to their initial angle. They will therefore reach the polarization axis ($\theta = 0$) at the same time and alignment is obtained. Molecules initially located at large polar angles will lag behind and rotate into alignment at a later time.

Three important conclusions can be made from this simple model. First, the speed of the forced rotation, and hence the time delay until the alignment is obtained, depend on the pulse energy and the inertia of the molecules. Second, the alignment will be brief since the molecules will continue to rotate under the field-free conditions. Third, the degree of alignment is limited since no matter how high the kick strength is, molecules initially located at large polar angles will always lag behind.

2.2.2 Quantum mechanical description

As stated above a rotational wave packet is generated through a series of Raman transitions. This wave packet can be computed numerically by solving the time-dependent Schrödinger equation

$$i\hbar \frac{\partial}{\partial t} |\psi(t)\rangle = \hat{H} |\psi(t)\rangle \quad (2.13)$$

where \hat{H} is the total rotational Hamiltonian in Eq. (2.2). The solution is found by expanding the initial wave function in an appropriate orthonormal basis

$$|\psi^i(t)\rangle = \sum_n C_n(t) |n\rangle \quad (2.14)$$

where i denotes the initial state. By inserting this into the time-dependent Schrödinger equation and projecting onto a specific eigenstate $|n'\rangle$ a set of coupled differential

equations for the expansions coefficients is found

$$i\hbar\dot{C}_{n'}(t) = C_{n'}(t)E_{n'} + \sum_n C_n(t)\langle n'|\hat{H}_{int}|n\rangle \quad (2.15)$$

where E_n is the eigenvalue for the n 'th eigenstate of the field-free rotational Hamiltonian. These differential equations are then propagated through the interaction with the pulse [33]. After the interaction the time evolution of the wave packet is trivially found simply by accumulation of phase

$$|\psi^i(t)\rangle = \sum_n C_n(t_0)|n\rangle e^{iE_n(t-t_0)/\hbar} \quad (2.16)$$

where t_0 is the time of the turn-off of the pulse. Since the eigenstates are now time dependent the expectation value for $\cos^2\theta$ is also expected to be time dependent, and in analogy with Eq. (2.8) it can be expressed as:

$$\langle \cos^2\theta \rangle_T(t) = \sum_i w_i(T_{rot}) \langle \psi^i(t) | \cos^2\theta | \psi^i(t) \rangle \quad (2.17)$$

From the classical model we know that alignment occurs right after the laser pulse, however, from the quantum mechanical wave packets, recurrences in alignment is expected as the wave packet components will come back into phase at certain times. These recurrences of alignment are termed alignment revivals. For molecules with regularly spaced energy levels (E_n), such as linear and symmetric top molecules, complete reconstruction occurs, apart from an overall phase, and the alignment is expected to be repeated. For asymmetric tops, where the energy levels are less regularly spaced, only parts of the wave packet will rephase and hence alignment revivals will be weakened. The timing of the revivals depend on the energy level structure and hence on the rotational constants of the molecules. For the simple case of a linear molecule where all eigenenergies are multiples of $2B$, B being the rotational constant perpendicular to the molecular axis, rotational revivals occur at integer multiples of $1/(2B)$ [34, 35].

CHAPTER 3

Experimental setup

A schematic drawing of the experimental setup is shown in Fig. 3.1. The molecules to be investigated are expanded into vacuum using a pulsed valve. After skimming, the molecular pulse is crossed at 90° with two or more pulsed laser beams. First, one or more laser pulses (pump pulses) starts the experiment and then, after a short time delay, one or two laser pulses (probe pulses) ionize the sample. The generated ions are accelerated, in an static electric field, onto a position sensitive detector. The detector lights up at the position of the ion impact and a CCD camera records the light from the detector.

The different components of the experimental setup will be described in detail in the following sections. In Sec. 3.1 a description of the vacuum system, the pulsed valve and the detection system is given. The laser systems and the optical setup is presented in Sec. 3.2. In Sec. 3.3 an overview of the electronic and trigger setup is presented. Finally the newly developed software for ion image analysis is described in Sec. 3.4.

3.1 Vacuum system

Due to our experimental conditions, where very cold, low density molecular gases are studied, low background pressures are required. Therefore all of our experiments are conducted under high or ultra high vacuum conditions. During my time in Femtolab I have worked with two different vacuum systems. My first work was conducted in an inherited vacuum system, however, from the very start of my Ph.d. project I took part

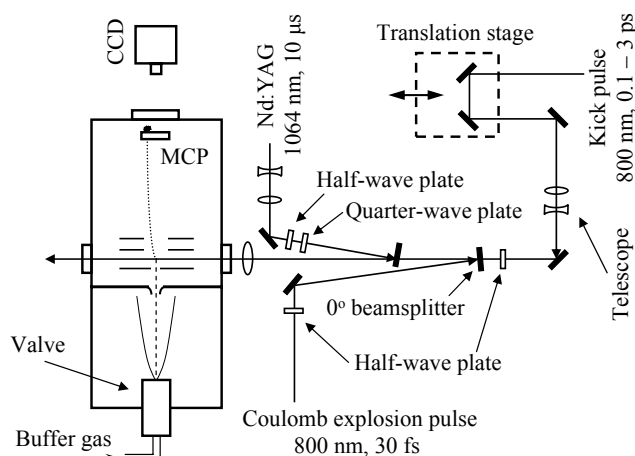


Figure 3.1: Schematic drawing of an experimental setup used for 3D alignment. Here both the Nd:YAG laser and the femtosecond laser is used to align the sample, which is subsequently probed by the Coulomb explosion probe.

in the design and construction of a new vacuum system designed specifically for our purposes. Since 2006 all of my experiments have been conducted in the new vacuum system. Common to both systems is the method of generating a cold molecular sample. We use pulsed valves to expand a mixture of the molecular gas to be investigated, seeded in a helium or argon buffer gas, into vacuum. The gas mixture is supplied to the valve at high pressure and expanded through a small nozzle. During the expansion the molecules are cooled translationally and rotationally through collisions with the buffer gas [36]. In order to avoid relatively high background pressures in the region of the interaction with the laser pulses, the vacuum systems are separated into parts connected only through a small orifice in molecular beam skimmers. These skimmers only let the centermost part of the molecular pulses pass through to the next chamber.

The old vacuum system is composed of three separate chambers, a source chamber housing the valve, a middle chamber and a target chamber where the experiments are conducted. The chambers are separated by beam skimmers (Beam Dynamics Inc.) with orifices of 1 mm in diameter, and the molecular beam travels horizontally through the chambers. The small aperture between the chambers enables us to keep the pressure in the target chamber in the 10^{-8} mbar region while the pressure in the source chamber is 10^{-5} mbar, due to the load of the pulsed valve. The pulsed valve is of the Gentry-Giese type (R. M. Jordan, PSV C-211) and is able to deliver molecular pulses with a duration of around 60 μs at a repetition rate of 20 Hz. The valve nozzle has a diameter of 0.5 mm and is typically operated with a backing pressure of a few bar.

The combination of relatively long pulse duration and large nozzle diameter means that the gas load on the source chamber is very large, for this reason it is pumped by a 2000 l/s diffusion pump. The molecular sample is supplied to the valve by a gas flow system, where the buffer gas is bubbled through a pure liquid sample of the molecule under study and thereafter passes by the back of the valve nozzle. By controlling the temperature of the liquid, the vapor pressure of the sample can be varied. Both argon and helium has been used as buffer gas, cooling is superior with argon however the observed signal decreases significantly as compared to when using helium. Due to the three chamber setup the distance between the valve nozzle and the laser interaction point is 0.7 meter. This rather large distance limits the sample density in the laser interaction region. For molecular samples with low vapour pressure the amount of ions or electrons detected per laser shot will, consequently, be small and long acquisition times are required to ensure sufficient statistics of the detected particles.

During the design phase of the new chamber a number of things were considered in order to improve our experimental capabilities, maximize system stability and reliability and to ease operation. A detailed drawing of the new vacuum system is shown in Fig. 3.2 and a photo of the chamber in operating condition is shown in figure Fig. 3.3. A schematic drawing of the new vacuum system, including a list of all the components, is given in App. A. As can be seen in the figures, this system consists of only two chambers, a decision taken in order to reduce the distance between the valve and the laser interaction region, since the sample density scales as $1/r^2$, at least [36]. The distance in the new chamber is 0.45 m, a reduction of 35% as opposed to the old chamber, increasing the sample density by at least a factor of 2.4. Another important aspect of this system is the ability to send laser beams onto the molecular sample from two orthogonal directions, both orthogonal to the molecular beam. Since the molecular pulse travels vertically both laser beams are sent in horizontally, at a convenient height, (10 cm) above the optical table. This crossed beam setup opens up for, yet unexplored, experiments utilizing two laser beams with orthogonal polarization, both in the plane of the detector. The valve used in the new chamber is a solenoid operated, miniaturized, high-pressure pulsed valve (Even-Lavie). Due to the miniaturization, high stagnation pressures can be used and short opening times are possible. The valve can be operated with up to 100 bar stagnation pressure, resulting in rotational temperatures in the sub 1 K range [37]. Gas pulses as short as 8 μ s can be obtained at 100 bar stagnation pressure and combined with a nozzle diameter of only 0.2 mm this results in very low gas load on the source chamber. The source chamber is pumped by a 400 l/s turbo pump (Leybold, Turbovac 361) and even when running the valve at 40 Hz with 100 bar stagnation pressure the chamber stays in the low 10^{-5} mbar pressure region. The nozzle has a conical shape which helps direct the expansion, thereby increasing the sample density and improving the cooling [38]. The gas supply system is closed and the molecular sample is positioned inside the valve body, very close to the nozzle. Liquid and solid samples are inserted into the valve (liquids soaked on glass filter paper) and will mix with the buffer gas through evaporation or sublimation.



Figure 3.2: Drawing of the new vacuum system. Cut views reveal the valve and the skimmer in the source chamber (bottom) and the circular electrodes in the target chamber (top).

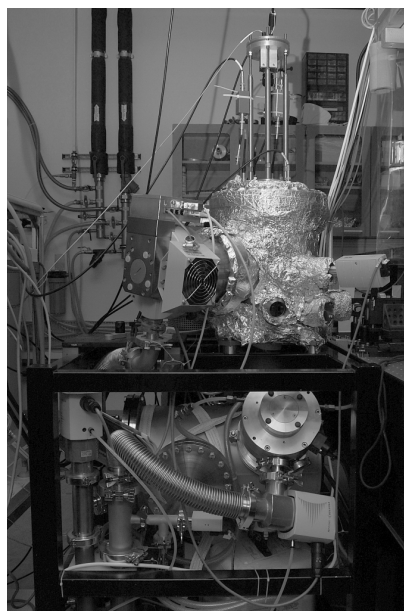


Figure 3.3: Photo of the new vacuum system. Viewed from opposite side as compared to Fig. 3.2

The valve temperature can be controlled from about 40° C to 250° C so molecules that have vapour pressures in the few mbar region somewhere in this temperature interval can be used. Lighter molecules can be mixed with the buffer gas before the gas is supplied to the valve. Since this is a closed system very small amounts of gas is used and consequently very little sample is needed. The second chamber (target chamber) is pumped by a 500 l/s turbo pump (Pfeiffer, TMU 521P). When the pulsed valve is running a small impact is seen on the chamber pressure, rising from the mid 10^{-10} mbar region, to the low 10^{-9} mbar region. The exclusive use of turbo pumps makes the vacuum system much easier to work with and complications with oil contamination are avoided.

In the interaction region the molecular sample is crossed at 90° with one or more pulsed laser beams. The probe pulses break up the molecules into charged fragments which are then projected onto a position sensitive detector using an electrostatic field. The electrostatic field is generated using three open, circular symmetric electrodes set up for velocity map imaging [39]. The first electrode (repeller) has an aperture of

3 mm, the following two (extractor and ground) has apertures of 20 mm. By setting the third electrode to ground and choosing the right voltage ratio between the repeller and extractor, ions generated at different positions in the laser focus, but with same initial velocity vector, will impact on the detector at the same position. This is important since we focus rather weakly resulting in an elongated focus (for $\lambda = 800$ nm and $\omega_0 = 30$ μm the Rayleigh range is about 3 mm) and therefore ions will be generated in a rather large volume. In a grid electrode setup with a homogeneous electric field our non-point ion source would cause blurring of the ion image.

The detector is a chevron stacked microchannel plate (MCP) detector with a phosphor screen attached to its back (EI-Mul Technologies, Ltd.). When adequate voltage is applied over the MCP, a particle impact of sufficient energy will release a guided electron cascade through the MCP. By keeping the phosphor screen at higher voltage than the MCP, the electrons from the cascade will be accelerated onto the screen and it will light up at the position of the impact. Images of the phosphorescence from the screen is then recorded with a CCD camera and transferred to a computer for real-time analysis. Our MCP has an appreciable gain at around 1.5 kV and the phosphor screen is usually set about 2 kV higher than the back of the MCP. Through capacitative read-out of the MCP back, monitored on a fast oscilloscope (see Fig. 3.6), it is possible to see small voltage spikes as ions hit the detector. All ions will arrive within about 10 μs following the probe pulse and will be separated in time according to their mass to charge ratio. A recording of voltage as function of time therefore reveal information about the probe generated ions and will be referred to as a mass/charge spectrum. Using a fast, high-voltage gate it is possible to isolate signals from single ion species by only having appreciable gain in the MCP for short time intervals. In our setup we keep the back of the MCP at 1.2 kV and gate the front down to -0.6 kV with a fast pulser. The pulser is able to generate pulses as short as 60 ns with rise and fall times around 10 ns, which has been sufficiently fast to separate the ion species used for our imaging experiments.

3.2 Optical setup

The most important components in our lab are the nanosecond and femtosecond laser systems. The femtosecond laser system consists of two separate regenerative amplifiers seeded by the same femtosecond oscillator. The oscillator (Spectra Physics, Tsunami) delivers a pulse train of 100 fs pulses near 800 nm at a rate of 82 MHz. The two regenerative amplifiers (Clark MXR, CPA 1000 and Spectra Physics, Spitfire) both run at 1 kHz and outputs pulses with energies of up to 0.9 mJ and 2.3 mJ respectively. The nanosecond laser systems consists of a injections seeded, Q-switched Nd:YAG laser (Spectra Physics, Quanta Ray Pro 270-20) supplying 10 ns pulses at 1064 nm at a rate of 20 Hz with pulse energies of up to 1.5 J. It is electronically synchronized to the femtosecond laser with a jitter on the order of 1 ns. The Nd:YAG

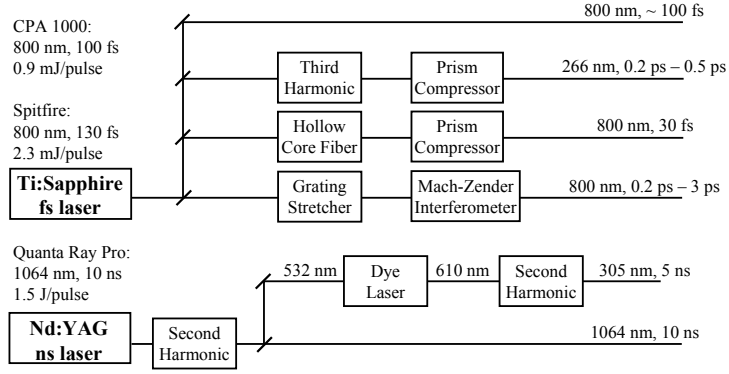


Figure 3.4: Schematic drawing of the optical setup.

laser also supplies a frequency doubled output which is used to pump a dye laser (Lambda Physik, Scanmate 2). Our laser pulses can be divided into two groups, pump pulses that start the experiment and probe pulses that generates ions for ion imaging detection. An overview of the optical setup is given in Fig. 3.4.

3.2.1 Pump pulses

For adiabatic alignment the direct 1064 nm output from the Nd:YAG laser is used. The pulse energy is controlled by rotating the polarization of the pulse using a half-wave plate and subsequently sending it through a polarizer.

For nonadiabatic alignment the output from one of the regenerative femtosecond amplifiers is used. For most experiments the direct output pulses are too short, since the total pulse energy is too low at non-ionizing intensities, and a grating stretcher has therefore been built (see Fig. 3.5 (a)). The stretcher chirps the pulses by taking advantage of the color dependent reflection angle from the grating. The transform limited pulses from the laser are first reflected on the grating, sent through a cylindrical lens and reflected back onto the grating through the lens by a 0° mirror (M2). The mirror is positioned one focal length behind the lens, and the combination of the two works as a telescope. By changing the distance between the grating and telescope the amount of added chirp can be controlled. After the beam has passed once through this setup it will have a spatial chirp. In order to circumvent this the pulse is sent through an additional time by a second 0° mirror (M3). The total group velocity dispersion added to the pulse is [40, 41]:

$$\phi''(\omega) = \frac{d^2\phi_c(\omega)}{d\omega^2} = -\frac{2\lambda^3\varepsilon}{\pi c^2 d^2} \left[1 - \left(\frac{\lambda}{d} - \sin\gamma \right)^2 \right]^{-1} \quad (3.1)$$

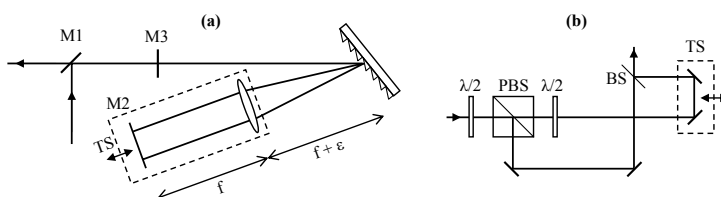


Figure 3.5: Schematic drawing of the grating stretcher (a) and the modified Mach-Zender interferometer (b).

where d is the groove spacing of the grating, γ is the Littrow angle of the grating and ε is the displacement of the grating from the focal point. With our current grating ($d = 1/1200$ mm, $\gamma = 27.7^\circ$) a displacement of $\varepsilon = 1.1$ cm will stretch a 100 fs pulse to 3 ps. Careful alignment of the stretcher is crucial since good spatial and temporal profiles can be hard to archive. In some experiments we enhance the degree of alignment by using two time separated picosecond pulses. The two pulses are generated from the output of the grating stretcher using a modified Mach-Zender interferometer (see Fig. 3.5 (b)), where the first beam splitter is replaced by a half-wave plate ($\lambda/2$) and a polarizing beam splitter (PBS). This gives us full control over the power distribution of the two pulses. An additional half-wave plate is inserted to ensure equal polarization of the two output pulses. Control over the relative timing of the two pulses is obtained by inserting a translation stage (TS).

3.2.2 Probe pulses

Our method of measuring alignment is by extracting information about the spatial orientation of molecules through photo-fragment imaging. Experimentally this is done in two steps. First, ionic fragments from the molecules must be generated. This is done either through dissociation with a UV pulse followed by selective ionization with a second pulse, or by Coulomb explosion due to a single intense pulse. Second, the ionic fragments are projected onto a detector using an electrostatic field. When the electrostatic field is setup for velocity map imaging, the ion impact position on the detector depends only on the initial ion recoil velocity. Therefore, if the fragments recoil along their bond axis^a, the orientation of the molecules can be extracted from recording the ion impact positions on the detector. It should be noted that one could easily imagine situations where the axial recoil approximation is not valid. Charge asymmetric multiple ionization is an example where the ionic fragments may not recoil along their bond axis. Also if dissociation is slow the molecules may have time to rotate during dissociation; A fast dissociation will, however, automatically freeze rotation, due to the increased inertia as the fragments fly apart.

^aknown as the axial recoil approximation.

As mentioned above we have used two different probe schemes to generate ions for velocity map imaging. Usually an intense pulse ($\sim 2 \times 10^{14}$ W/cm²) is used to strip off several electrons from the molecules, which subsequently dissociate due to Coulomb repulsion. Due to the nature of this dissociation we call this probe the Coulomb explosion probe. In the dissociation process it is crucial to minimize influence on the sample by the probe. For Coulomb explosion we keep the pulse duration short (~ 30 fs) in order to minimize the torque exerted by the pulse on the molecules and to obtain a fast ionization. As soon as the molecules are ionized they will quickly fly apart due to the repulsion. The Coulomb explosion pulses are generated from part of the output of the femtosecond laser system by spectral broadening and subsequent compression [42]. They are spectrally broadened by self-phase modulation in an argon atmosphere at a pressure of about 2 bar. The broadened pulses are chirped and are therefore sent through a prism pair for compression.

Some of our experiments have been conducted on small hydrocarbon molecules containing a carbon-iodine (C-I) bond. For these molecules excitation from a non-bonding orbital on the iodine atom to an anti-bonding orbital localized along the C-I bond leads to prompt dissociation, along the bond axis, into neutral fragments [43]. The iodine atoms are left in either the ground state or a spin-orbital excited state. A few nanoseconds after dissociation the iodine atoms are ionized by 2+1 photon resonance enhanced multiphoton ionization (REMPI) using a 304.59 nm or 303.96 nm nanosecond laser pulse, for the ground and excited state respectively [44]. The electronic excitation is resonant with 266 nm photons, which are easily generated through third harmonic generation of the output from the femtosecond laser system. The REMPI pulse is generated by frequency doubling the output from our dye laser (Rhodamine 640 dissolved in methanol) in a 3 cm thick KDP crystal. We call this probe the dissociation-ionization probe.

If the alignment and probe laser pulses are linearly polarized, parallel to the detector, the ion distribution contains cylindrical symmetry. The full three dimensional ion recoil velocity distribution ($f_{ion}(\theta)$) can therefore be obtained from the recorded two dimensional projections through inverse Abel transformation [45]. As it is possible to extract the angular selectivity ($P_{diss}(\theta)$) of the 266 nm dissociation pulse the actual angular distribution of the C-I bond axis ($f(\theta)$) can be found if the dissociation-ionization probe is used:

$$f_{ion}(\theta) = f(\theta) \cdot P_{diss}(\theta) \quad (3.2)$$

From the angular distribution the often used measure of the degree of alignment, $\langle \cos^2 \theta \rangle$, can be calculated:

$$\langle \cos^2 \theta \rangle = \int \cos^2 \theta f(\theta) \sin \theta d\theta \quad (3.3)$$

The dissociation-ionization probe is not an orientationally unbiased probe. The dissociation efficiency is most (least) effective for molecules with the C-I bond parallel

(perpendicular) to the polarization of the probe, therefore, angular localization perpendicular to the probe is difficult to detect [46].

In many experiments the full angular distribution is not needed and a relative measure for the degree of alignment is sufficient. In those cases the two dimensional ion distribution on the detector plane is used to calculate $\langle \cos^2 \theta_{2D} \rangle$, where θ_{2D} is the angle between the polarization vector of the alignment pulse and the ion impact on the detector. In our experience $\langle \cos^2 \theta_{2D} \rangle$ is a good quantitative measure for the degree of alignment, it is however important to note that the value is biased by the probe.

The two probe schemes have different advantages and uses. If the full angular distribution must be found we are limited to the rather cumbersome two-pulse (and two-laser) dissociation-ionization probe and to study molecules containing a C-I bond. In most experiments however, a relative measure for the degree of alignment is sufficient and we use the Coulomb explosion probe. This probe is easier to use and is not limited to 20 Hz by the Nd:YAG laser.

3.2.3 Beam overlap and pulse timing

The laser beams are sent into the vacuum system collinearly along a single axis (see Fig. 3.1). This is done by combining all laser beams using beam splitters and dichroic mirrors and centering them through two irises. The beams are focused onto the molecular pulse using either a custom made $f = 30$ cm achromatic lens when the dissociation-ionization probe is used, or a plano-convex $f = 30$ cm lens, when the Coulomb explosion probe is used. Telescopes in each laser beam are used in order to fix all foci at the same position (correct for chromatic aberration) and, equally important, to control the focal spot size of each beam. Naturally the probe pulse focus must be smaller than the pump, otherwise the effect of the pump pulse will be diminished. The relative size of the foci is, however, also very relevant since molecules within the pump pulse focus will experience different field strengths depending on their precise transverse position. Molecules at the center of the focus will experience higher fields than molecules located away from the center and the alignment will therefore depend on the position inside the focus. The observed alignment will thus be an average over the alignment intensities probed by the probe pulse. For comparison of theoretical calculations with experimental results this intensity averaging over the focal volume has to be accounted for [18]. In order to only do measurements on the best aligned molecules it is usually desired to have the probe focus much more smaller than the pump focus.

Synchronization of the nanosecond pulses to the femtosecond pulses is done electronically using a delay generator for triggering the Q-switch of the Nd:YAG laser. The relative timing is monitored by a fast photodiode. For the femtosecond (and picosecond) pulses, where sub picosecond time resolution is needed, the temporal resolution of the photodiode is not sufficient and nonlinear optical cross-correlations are necessary for determining the precise relative timing. In the dissociation-ionization probe

setup we monitor the output 400 nm light stemming from difference-frequency mixing of the 800 nm alignment pulses and the 266 nm dissociation pulses in a 0.2-mm-thick BBO crystal. For the Coulomb explosion pulse, type-II frequency doubling is used and again the output 400 nm light is monitored. The 400 nm light is filtered out and monitored using a fast diode. A boxcar integrator (Stanford Research Systems, SR250) collects the signal at the full 1 kHz repetition rate and sends it to a computer through an ADC. The relative pulse timing is controlled by a large computer-controlled delay stage (Schneeberger, custom-build electronics) with a travel length of 0.5 meters, giving us more than a 3 ns time interval (double pass) with a 67 fs resolution (minimum step size of 0.01 mm). A LabVIEW program has been written to control the stage and record correlated stage positions and diode signals for the cross-correlation.

When setting up for an experiment the laser foci are overlapped by centering them sequentially on a series of pinholes with reducing size (500 μm , 100 μm and 20 μm). This is done outside the vacuum chamber by inserting a 45° metallic mirror right after the focusing lens. When all foci are well centered in the pinholes fine-tuning is done directly on the molecular beam by monitoring ion signals on the MCP.

3.3 Electronics

This section is included to give an overview of how our experiments are timed and what type of electronic equipment is used. A number of very different timescales are in play and everything has to be synchronized appropriately. On one extreme end is our laser pulses which have durations down to just a few tens of femtoseconds, however, our experiments usually run as slow as 20 per second. A schematic drawing showing all the electronic components is shown in Fig. 3.6.

The master clock (trigger) in our experiments stem from the most important lab workhorse, the femtosecond laser system. A trigger is supplied for every laser pulse at a rate of 1 kHz, however, the molecular valve and the Nd:YAG laser have maximum repetition rates of 40 Hz and 20 Hz respectively, significantly reducing the rate of our experiments. The pulse to pulse jitter on the 1 kHz laser system is on the order of 10 ns, determined by the pulse train of the 82 MHz oscillator, and the jitter between each laser pulse and its corresponding trigger is specified to be below 250 ps. A schematic drawing of the trigger timing is shown in Fig. 3.7. The outputs marked with a '*' trigger components for the following laser pulse, since they must be triggered a few hundred microseconds prior to the experiment. For the nonadiabatic alignment experiments, requiring sub picosecond time resolution, the pulse delays are controlled optically by delay stages and all time relevant pulses are generated from the same initial laser pulse. In this way there will be no jitter between these pulses. The output from the Nd:YAG laser has a jitter of about 0.5 ns, however, due to a pulse duration of 10 ns for the adiabatic alignment pulses and since precise timing of the REMPI pulse is inessential, this relatively large jitter does not give rise to any problems. The 10 ns

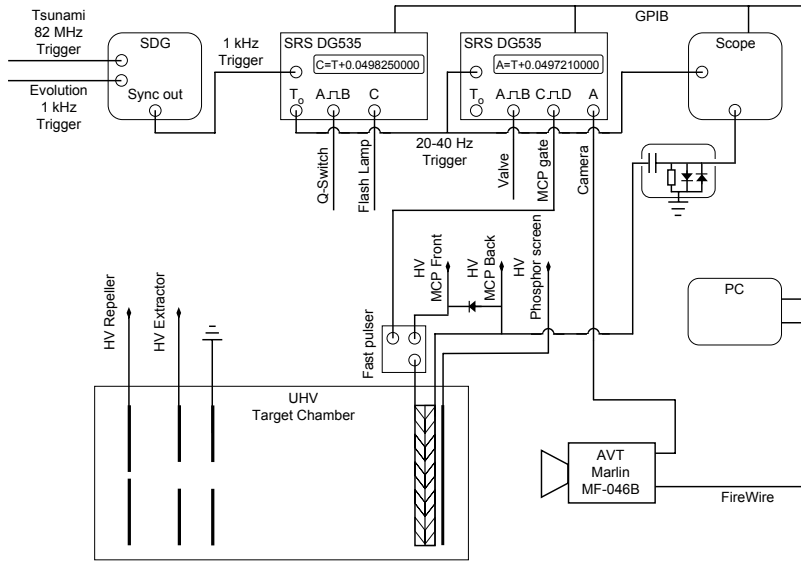


Figure 3.6: Schematic drawing of the electronic setup.

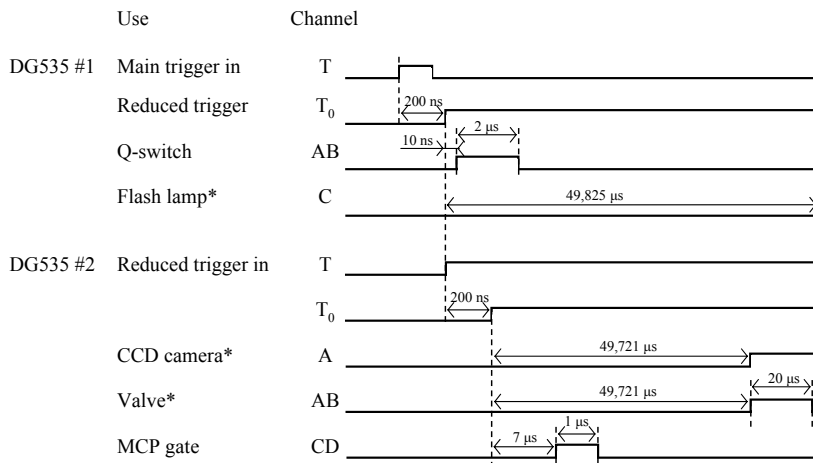


Figure 3.7: Schematic drawing of the trigger timings. The depicted timings are used when the Nd:YAG laser is required. The MCP gate delay (channel C) and width (channel D) is individually set to isolate a single ion species.

Use	Model	Output voltage	Ripple (full load)
Repeller & Extractor (ions)	MP15P	0 to 15 kV	150 mV p-p
Repeller & Extractor (electrons)	MP5N	0 to -5 kV	20 mV p-p
Phosphor screen & MCP back	MP5P	0 to 5 kV	20 mV p-p
MCP front	MP1N	0 to -1 kV	10 mV p-p

Table 3.1: High voltage module specifications. The stability and temperature coefficient is specified as $<0.007\%/hr$ and $<25\text{ ppm}/^\circ\text{C}$ respectively.

pulse to pulse jitter (1 kHz trigger) is insignificant since the components triggered by the previous pulse (the pulsed valve, the CCD camera and the flash lamps) operate on a microsecond timescale. The delay generators (Stanford Research Systems, DG535) can be used to reduce the repetition rate since they will not accept new triggers until all channel delays have passed. The 1 kHz trigger rate can for example be reduced to 20 Hz, by setting a delay between 49 ms and 50 ms. The first delay generator is used in this way when the Nd:YAG laser is not needed. The CCD camera is triggered by channel A due to a limited number of available channels. To synchronize it correctly to the phosphorescence of the MCP an additional delay, calculated from the MCP gate and valve delay (channel A and C), is added internally in the camera through the data analysis software.

The high voltages are supplied by a custom build unit, based on modular supplies (Spellman, MP). There is a total of seven supplies, three for the detector, two positive supplies for ion imaging and two negative supplies for electron imaging. A list of the supplies is given in Table 3.1. Each supply is controlled by a 0 V to +10 V input, supplied by a 16 bit DAC, giving a high voltage output of 0 V to the maximum output of the supply. The ripple ($<0.001\%$), stability ($<0.007\%/hr$) and temperature coefficient ($<25\text{ ppm}/^\circ\text{C}$) are well within our experimental requirements. As shown in Fig. 3.6 a diode has been placed between the supplies for the MCP in order to protect the MCP against too high voltages that could potentially destroy it.

3.4 Data acquisition and analysis

In combination with the upgrade of the vacuum system we decided to also upgrade the data analysis software. The main reason for this was that the old software was cumbersome to work with and hard to modify. As the new valve was able to run at 40 Hz, a faster camera had to be implemented anyway. We decided to purchase a CCD camera with an IEEE 1394 (FireWire) interface (Allied Vision Technologies, Marlin MF-046B) since no additional hardware (such as a frame grabber card) would be needed and, more importantly, the camera easily could be replaced due to the industry standard data communications protocol (IEEE 1394 IIDC v. 1.3). The camera

has a resolution of 780×582 pixels and a gray scale color depth of 8 bit. The full frame is transferred to the computer, however only the center 575×575 pixels are saved in memory. At a repetition rate of 40 Hz this would add up to 13 MB/s or 48 GB of data per hour. Clearly it is impractical to store this much data and real-time image analysis is therefore needed. As we are only interested in the position of each ion hit, just two coordinates are needed for each ion hit; With 100 ion hits per image and storing in single-precision floating point numbers that would result in 115 MB of data per hour, a reduction of 99.7%. The data analysis program is written in LabVIEW (version 8.0) since well developed software kits are available. Our program is based on the NI Vision module (IMAQ Vision and IMAQ for IEEE 1394 cameras) and solely uses functions from these kits. Two different analysis routines have been developed, a simple analysis (Centroid9.vi) that is able to run very fast, up to 200 Hz on the current computer, and a more sophisticated analysis capable of running up to 30 Hz (Centroid14.vi). The LabVIEW code for the data acquisition program and for Centroid14 is presented in App. B.

The image analysis in Centroid14 is based on a series of image manipulations that isolates particles and enhances the contrast between noise and actual ion hits. First, the image is convoluted with a 3 by 3 gaussian kernel for smoothing. Then, it is convoluted with a 7 by 7 laplacian kernel to enhance edges and increases the contrast between the actual ion hits and noise. Noise is then removed, first by setting a threshold and then by removing small particles. The particle removal is done by an erosion, where all pixels connected to a pixel with zero intensity are set to zero intensity. Particles that are completely removed by the erosion will be removed from the image, whereas particles surviving the erosion are restored to their original shape and size. Particles surviving the noise removal are considered as ion hits, their centers are found and the pixel coordinates are stored (with subpixel resolution). Finally, each particle is checked for its size and shape. If it is large and elongated it is most likely two or more connected ion hits and as a means of compensation the center coordinate is counted twice. An image series demonstrating the steps in the image analysis process is shown in Fig. 3.8, the dark blue color represents low pixel intensity and the dark red color represents high pixel intensity (see colorbar). Image (a) is a 59×59 pixel chop of an image containing iodine ion hits. Fig. 3.9 shows the pixel intensity along a straight line connecting the three major ion hits in the image. The strength of the edge detection is clearly seen in the step between graph (b) and (c), the lower intensity parts connecting the particles are efficiently removed and isolated particles are obtained. The following noise removal steps cut away the weak areas and the smallest particles that are caused by noise, either in the camera or in the detector. In the simple analysis only a threshold and an erosion is applied and the remaining particles are considered as ion hits and treated the same way as the ion hits in the advanced analysis. Naturally the computation time for this analysis is much lower since the cumbersome convolutions are avoided, however, the methods also has severe drawbacks. The threshold has to be set relatively high in order to remove noise and separate close lying particles, with

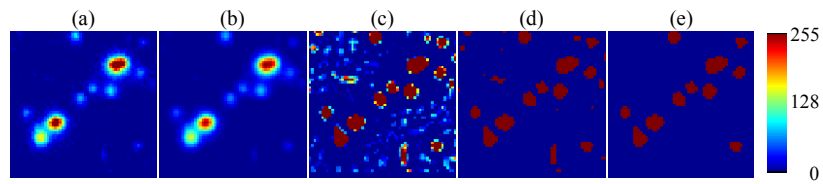


Figure 3.8: Data analysis on part of a sample image, showing each step in the data processing. (a) Original; (b) Gauss smoothing; (c) Edge detection; (d) Threshold; (e) Particle removal.

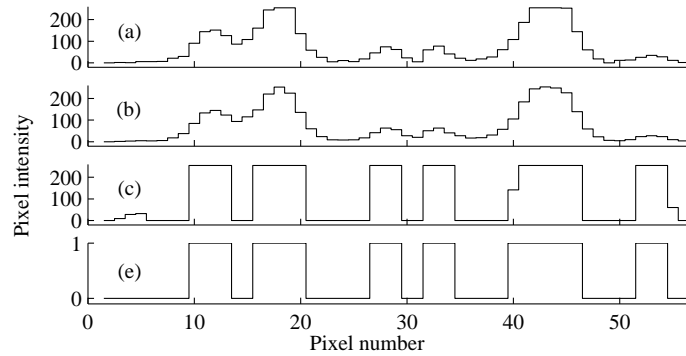


Figure 3.9: Pixel intensity along a straight line connecting the three major ion hits in Fig. 3.8, starting bottom left. (a) Original; (b) After gauss smoothing; (c) After edge detection; (d) After threshold and particle removal.

the result of wiping out many weak particles. This can prove to be a serious limitation when working with a nonuniform detector, where particles in the less sensitive areas will be removed by the threshold, resulting in false reading of the velocity distribution. The major advantages of the advanced analysis is its effectiveness in detecting even weak particles and in separating connected ones. This means that we can turn down the gain of the detector to make each ion hit smaller (down from about 30 pixels to about 16 pixels) and run with a higher amount of signal without too much loss in reliability, caused by connected particles. Since we experimentally are limited to 40 Hz by the pulsed valve, we always use the advanced image analysis. The reduction from 40 Hz to 30 Hz is easily compensated by a higher amount of detected particles per shot and on top of that we are more confident in avoiding connecting particles. A detailed description of the image analysis program, CCD camera settings and a custom data analysis program can be found in [47].

CHAPTER 4

Experimental Results I: Nonadiabatic alignment

In this chapter I will present experimental results on nonadiabatic alignment of both symmetric and asymmetric top molecules. For these experiments a short linearly polarized nonresonant laser pulse, generated from part of the output from our femto-second laser system, was used to induce alignment. In the first section the alignment obtained immediately after the laser pulse will be presented. The second section will address the the long time evolution of the rotational wave packet and focus on the alignment revivals observed.

4.1 Early time alignment dynamics

The alignment dynamics of the most polarizable molecular axis, following the interaction with a short linearly polarized laser pulse, will be presented in this section. Through our experiments we have learned, that when only the alignment of the most polarizable molecular axis is considered, the initial alignment dynamics is quite similar for symmetric and asymmetric top molecules. Therefore, I will focus on results from the asymmetric top molecule iodobenzene [$\text{C}_6\text{H}_5\text{I}$]. For iodobenzene the most polarizable molecular axis is coinciding with the C-I axis. The degree of alignment is measured by the dissociation-ionization probe and quantified by $\langle \cos^2 \theta \rangle$, where θ is the angle between the C-I axis and the alignment pulse polarization. The experiments were conducted in the old vacuum system, with an alignment pulse duration of 1.4 ps (FWHM, gaussian shape) and an intensity of $4.1 \times 10^{12} \text{ W/cm}^2$. In order to enable inverse Abel transformation of the ion images all laser pulses were linearly polarized,

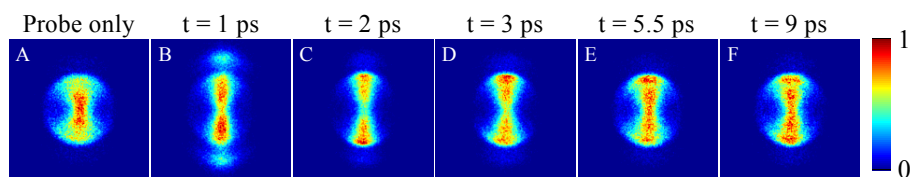


Figure 4.1: Images of I^+ ions generated with the dissociation-ionization probe. The first image (A) is recorded with the probe only. The observed changes in the following images are induced by a 1.4 ps long 800 nm pulse with a peak intensity of 4.1×10^{12} W/cm². The images are recorded at a variable delay, t , of the probe with respect to the peak of the alignment pulse.

parallel to the plane of the detector. An image series showing the recorded I^+ ion distributions is shown in Fig. 4.1. The images are false color, with the color representing the relative intensity of the I^+ ion signal (see the colorbar). The laser pulses are polarized along the vertical axis in the images. From the first image (Fig. 4.1 A, Probe only) where no alignment is present, we see that the random orientation of the sample is not reflected, instead the ion hits are mostly observed along the polarization direction of the probe pulses (the 266 nm and 305 nm pulse). As mentioned in Sec. 3.2.2 the dissociation-ionization probe is not orientationally unbiased, however, its angular selectivity can be extracted from this image, since the angular distribution of the molecules is known to be isotropic. On the following images the distribution of the I^+ ions on the detector is changed as the alignment pulse is added. Initially, at a delay of 1 ps between the center of the alignment pulse and the dissociation pulse ($t = 1$ ps) a confinement along the vertical axis is apparent (Fig. 4.1 B). This is attributed to alignment of the molecular C-I axis along the polarization axis of the alignment laser pulse. The intensity of the alignment laser pulse is still relatively high at $t = 1$ ps, reduced by a factor of about four from the peak value. Due to the presence of the alignment laser field this image is not directly comparable to the other images in Fig. 4.1. A significant part of the ions are produced in an ionization process involving photons from both the alignment pulse and the dissociation pulse and hence the ion angular distribution is different. A further narrowing of the ion signal along the vertical axis is observed in the third image (Fig. 4.1 C), recorded at $t = 2$ ps, indicating increased alignment. At this time the field from the alignment laser is almost completely gone (reduced by more than a factor of 100) and alignment is therefore observed at almost field-free conditions. From the following images (Fig. 4.1 D-F) the nature of the rotational wave packet is revealed, since the degree of alignment rapidly drops as the wave packet dephases. The alignment seen at $t = 2$ ps clearly deteriorates and the images return to a less confined shape.

As described in Sec. 3.2.2 the full three dimensional angular distribution, $f(\theta)$,

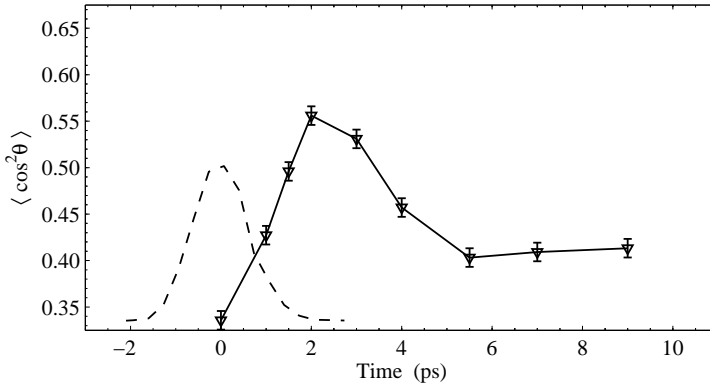


Figure 4.2: Degree of alignment expressed as the average value of $\cos^2 \theta$, following the interaction with a 1.4 ps long 800 nm pulse with an intensity of 4.1×10^{12} W/cm². The dashed line represents the cross-correlation of the alignment pulse (arb. units).

of the C-I axis, and hence the most polarizable molecular axis, can be extracted from these two dimensional images. In order to do this the angular distribution of the ions, $f_{ion}(\theta)$, for each image and the angular selectivity of the dissociation pulse, $P_{diss}(\theta)$, must be found (see Eq. (3.2)). The angular distribution of the ions can be found from each image by inverse Abel transformation, however, a background I⁺ signal, originating from multiphoton dissociative ionization by the dissociation pulse, must first be removed, since the angular selectivity of this contribution can not be found. This is done by recording an additional image under the same conditions, but omitting the ionization pulse and subsequently subtracting it from the original image. The angular selectivity of the dissociation pulse is found directly from image A in Fig. 4.1 by inverse Abel transformation, since the angular distribution of the C-I axis, $f(\theta)$, is uniform in this image. Naturally, the background contribution must also be subtracted from this image. With both the angular selectivity of the dissociation pulse and the angular distribution of the ions at hand, the full three dimensional angular distribution of the C-I axes, $f(\theta)$, can be readily computed through Eq. (3.2). Finally, $\langle \cos^2 \theta \rangle$ can be calculated for each image via Eq. (3.3). For a uniform and a perfectly aligned distribution $\langle \cos^2 \theta \rangle$ is 1/3 and 1, respectively. If the angular localization is perpendicular to the alignment axis, i.e. in the equatorial plane ($\theta = \pi/2$), $\langle \cos^2 \theta \rangle$ drops below 1/3. Since this alignment is the opposite of conventional alignment, it is termed anti-alignment. The $\langle \cos^2 \theta \rangle$ values extracted from the images in Fig. 4.1 along with additional recordings (not shown here) are presented in Fig. 4.2 together with a cross-correlation of the alignment pulse (dashed line, arb. units). We see that the alignment peaks immediately after the interaction with the alignment pulse at about $t = 2$ ps with

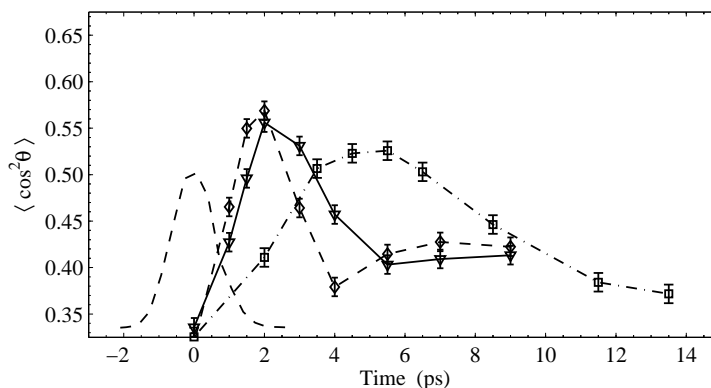


Figure 4.3: Degree of alignment at three different alignment pulse intensities. Squares: 1.4×10^{12} W/cm², triangles: 4.1×10^{12} W/cm² and diamonds: 5.5×10^{12} W/cm². The duration of the alignment pulse is fixed at 1.4 ps. The dashed line represents the cross-correlation of the alignment pulse (arb. units).

$\langle \cos^2 \theta \rangle \sim 0.56$. The alignment is, however, brief and is observed to fall off already at $t = 3$ ps. From this we conclude that alignment under field-free conditions can indeed be obtained for iodobenzene by inducing a rotational kick with a short pulse.

Having established field-free alignment we would like to see how the obtained alignment depend on the laser pulse intensity. Therefore we repeated the experiment with both a lower (1.4×10^{12} W/cm²) and higher (5.5×10^{12} W/cm²) intensity in the alignment pulse and kept the duration of the pulse fixed at 1.4 ps. The measured alignment from these experiments including the curve from Fig. 4.2 is presented in Fig. 4.3. Three things are apparent from this figure. First, as the intensity is increased the dynamics in the alignment becomes faster. At the low intensity the alignment peaks around $t = 5$ ps, three picoseconds after the peak observed at the high intensity. Second, the minute increase in the degree of alignment when increasing the intensity from 4.1×10^{12} W/cm² to 5.5×10^{12} W/cm² suggest a saturation of the alignment in this intensity range. We were, however, unable to further investigate this saturation since multiphoton ionization sets in at higher intensities. Third, the alignment improves as the intensity is increased, reaching maximum values of $\langle \cos^2 \theta \rangle \sim 0.52$, ~ 0.56 and ~ 0.57 at intensities of 1.4×10^{12} W/cm², 4.1×10^{12} W/cm² and 5.5×10^{12} W/cm² respectively.

When evaluating our experimental observations of the alignment immediately after the interaction with the short pulse, we see that they correspond well with the δ -kick model presented in Sec. 2.2.1. The angular velocity of the molecules is expected to be proportional to the total pulse energy and hence the dynamics will be faster at higher

intensity. The degree of alignment is limited by the *sine* term in the angular velocity and hence a saturation in the degree of alignment is expected. Finally, the increased alignment obtained at higher intensity can be attributed to the fact that the molecules are not rotationally frozen prior to the interaction with the pulse; As the intensity and hence the forced angular velocity is increased, the initial rotational motion of the molecules will be less important and the alignment will be improved.

One would expect that a higher degree of alignment could be obtained at higher total pulse energy. The only way to do this without ionizing the molecules is to increase the pulse duration and keep the intensity as high as possible without ionizing. However, the peak in alignment would then be obtained earlier, during the presence of the alignment pulse and not under field-free conditions [28].

4.2 Long time alignment dynamics: Rotational revivals

After the initial alignment peak we observed a rapid decrease in the alignment. Due to the quantum nature of the rotational wave packet, rephasing of the wave packet components is expected and alignment recurrences (revivals) should be observed. The timing of the revivals is defined by the rotational energy levels since they determine the phase of the rotational wave packet components (see Eq. (2.16)). Different types of revivals are therefore expected for molecules of different symmetry.

In the following sections I will present results from experiments on the symmetric top molecule methyl iodide [CH_3I] and the asymmetric top molecule iodobenzene.

4.2.1 Symmetric top molecule

In this section I will present experimental results on the symmetric top molecule methyl iodide. The field-matter interaction for a symmetric top molecule is independent of χ (see Eq. (2.3)) and consequently K is conserved in the interaction. Hence the energy difference of the components of the wave packet will be integer multiples of B , the rotational constant perpendicular to the C-I axis, and the K dependent term in the energy will only contribute to an irrelevant overall phase shift in the wave packet^a. Due to this simple energy-level structure, complete rephasing of the rotational wave packet is expected at the rotational revivals and the alignment should therefore be fully restored. With a rotational constant of $B = 7.5013$ GHz [48] revivals are expected for every $1/(2B) = 66.655$ ps.

In order to investigate the alignment dynamics of this molecule we recorded ion images in the range from 1-75 ps following a 0.75 ps long alignment pulse with an intensity of 1.3×10^{13} W/cm². Due to the large amount of data points needed and the fact that we were only interested in the relative timing and strength of the revivals, we did not determine the full three dimensional angular distribution, $f(\theta)$. As

^aRotational energy for a prolate symmetric top molecule is: $E(J,K) = BJ(J+1) + (A-B)K^2$.

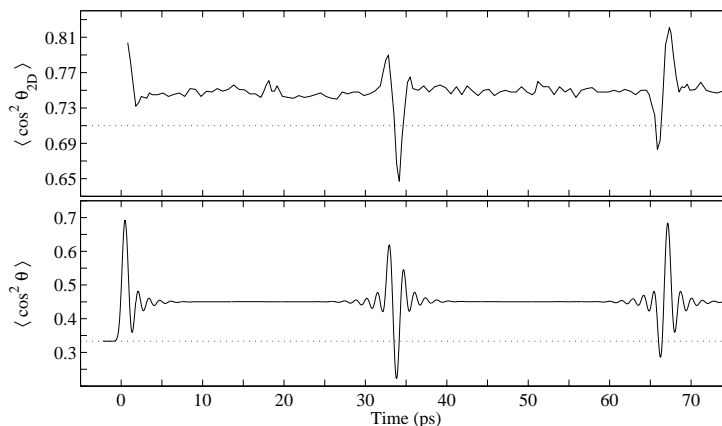


Figure 4.4: Alignment dynamics of methyl iodide as a function of time after the peak of the alignment pulse. Top: Experimentally determined values of $\langle \cos^2 \theta_{2D} \rangle$ using a 0.75 ps alignment pulse with a peak intensity of 1.3×10^{13} W/cm². The dotted line represents the value obtained from a sample with random angular distribution. Bottom: Numerically calculated values of $\langle \cos^2 \theta \rangle$ with a similar alignment pulse and a rotational temperature of 10 K.

described in the previous section this requires recording of a background image for each delay in addition to much higher ion counts to obtain enough statistics for inverse Abel transformation. From each image we determined $\cos^2 \theta_{2D}$, where θ_{2D} is the angle between the alignment pulse polarization and the ion velocity projection in the plane of the detector. In this scheme a perfectly aligned, a randomly oriented and a perfectly anti-aligned distribution corresponds to a $\langle \cos^2 \theta_{2D} \rangle$ value of 1, 0.5 and 0 respectively. The results are displayed in the top of Fig. 4.4. The horizontal dotted line at $\langle \cos^2 \theta_{2D} \rangle = 0.71$ represents the value obtained from an experiment without the alignment pulse, i.e. with random angular distribution of the sample. The displaced value, compared to 0.5 for an isotropic distribution on the detector, reflect the angular selectivity of the dissociation-ionization probe used for this experiment. In Fig. 4.4 we observe significantly faster alignment dynamics than what we observed for iodobenzene in the previous section. After the first data point at $t = 0.8$ ps the alignment quickly dephases within just 1 ps. The fast evolution is a result of the considerable lower inertia of methyl iodide compared to iodobenzene.

After the initial alignment peak we see that the value of $\langle \cos^2 \theta_{2D} \rangle$ does not drop to the same level as that of a randomly distributed sample (0.71), but rather stays at a higher value. This increase in the degree of alignment is referred to as permanent alignment and is a result of the way the wave packet is induced [49]. In the interaction with a linearly polarized laser pulse very high J states are excited, however, M remains

conserved. Classically this ($J \gg M$) corresponds to the molecules rotating with their C-I axis in a plane containing the polarization axis. The depletion of molecules rotating with their C-I axis in a plane perpendicular to the polarization axis ($J \sim M$) is the reason for the increased $\langle \cos^2 \theta_{2D} \rangle$ value. The two transients located around $t = 34$ ps and $t = 67$ ps are identified as the first half and the first full rotational revival. At the full revival the alignment is observed to be at least as strong as the initial alignment, indicating complete rephasing of the wave packet. At the half revival located near $t = 34$ ps, the value of $\langle \cos^2 \theta_{2D} \rangle$ drops below the value for a random distribution, and the sample must therefore be anti-aligned.

To confirm our experimental findings a numerical calculation was conducted by Tamar Seideman and Edward Hamilton [18]. The calculation was conducted at a rotational temperature of 10 K for a 0.75 ps pulse with an intensity of 1.0×10^{13} W/cm² and included averaging over the intensity profile of the focal volume. The calculated alignment dynamics is presented in the bottom graph of Fig. 4.4. Only a qualitative comparison can be made between the two curves for a number reasons. Most importantly, experimentally we had insufficient statistical data to extract $\langle \cos^2 \theta \rangle$ and the two measures for alignment are therefore not the same [50]. Also, the experimental rotational temperature is not known and the 10 K used in the calculation is only an estimate (although probably a quite realistic estimate). In spite of these differences we do observe very similar structure in the two graphs. The calculation reproduces both the permanent alignment, the timing and the detailed shape of the half and full revival very well. The many oscillations observed in the numerical calculation near the revivals is a result of the quantum nature of the wave packet. Experimentally these oscillations are washed out due to spatial averaging over the intensity distribution in the focal volume of the alignment pulse and averaging over a thermally populated rotational ensemble. In Sec. 4.2.2 we show that such a detailed structure can be measured by carefully choosing and controlling essential experimental parameters.

In the interaction with an intense nonadiabatic alignment pulse very high rotational states are excited and centrifugal distortion of the molecules is expected [18]. Such distortion destroys the periodicity in the energy levels and therefore render perfect reconstruction of the rotational wave packet impossible. Experimentally this would be observed as distorted alignment transients and reduced alignment at the revivals. A recording of $\langle \cos^2 \theta_{2D} \rangle$ in the time intervals corresponding to the 1st, 2nd, 16th and 42nd revival is shown in Fig. 4.5. The dotted vertical lines indicate the predicted revival times $T_{rev} = n/(2B) + 0.4$ ps, n being the order of the revival. The addition of 0.4 ps is to account for the initial alignment maximum 0.4 ps after the peak in the alignment pulse. From Fig. 4.5 we see that alignment revivals persist for a very long time. The 42nd revival near 2.8 ns after the alignment pulse is clearly visible and marks the limit of our time delay, defined by the 0.5 m translation stage. The revival time fits remarkably well with what is expected from the rotational constant for all the revivals. The first two revivals are observed to be very similar both in amplitude, shape

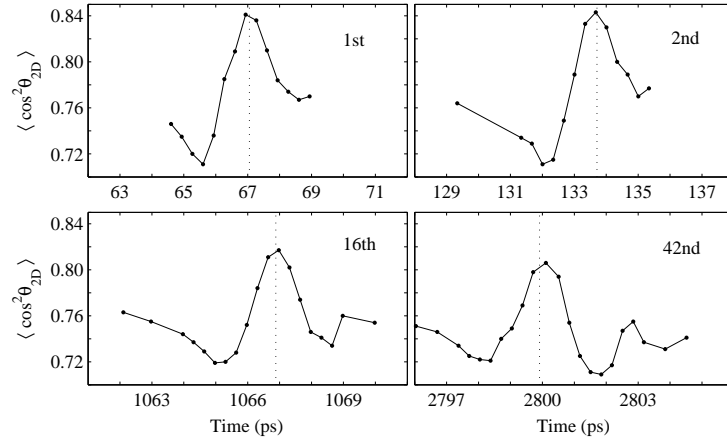


Figure 4.5: Alignment dynamics of methyl iodide, represented by $\langle \cos^2 \theta_{2D} \rangle$ near selected full revival times. The panels show the first, second, 16th and 42nd full revival. The dotted vertical lines indicate the predicted revival times $T_{rev} = n/(2B) + 0.4$ ps, n being the order of the revival.

and timing with respect to T_{rev} . When moving on to the 16th the revival the alignment maximum is reduced and the temporal evolution of the transient has become slower. These effects are more pronounced at the 42nd revival, where further reduction in the alignment is observed. Numerical calculations, including centrifugal distortion in the energy expression, confirm that the experimentally observed changes can be attributed to centrifugal distortion [18]. Here the effects of the centrifugal distortion become noticeable at the fourth revival and become much more apparent on a nanosecond time scale. A similar effect has been observed in experiments on N_2 by Dooley *et al.* [51]. We are confident that any effects from collisions can be neglected since our sample is very cold and has a low density. This is confirmed by the fact that Sussman *et al.* [52] were able to see revivals in CO_2 for hundreds of picoseconds in a gas cell at 300 K and 300 Torr.

4.2.2 Asymmetric top molecule

In the previous section symmetric top molecules, with their regular energy level structure, are shown to exhibit periodically spaced revivals. As will be presented in this section, asymmetric top molecules show much more interesting rotational dynamics, since the rotational energy levels are not regularly spaced and both J and K levels are excited in the wave packet when interacting with a nonresonant linearly polarized laser pulse. The irregular energy level structure does, however, result in reduced alignment

at the revivals compared to the prompt alignment, since only partial rephasing of the wave packet will occur. The observed revivals depend on the specific coherences in the wave packet and hence the type of revivals and their strength will depend on the molecular inertia and polarizability tensor as well as on the alignment laser pulse.

In this section results from experiments on iodobenzene are presented. These experiments were conducted in the new vacuum chamber and the sample was supplied by the Even-Lavie valve, enabling preparation of samples at very low temperature (see Sec. 3.1). The Coulomb explosion probe (25 fs, 2.5×10^{14} W/cm²) was used, since a large number of data points was needed and knowledge of the exact angular distribution was less important. In this way the experiment was not limited to a repetition rate of 20 Hz by the Nd:YAG laser. Also, as seen for the methyl iodide data in Fig. 4.4, the relative alignment measure $\langle \cos^2 \theta_{2D} \rangle$ gives a good estimate of the alignment and can easily be compared qualitatively to $\langle \cos^2 \theta \rangle$. The focal spot size of the probe pulse was adjusted to be significantly smaller than that of the alignment beam ($\omega_0^{probe} = 25$ μ m, $\omega_0^{align} = 45$ μ m). The low rotational temperature, combined with the spatially confined probe, allowed us to observe quantum-mechanical structure that was predicted numerically in the past [17] but was never observed in the laboratory.

Figure 4.6 shows three I⁺ ion images. The first image is recorded without an alignment pulse. By polarizing the Coulomb explosion probe perpendicular to the detector, ion images of an isotropically distributed sample should be circularly symmetric, which is indeed what we observe in Fig. 4.6 A. Alignment of the C-I axis along the alignment laser polarization should show up as localization along the vertical axis in the ion images. Image B (Fig. 4.6), recorded 351 ps after the peak of the alignment pulse (0.2 ps, 1.6×10^{13} W/cm²), shows localization along this direction. In Fig. 4.6 C, recorded at $t = 702$ ps, the ion signal is predominately observed along a horizontal line. This reflects anti-alignment, where the C-I axis of the molecules is aligned perpendicular to the alignment laser polarization axis. In these three ion images two distinct radial rings are observed. The inner (outer) ring result from I⁺ ions Coulomb fragmenting with a C₆H₅⁺ (C₆H₅²⁺) counter ion [53]. The outer ring is barely visible in the images and the inner ring correspond to the radial range of the intense red ring in Fig. 4.6 A. The reduced signal intensity just "North East" of the center of each image is due to reduced gain in that area of the MCP detector. These images were the first to be recorded with the new imaging system described in Sec. 3.4 and since the image analysis programs were not fully developed at that time, the particle detection was conducted with Centroid9. When comparing with images recoded subsequently using Centroid14 (see Fig. 6.6 in Sec. 6.2), the advantage of the more sophisticated analysis is apparent. Here the low sensitivity area of the MCP detector is not seen, since Centroid14 is very insensitive to particle size and intensity.

For a full investigation of the revival structure a series of ion images was recorded in three selected time windows representing the intervals where the important alignment transients occur. From each image $\langle \cos^2 \theta_{2D} \rangle$ was determined using only the

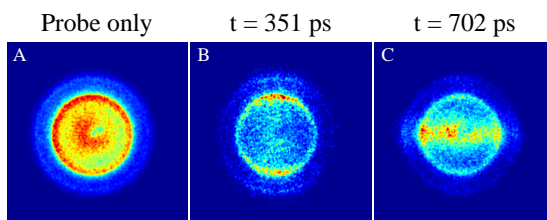


Figure 4.6: I^+ ion images obtained (A) without the alignment pulse and (B), (C) including a 0.2 ps alignment pulse with an intensity of $1.6 \times 10^{13} \text{ W/cm}^2$.

ions from the outer ring. In this way we restrict the probed alignment intensities to a narrow range close to the maximum value, because the high nonlinearity of the Coulomb explosion process leading to $[I^+, C_6H_5^{2+}]$ formation only occurs efficiently in the spatial regions near the center of the alignment laser focus. The observed alignment dynamics obtained with the alignment pulse used for the images in Fig. 4.6 is shown in Fig. 4.7 (a). At very short pulse durations the alignment dynamics is insensitive to the pulse duration [54]. Therefore, if the pulse duration is kept short the relevant alignment parameter determining the induced wave packet, is the fluence (pulse intensity times duration) of the alignment laser pulse. For this relatively weak fluence ($F = 3.3 \text{ J/cm}^2$) the initial alignment peak is reached at $t = 4.5 \text{ ps}$. The following alignment dynamics is very similar to that observed for methyl iodide in Fig. 4.4, with two transients clearly visible around $t = 351 \text{ ps}$ and $t = 702 \text{ ps}$. Here the alignment is, however, observed on the first transient and anti-alignment on the second. Image B in Fig. 4.6 corresponds to the alignment peak in the first transient of Fig. 4.7 (a) and image C to the minimum $\langle \cos^2 \theta_{2D} \rangle$ value in the second transient.

We choose to conduct a series of experiments where the fluence was varied. Since the intensity in Fig. 4.7 (a) was already at the multiphoton ionization limit we had to increase the pulse duration in order to increase the fluence. As stated above changing the pulse duration has a very minimal effect on the observed alignment dynamics as long as it remains short. We repeated the experiment with pulse durations of 0.5, 1.0 and 2.0 ps and, with the exception of the 2.0 ps case, adjusted the intensity to the largest value the molecules could withstand without ionizing. At 2.0 ps the available laser power was insufficient to reach this limit. Figure 4.7 (b), (c) and (d) show the alignment dynamics measured for fluences of 5.8, 9.0 and 12.5 J/cm^2 , respectively. As the fluence is increased we observe that the alignment immediately after the pulse improves and shifts to earlier times, just as seen in Sec. 4.1. In addition the observed revivals undergo a qualitative change. At $F = 5.8 \text{ J/cm}^2$ new transients start to form around $t = 378 \text{ ps}$ and $t = 757 \text{ ps}$ whereas the ones observed at the lowest fluence are weakened in strength. When the fluence is further increased, as shown in Fig. 4.7 (c) and (d), the revival structure seen at the lowest fluence is further reduced and is only

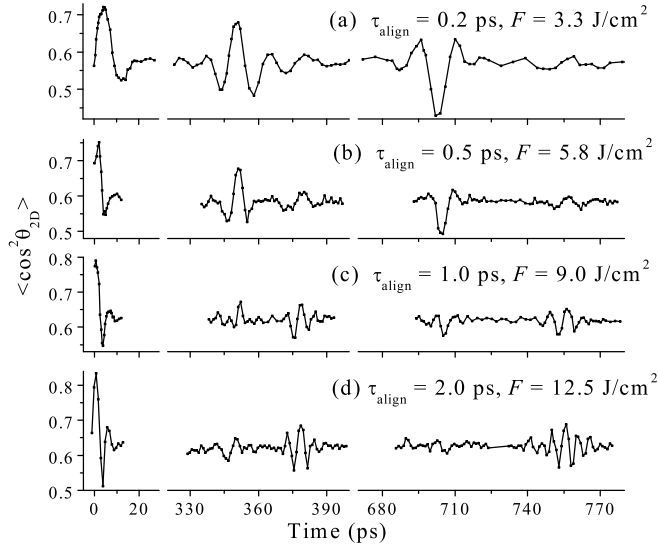


Figure 4.7: $\langle \cos^2 \theta_{2D} \rangle$ recorded in three time intervals representing the rotational dynamics shortly after the alignment pulse and in the two first regions with *J*-type and *C*-type revivals. The measurements are carried out at four different fluences and pulse durations, indicated on each panel. The peak intensities are (a) 1.6×10^{13} , (b) 1.1×10^{13} , (c) 8.5×10^{12} and (d) 5.9×10^{12} W/cm². Each data point is obtained from an I⁺ ion image accumulated over 1500 laser shots and containing about 40,000 ion hits (as the images in Fig. 4.6).

just barely visible at the highest fluence. The new type of revival on the other hand increases in strength. When the lowest and highest fluence cases are compared [Fig. 4.7 (a) and (d)], we see that the induced wave packets show completely different revivals, and hence completely different coherences determine the alignment dynamics. The numerous oscillations near the revivals, especially pronounced at the highest fluence, has been observed in numerical calculations of asymmetric tops and is well understood theoretically [6]. It is a result of beats between the highest rotational energy levels excited [20]. Experimentally, this has not been observed earlier, due to the combination of averaging over the intensity profile of the alignment laser focus and numerous initially populated rotational energy states. Numerically it was shown that this averaging washes out the detailed substructure of the revivals.

To classify the revivals we use the nomenclature of rotational coherence spec-

troscopy (RCS) introduced by Felker *et al.* [34]. Although the wave packets excited in our experiments are different from those of RCS the appearance and timing of the alignment transients are very similar. The spacing between the revivals observed at the lowest fluence in Fig. 4.7 is 352.5 ps, very close to $1/[2(B + C)]^b$. Except for the polarity (alignment on the half revival and anti-alignment on the full revival) this type of transient is very similar to the one observed for the symmetric top molecule in Sec. 4.2.1. In RCS this type of transient arise from coherences between wave packet components that differ in J by one or two and are therefore termed J -type revivals. For an asymmetric top molecule the J -type transients are expected to have a periodicity of up to $1/[2(B + C) + (C - B)^2/(2A - B - C)]$ [35], which for iodobenzene is 353.85 ps. From the experimental results in Fig. 4.7 the time separation of the half and the full J -type revival can be determined, however, due to the low amplitude at the highest fluence [Fig. 4.7 (d)] the separation was not found for this case. In Fig. 4.8 the alignment dynamics in the region around the half and the full J -type revival is compared. Since the polarity of the J -type revival reverses between the half and full revival, the $\langle \cos^2 \theta_{2D} \rangle$ values from the half J revival have been mirrored in the axis of the permanent alignment level ($\langle \cos^2 \theta_{2D} \rangle = 0.56, 0.58$ and 0.62 for Fig. 4.8 (a), (b) and (c) respectively) and time shifted in order to overlap with the full revival. The blue curve in Fig. 4.8 represents the mirrored, time shifted half J revival while the red curve show the recorded full J revival. The best fit for the delay between the revivals is: (a) 352.5 ps, (b) 353.4 ps and (c) 353.6 ps. We see that these values agree very well with the expected separation of 353.85 ps and that as the fluence is increased the agreement improves. The second type of revival, observed at the higher fluences [Fig. 4.7 (b), (c) and (d)], is unique to asymmetric tops and is termed C -type revival, since the periodicity corresponds to rotations about the molecular c -axis. From [35] we expect a periodicity of $1/(4C) = 377.29$ ps for iodobenzene. In Fig. 4.9 the alignment dynamics around the second C revival is shown as the red curves. The blue curves represent the alignment dynamics around the first C revival, which has been shifted in time. The best fit for the delay between the revivals is (b) 377.0 ps, (c) 377.5 ps and (d) 377.0 ps, in very good agreement with the expected value of 377.29 ps. The excellent correspondence between the periodicity according to the RCS theory and our experiments suggest that this method can be used as a spectroscopic tool. With the J and C -type revival periodicity at hand a good estimate for the B and C rotational constants can be found. To find all three rotational constants the molecule must be planer since the rotational constants then are related through the inertia ($I_c = I_a + I_b$). The A constant can thus be found from B and C by: $A = C \cdot B / (B - C)$.

To confirm and generalize our experimental findings numerical calculations were conducted by Tamar Seideman and Edward Hamilton. The calculations were conducted at a rotational temperature of 1.0 K and did not include any averaging over

^bRotational constants for iodobenzene: $A = 5671.89$ MHz, $B = 750.416$ MHz and $C = 662.627$ MHz [55]

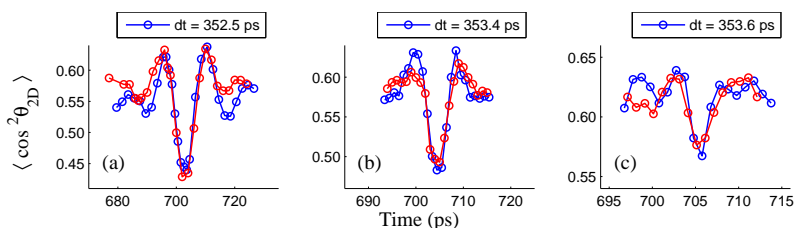


Figure 4.8: Red curve: $\langle \cos^2 \theta_{2D} \rangle$ values near the full J revival. Blue curve: $\langle \cos^2 \theta_{2D} \rangle$ values mirrored in the axis of the permanent alignment level ($\langle \cos^2 \theta_{2D} \rangle = 0.56, 0.58$ and 0.62 for (a), (b) and (c) respectively) and shifted in time according to the label above each graph. The fluences are: $3.3, 5.8$ and 9.0 J/cm^2 for (a), (b) and (c).

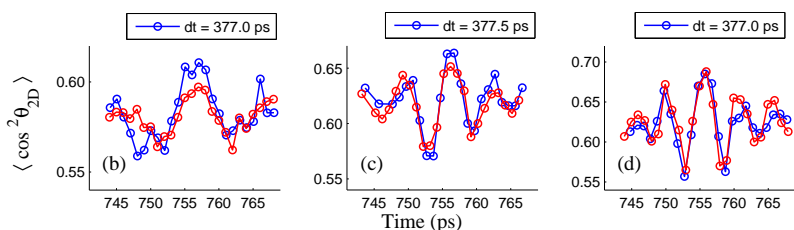


Figure 4.9: Red curve: $\langle \cos^2 \theta_{2D} \rangle$ values near the second C revival. Blue curve: $\langle \cos^2 \theta_{2D} \rangle$ values from the first C revival shifted in time according to the label above each graph. The fluences are: $5.8, 9.0$ and 12.5 J/cm^2 for (b), (c) and (d).

the focal volume since our experimental probe was very confined. The results are presented in Fig. 4.10. Although $\langle \cos^2 \theta \rangle$ was used as the measure of alignment and pulse durations and fluences are lower than in the experiment, the resulting alignment transients are qualitatively very similar to our experimental findings. The transition from the symmetric top like J -type revival at low fluence to the C -type revival at higher fluences is clearly confirmed. The calculation also reproduce the rich revival structure near the C -type revival.

Our results on iodobenzene show that the nonadiabatic alignment dynamics of asymmetric top molecules can be controlled by the fluence of the alignment pulse. At low fluence the quasiperiodic symmetric top like J -type revivals dominate. With increasing fluence the molecules preferentially rotate in the molecular plane about the c -axis and C -type revivals are therefore primarily observed. Rouzée *et al.* [56] observed a similar effect in the alignment dynamics of the asymmetric top molecule ethylene [C_2H_4]. By measuring transient birefringence, following a 100 fs alignment pulse in a gas cell at room temperature, they observed both J and C -type revivals. As their experiment was conducted at very low fluences the transition from the J to C -

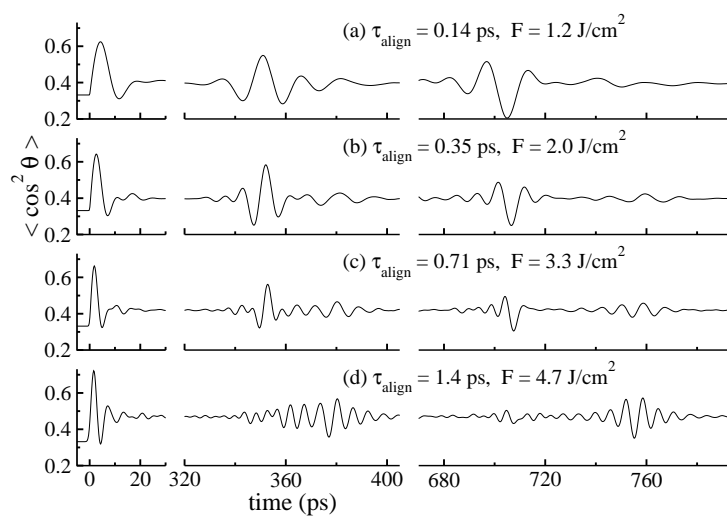


Figure 4.10: Computed alignment dynamics of iodobenzene at four different fluences and pulse durations in the same time intervals as presented in Fig. 4.7. The rotational temperature is 1.0 K and the peak intensities are (a) 8.0×10^{12} , (b) 5.5×10^{12} , (c) 4.4×10^{12} and (d) $3.1 \times 10^{12} \text{ W/cm}^2$.

type revival was not complete but the trend was clearly seen and also discussed in the paper.

For a more complete orientational control all three molecular axes must be confined to space-axes. This can not be obtained by a single linearly polarized pulse and thus more elaborate techniques must be utilized. In Chapter 6 and 7 a number of different approaches to control of all three molecular axes are given.

CHAPTER 5

Experimental Results II: Two-pulse nonadiabatic alignment

In this chapter I will show that the strongest degree of field-free alignment obtainable with a single nonadiabatic alignment pulse can be enhanced by using a two-pulse sequence. A systematic investigation of the optimal pulse duration, intensity and relative timing will be presented.

For many applications it is desired that the degree of alignment under field-free conditions is as high as possible. Using nonadiabatic alignment techniques this can be accomplished by minimizing the rotational temperature of the sample and selecting the most favorable pulse duration and intensity of the alignment pulse. In Sec. 4.1 we found that the degree of alignment improved as the intensity of the alignment pulse was increased. The degree of alignment was, however, limited by the intensity the molecules could withstand without ionizing and a saturation in the degree of alignment at high intensities was also observed. To overcome these limitations Averbukh and Arvieu [31] and Leibscher *et al.* [19, 32] suggested the use of a train of short laser pulses. Their idea is based on the classical δ -kick model (see Sec. 2.2.1) that predicts a limited degree of alignment, due to the *sine* term in the angular velocity, following the interaction with a single short laser pulse (kick pulse). Molecules initially located at large polar angles with respect to the laser pulse polarization axis will not receive a proportional impulsive kick and consequently they will not reach the axis at the same time as molecules initially located near it. This difference in the time at which alignment is reached for different initial angles (θ_0) is the cause of saturation in

the alignment process. By applying multiple pulses the molecules can be prepared in a state where most of them are located at small polar angles to the laser polarization axis. The final laser pulse should be much stronger than the first pulses so that the angular velocity of the molecules, gained from the first pulses, is negligible compared to the angular velocity from the final pulse. In this way it is ensured that the final angular velocities of the molecules, now positioned at small polar angles, are proportional to their polar angle. Numerically the authors found optimal two- and three-pulse alignment schemes, defining the best intensity ratios and relative timings. They found a strong improvement in the obtained degree of alignment as the pulse energy from a single pulse was split into two optimally timed pulses and a slight further improvement by dividing the energy into three pulses [19].

5.1 Initial experiments on iodobenzene

We decided to test experimentally if splitting the laser power into two pulses would improve the obtained degree of alignment. Even though the δ -kick model was based on a linear molecule iodobenzene was chosen as a test molecule, since we have had good experimental experiences with it. As presented below our findings are in very good qualitative agreement with the theoretical predictions.

The two-pulse experiments on iodobenzene were done in combination with the results presented in Sec. 4.1. The alignment pulses were 1.4 ps long and the total available intensity was 5.5×10^{12} W/cm². The experimental $\langle \cos^2 \theta \rangle$ values are shown in Fig. 5.1 along with cross-correlations of the alignment pulses (dashed line, arb. units). The depicted relative alignment pulse timing and intensity was found to be optimum under these experimental conditions. When only the first pulse is used, centered at $t = 0$ ps, with a peak intensity of 1.4×10^{12} W/cm², the degree of alignment peaks at $\langle \cos^2 \theta \rangle = 0.52$. By increasing the intensity a factor of three ($I = 4.1 \times 10^{12}$ W/cm²), second pulse only, the obtained alignment improves to 0.56. A further marginal improvement in the degree of alignment is observed when combining the total energy of these two pulse into a single pulse ($I = 5.5 \times 10^{12}$ W/cm²), with a peak of $\langle \cos^2 \theta \rangle = 0.57$ (see Fig. 4.3, diamonds). From the small improvements in the observed alignment it is clear that saturation has been reached. On top of this, a further increase in the intensity is not possible, since multiphoton ionization is already starting to appear at these high intensities. By instead using both alignment pulses with the relative timing depicted in Fig. 5.1 we observed a greatly improved alignment (Fig. 5.1, circles). The alignment peaked under essentially field-free conditions (intensity reduced by more than a factor of 100) about 2 ps after the peak of the second pulse, with a $\langle \cos^2 \theta \rangle$ value of 0.66. Clearly, these results demonstrate that it is possible to overcome the limitations imposed by saturation and ionization by distributing the total pulse energy into two properly timed pulses.

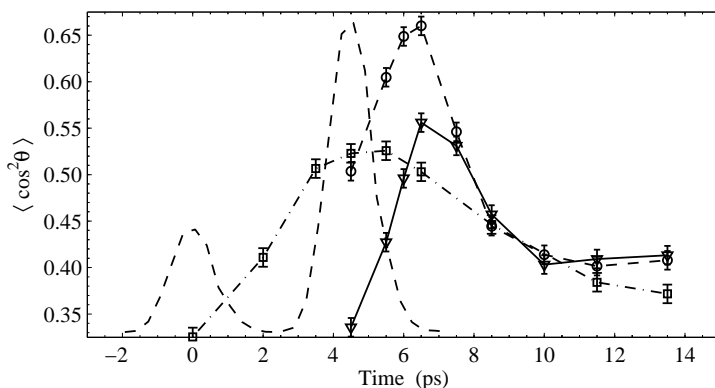


Figure 5.1: The degree of alignment vs time obtained for the first pulse only (squares), the second pulse only (triangles), and both pulses (circles). The dashed line represent the cross-correlations of the alignment pulses (arb. units). For a sample of randomly oriented molecules $\langle \cos^2 \theta \rangle = 1/3$.

5.2 Detailed experiments on *tert*-butyliodide

Having established great improvements in the obtained alignment by utilizing two alignment pulses a detailed study is undertaken. The goal is to identify the conditions under which the degree of alignment is optimal, in particular we investigate the two-pulse alignment dependence on the relative intensity (I_1/I_2), time separation and the duration of the two laser pulses.

A critical condition for achieving enhanced two-pulse alignment is that the second pulse is sent around the time when the degree of alignment from the first pulse peaks. For a symmetric top or linear molecule this can be achieved by synchronizing the second pulse to either the initial alignment maximum following the first pulse or to an alignment revival. Contrary, for an asymmetric top molecule like iodobenzene, the degree of alignment at the revival is weakened compared to that immediately after the pulse and in order to obtain optimum alignment we are therefore constrained to send the second pulse immediately after the first. For this reasons we decided that the detailed experiments should be carried out on a symmetric top molecule. In this way we were relatively unconstrained in our choice of pulse durations, since we did not need to worry about optical interference effects, due to temporal overlap of the two alignment pulses. For the experiments *tert*-butyliodide [$\text{IC}(\text{CH}_3)_3$] was selected, since it contains a C-I bond axis along the most polarizable molecular axis and due to its relatively high moment of inertia^a perpendicular to the C-I axis. If the inertia

^aRotational constants for *tert*-butyliodide: A = 150.262 GHz and B = 7.50130 GHz [48]

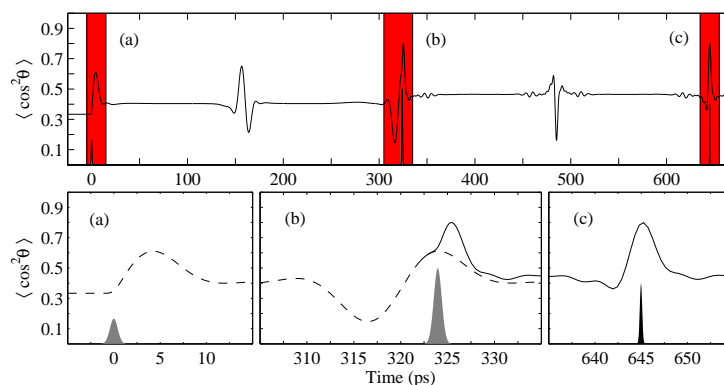


Figure 5.2: Calculated timing sequence of the two alignment pulses and the probe pulse. The time regions in red are expanded in the lower three subfigures. The grey areas in (a) and (b) represents the alignment pulses whereas the black area in (c) show the probe pulse. The dashed curve depicts the degree of alignment from the first pulse ($I_1 = 2 \text{ TW/cm}^2$) only, the solid shows the alignment when the second pulse ($I_1 = 6 \text{ TW/cm}^2$) is included. The temperature was set at 1 K, pulse duration at 1 ps and focal volume averaging was included.

is too low, molecular rotations will be fast and very short alignment pulses would be required.

Figure 5.2 illustrate the timing of the two alignment pulses and the dissociation pulse used to measure the time dependent degree of alignment. It also shows the calculated alignment dynamics due to the two alignment pulses. The lower panels (a), (b) and (c) are expansions of the red regions in the upper graph. The dashed curve in Fig. 5.2 (a) and (b) represents the obtained degree of alignment due to the first alignment pulse. At the first full revival, near the peak in the alignment, the second pulse is applied [Fig. 5.2 (b)] and the following dynamics is represented by the full curve. On the subsequent full revival the degree of alignment is probed by resonant dissociation and delayed ionization of the iodine fragment (the dissociation-ionization probe). The detailed study requires analysis of the alignment as a function of several laser parameters, which necessitates recording a large number of ion images under different conditions. For time reasons this is impractical to perform with high ion statistics in each image and we therefore choose to characterize the degree of alignment by $\langle \cos^2 \theta_{2D} \rangle$. As shown in Chapter 4 this measure agrees qualitatively well with $\langle \cos^2 \theta \rangle$. The experiment was conducted in the old vacuum system using the Jordan valve and we expect a rotational temperature on the order of 10 K. The focal spot size of the alignment laser pulses was $\omega_0 = 25 \text{ }\mu\text{m}$, only slightly larger than the dissociation pulse at $\omega_0 = 20 \text{ }\mu\text{m}$.

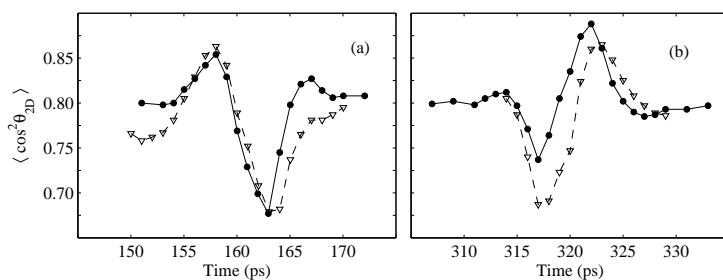


Figure 5.3: The degree of alignment measured at (a) the first half and (b) the first full revival following one or two alignment pulses. The pulse duration is 0.5 ps and the intensity of the second pulse, I_2 , is fixed at 9.4×10^{12} W/cm². Triangles (dashed curve): Second pulse only. Circles (solid curve): $I_1 = 4.5 \times 10^{12}$ W/cm².

Figure 5.3 shows experimentally recorded alignment dynamics around (a) the first half and (b) the first full revival following the second alignment pulse. The triangles (dashed line) mark the measured alignment when only the second pulse is used and the circles (solid line) when a weak prepulse is added. The pulse duration is 0.5 ps and the intensity of the second pulse, I_2 , is 9.4×10^{12} W/cm². For the two-pulse data the intensity of the first pulse, I_1 , is 4.5×10^{12} W/cm². The relative timing of the two alignment pulses is chosen such that the second pulse is sent at the time where the degree of alignment due to the first pulse peaks. The very high apparent permanent alignment level of $\langle \cos^2 \theta_{2D} \rangle \sim 0.80$ is due to the selectivity of the dissociation-ionization probe, just as observed for methyl iodide in Sec. 4.2.1. The one pulse alignment revivals (triangles, dashed line) are very similar to what has been observed previously for linear and symmetric top molecules. At the half revival the molecules first become aligned, then antialigned and finally return to the permanent alignment level. The full revivals almost look like a mirror image of the half revival with opposite evolution in the alignment. For this particular pulse duration we observe a nearly identical degree of alignment on the half and full revival ($\langle \cos^2 \theta_{2D} \rangle \sim 0.86$). As the prepulse is included the revivals change towards a more symmetrical shape. The alignment on the full revival improves to $\langle \cos^2 \theta_{2D} \rangle \sim 0.88$, however, the antialignment observed at the half revival does not decrease compared to the single pulse case. This could potentially be ascribed to the low sensitivity of the dissociation-ionization probe for perpendicularly aligned molecules (see Sec. 3.2.2).

Having established improved alignment by utilizing two alignment pulses we seek to find the laser parameters leading to the best degree of two-pulse alignment. From the results presented in Fig. 5.3 we see that the best alignment is obtained on the first full revival following the second pulse and therefore, we restrict our measurements to this time interval. We begin by investigating the dependence on the relative delay

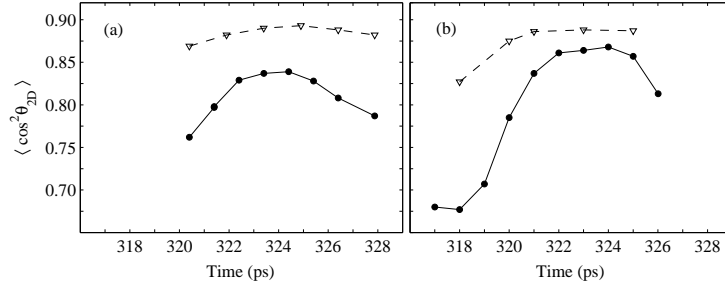


Figure 5.4: Two-pulse alignment dependence on the relative pulse separation. In (a) the pulse duration is 1 ps with $I_1 = 3.7 \times 10^{12} \text{ W/cm}^2$ and $I_2 = 14 \times 10^{12} \text{ W/cm}^2$. In (b) the pulse duration is 0.5 ps with $I_1 = 8.8 \times 10^{12} \text{ W/cm}^2$ and $I_2 = 9.2 \times 10^{12} \text{ W/cm}^2$. The circles show the degree of alignment obtained due to the first pulse only. The triangles show the highest degree of two-pulse alignment obtained when the second pulse is sent at the time depicted on the x-axis.

between the two alignment laser pulses. Experimentally we first recorded the degree of alignment around the first full revival following the first pulse [corresponding to the dashed curve in Fig. 5.2 (b)]. Next, we included the second alignment pulse and measured the degree of alignment on the first full revival following the second pulse [corresponding to Fig. 5.2 (c)] for different delays between the two alignment pulses. The experimental results are depicted in Fig. 5.4, where the circles show the degree of alignment from the first pulse only. The triangles show the highest degree of alignment obtained, on the full revival following the second pulse, when the second pulse is sent at the time given on the x-axis. Referring to Fig. 5.2 this corresponds to plotting the maximum in (c) as a function of the delay between the two alignment pulses. The left graph [Fig. 5.4 (a)] is obtained with at pulse duration of 1 ps and alignment intensities of $I_1 = 3.7 \times 10^{12} \text{ W/cm}^2$ and $I_2 = 14 \times 10^{12} \text{ W/cm}^2$ ($I_1/I_2 \sim 1/4$). There is nearly a one to one correspondence between these two curves. The best degree of two-pulse alignment is, however, obtained when the second pulse is sent slightly after the time where the alignment due to the first pulse peaks. The right graph [Fig. 5.4 (b)] is obtained with pulse durations of 0.5 ps and nearly equal intensity in the two pulses ($I_1 = 8.8 \times 10^{12} \text{ W/cm}^2$, $I_2 = 9.2 \times 10^{12} \text{ W/cm}^2$). The curve for the best two-pulse alignment again follows the degree of alignment due to the first pulse, and the optimum two-pulse alignment is obtained when the second pulse is sent near the time of the best alignment due to the first pulse.

With the optimum delay between the alignment pulses found we investigate the dependency on the intensity of the first pulse, I_1 . The intensity of the second pulse, I_2 , is fixed at $11 \times 10^{12} \text{ W/cm}^2$, just below the value where ionization and fragmentation of the sample start to occur. Again we started by measuring the alignment on the first

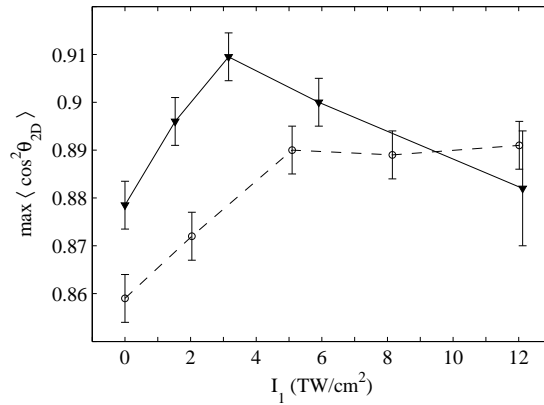


Figure 5.5: Optimum degree of two-pulse alignment as function of the intensity in the first pulse. The pulse duration was 1 ps (triangles, solid line) and 0.5 ps (circles, dashed line). I_2 is kept fixed at 11×10^{12} W/cm² and the second pulse is sent when the degree of alignment due to the first pulse peaks.

full revival following the first pulse for each value of I_1 . The second pulse was then sent at the time of the best alignment due to the first pulse and the degree of alignment on the full revival following the second pulse was finally measured. Results from experiments with pulse durations of 0.5 ps and 1 ps, showing the maximum degree of two-pulse alignment as function of I_1 , are displayed in Fig. 5.5. For the 1 ps pulses a clear maximum is observed with an intensity ratio of $I_1/I_2 \sim 1/3$. As the intensity of the first pulse is further increased the obtained two-pulse alignment reduces. No clear maximum is observed at the lower pulse duration of 0.5 ps. In general, the results show that almost any intensity ratio ($I_1 \leq I_2$) of two optimally timed pulses leads to a significantly higher degree of alignment than that obtained with just one pulse.

The results from the 1 ps pulses agree with the expectation from the δ -kick model, which predicts that the kick from the first pulse should be weak compared to that from the second pulse. For the 0.5 ps pulses this is not observed and the two-pulse alignment is high even though both alignment pulses are equally strong. The reason for this may lie in the rotational temperature of our sample. Calculations by Leibscher *et al.* [19] suggest that as the temperature of the sample increases a stronger prepulse is needed to obtain optimum two-pulse alignment. This makes sense since the degree of alignment from a single pulse is a decreasing function of temperature and an increasing function of pulse energy.

With the optimum pulse separation and relative intensity found we recorded a series of images with high statistics to determine the absolute degree of alignment, $\langle \cos^2 \theta \rangle$, for three different pulse durations (0.5 ps, 1 ps and 2 ps). The intensity

Pulse duration	0.5 ps	1 ps	2 ps
Two pulses	0.57(1)	0.60(2)	0.57(1)
One pulses	0.51(1)	0.53(1)	0.53(1)

Table 5.1: Values of $\langle \cos^2 \theta \rangle$ for different pulse durations with either one or two pulses. For the 0.5 ps and 1 ps results: $I_1 = 3.9 \times 10^{12}$ W/cm², $I_2 = 12 \times 10^{12}$ W/cm². For the 2 ps results: $I_1 = 2.7 \times 10^{12}$ W/cm², $I_2 = 8.4 \times 10^{12}$ W/cm². For the one pulse cases the intensity was I_2 . The uncertainties of the last digit are shown in the table.

of the second pulse was set just below the onset of multiphoton ionization and an intensity ratio of $I_1/I_2 \sim 1/3$ was chosen. The second pulse was sent at the peak in the alignment due to the first pulse on the first full revival following the pulse. The found results are summarized in Table 5.1 both for the second pulse alone and for the two-pulse combination. For all pulse durations we see a significant improvement in the degree of alignment as the prepulse is added. The optimum pulse duration for two-pulse alignment of *tert*-butyliodide was found to be 1 ps. The best degree of alignment obtainable with a single pulse was found to be $\langle \cos^2 \theta \rangle = 0.53$. By adding a properly timed weak prepulse the alignment was improved considerably to $\langle \cos^2 \theta \rangle = 0.60$.

Numerical calculations were conducted to confirm our experimental findings, however, due to limited computational capacity the peak intensities and the rotational temperature are kept lower than those employed in the experiment. We can therefore not expect quantitative agreement with the experimental findings but aim for qualitative similarities.

First the alignment dependence on the time separation between the two alignment pulses was investigated. The calculations were carried out at four intensities of the first pulse, $I_1 = 0.5, 2, 4$ and 6×10^{12} W/cm² while all other parameters were fixed ($\tau = 1$ ps, $T_{rot} = 1$ K and $I_2 = 6 \times 10^{12}$ W/cm²). The results are presented in Fig. 5.6. The same notation as in Fig. 5.4 has been used and thus the full curves show the degree of alignment due to the first pulse around the time where the second pulse is sent. The dashed curve in the left (right) column show the best degree of two-pulse alignment obtained at the first half (full) revival following the second pulse when the second pulse is sent at the given delay. The right column should be compared to our experimental findings in Fig. 5.4. Just as in the experiment the best two-pulse alignment at the full revival is observed when the second pulse is sent near the peak in the alignment due to the first pulse. In fact, as the intensity in the first pulse is increased [Fig. 5.4 (e) to (h)], the optimal timing moves from slightly after to approximately at the alignment peak due to the first pulse. The strongest two-pulse alignment, $\langle \cos^2 \theta \rangle = 0.81$, is observed to be at the full revival and is obtained for $I_1 = 2 \times 10^{12}$ W/cm² [Fig. 5.4 (f)].

Finally a calculation was conducted in order to find the optimal intensity of the first pulse while keeping the intensity of the second pulse fixed. The results for the highest obtained alignment, at the full revival following the second pulse, are depicted

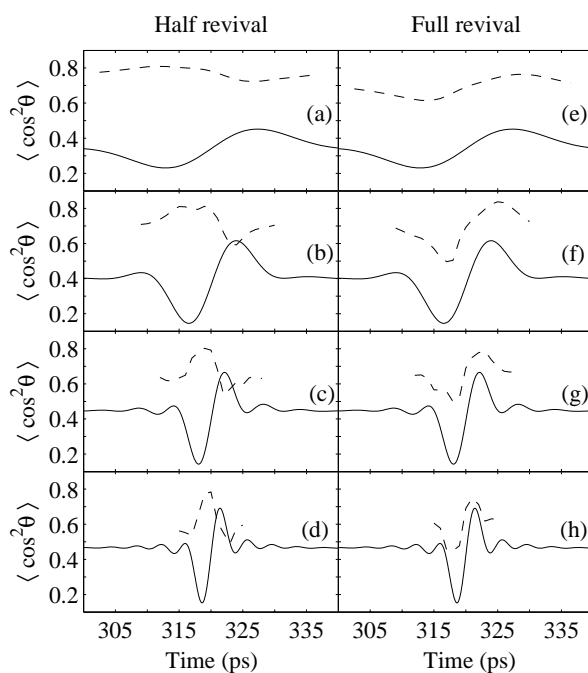


Figure 5.6: Numerical calculation of the degree of alignment as function of the pulse separation. The full curves show the degree of alignment due to the first pulse. In the left (right) column the dashed curve show the best degree of alignment obtained on the half (full) revival following the second pulse when the second pulse is sent at the given delay. The intensity of the first pulse was: (a)(e) $I_1 = 0.5$, (b)(f) $I_1 = 2$, (c)(g) $I_1 = 4$ and (d)(h) $I_1 = 6 \times 10^{12} \text{ W/cm}^2$. The remaining parameters were fixed with a pulse duration of 1 ps, $I_2 = 6 \times 10^{12} \text{ W/cm}^2$ and the rotational temperature 1 K.

in Fig. 5.7. The pulse duration is varied from 0.5 ps (red line) over 1 ps (black solid line) to 2 ps (blue line), the rotational temperature is 1 K and the intensity of the second pulse, I_2 , is $6 \times 10^{12} \text{ W/cm}^2$. The dashed black line represents the results from a 1 ps calculation where focal volume averaging was omitted, i.e. a calculation at the peak intensity only. For all pulse durations the degree of alignment is significantly improved as a weak prepulse is added. As the intensity of the prepulse approaches that of the second pulse the degree of two-pulse alignment drops and for the 2 ps case, it even drops below the level of the single pulse alignment. Under these conditions an optimal prepulse intensity is found for all pulse durations. The optimal prepulse intensity is found to be a decreasing function of the pulse duration. For the 1 ps case the best intensity ratio was numerically found to be $\sim 1/3$ just as for the experimental

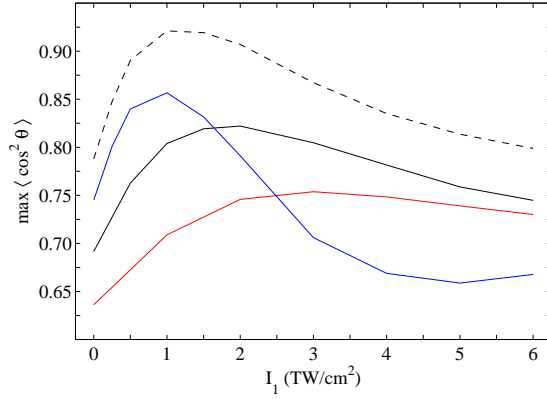


Figure 5.7: Numerically calculated optimum degree of two-pulse alignment as function of the intensity in the first pulse. The pulse duration was: (red curve) 0.5 ps (solid black curve) 1 ps and (blue curve) 2 ps. The dashed black curve represents the results for a 1 ps calculation where focal volume averaging was omitted. I_2 is kept fixed at 6×10^{12} W/cm² and the second pulse is sent when the degree of alignment due to the first pulse peaks.

case. In the 0.5 ps case the curve is found to be almost flat as the intensity of the first pulse approaches that of the second pulse, in good agreement with our experimental findings. When comparing the dashed and solid black lines we see a huge impact from the focal volume averaging. The shapes of the curves are quite similar, but the best alignment is reduced from $\langle \cos^2 \theta \rangle = 0.92$ to 0.82 as the averaging is included. The reason is that the alignment dynamics depend on the intensity of the alignment pulse and hence different regions of the focal volume peaks in alignment at different delays. The observed alignment is therefore only an average of the intensities probed in the focal volume. Additionally, for the two-pulse alignment, the optimum delay between the alignment pulses can not be the same for the whole of the focal volume, resulting in a further reduction of the degree alignment due to focal volume averaging. From Fig. 5.7 it is clear that the measured degree of nonadiabatic alignment can be significantly improved by minimizing focal volume averaging. This can be done experimentally by improving the confinement of the probe pulse or by selecting a probe that is nonlinear in the intensity, like the Coulomb explosion probe, so that a smaller part of the focal volume of the alignment pulses is probed. A large impact from focal volume averaging was expected in the experiments on *tert*-butyliodide since the probe pulse width was almost as large as the alignment pulse width ($\omega_0^{probe} = 20\mu\text{m}$, $\omega_0^{align} = 25\mu\text{m}$) and since the linear dissociation probe was used.

In conclusion we found both experimentally and theoretically that the strongest

degree of alignment obtainable with at single pulse can be significantly enhanced by using two alignment pulses. Optimum pulse durations, intensities and relative timings were found for the symmetric top molecule *tert*-butyliodide.

CHAPTER 6

Experimental Results III: Adiabatic Alignment

Adiabatic alignment has been established theoretically [4, 26] as well as experimentally [24, 53, 57, 58] and is by itself not a goal for us to further investigate. However, due to its simplicity it serves very well as a test of the new vacuum system and Even-Lavie valve. In this chapter a series of adiabatic alignment experiments, conducted at different stagnation pressures of the buffer gas, will be presented. Through these experiments we will test the Even-Lavie valves ability to vary the rotational temperature of the sample and estimate the lowest obtainable rotational temperature. The valves ability to supply samples of relatively large molecules (20+ atoms) by increasing the temperature of the valve body is also tested. An additional reason for undertaking adiabatic alignment experiments was to prepare for experiments where adiabatic alignment techniques are used in combination with nonadiabatic alignment to obtain 3D alignment (see Chapter 7).

In the experiments presented in this chapter the Nd:YAG laser (1064 nm, 10 ns, 20 Hz) was used to align the sample and the resulting alignment was probed with a linearly polarized Coulomb explosion pulse (800 nm, 130 fs or 30 fs). The experiments were conducted in the new vacuum system with the Even-Lavie valve.

6.1 One Dimensional Adiabatic Alignment

A series of experiments were conducted to illustrate the crucial role of the initial rotational temperature on the degree of adiabatic alignment and to test the Even-Lavie valves ability to supply rotationally cold molecular samples in a large tem-

perature interval. The experiments were conducted on a series of asymmetric top molecules, all containing atoms located on the most polarizable molecular axis, that are easily identifiable in a mass/charge spectrum. Upon multiple ionization by the probe laser these atoms are converted to ions, whose recoil along the most polarizable molecular axis make them useful experimental observables for identifying the spatial orientation of this axis (see Sec. 3.2.2). The molecules studied are: iodobenzene, *p*-diiodobenzene [C₆H₄I₂], 3,4-dibromothiophene (DBT) [C₄H₂SBr₂] and 4,4'-dibromobiphenyl (DBBP) [C₁₂H₈Br₂]. For all of these molecules adequate ion signal was obtained by heating the valve body to 32, 80, 60 and 145 °C for the mentioned molecular species, respectively. To our estimates the vapour pressures were on the order of a few mbar at these temperatures, sufficiently low to avoid cluster formation of the sample molecules. As the temperature can be raised all the way to 250 °C we suspect that samples of even larger molecules can be supplied by this valve.

The probe used in these experiments was a 130 fs, 800 nm pulse with an intensity of 6×10^{13} W/cm². It was focused to a slightly smaller spot size than the Nd:YAG pulse ($\omega_0^{1064} = 30 \mu\text{m}$ and $\omega_0^{800} = 26 \mu\text{m}$). We choose to polarize the Coulomb explosion probe perpendicular to the plane of the detector. This means that ion images of isotropically distributed molecules should be circular symmetric. The Nd:YAG laser was linearly polarized parallel to the detector plane making the most polarizable molecular axis (which for these molecules also is the principal molecular symmetry axis) align in the detector plane perpendicular to the probe polarization. From imaging fragments of I⁺ for iodobenzene and *p*-diiodobenzene, S⁺ for DBT and Br⁺ for DBBP, information about the orientation of the principal molecular symmetry axis can be extracted. As a high degree of alignment is expected, in particular at the lowest temperatures studied, angular selectivity of the probe will be minimized since the principal molecular symmetry axis will be oriented nearly perpendicular to the probe polarization.

In Fig. 6.1 the molecular structure of each of the molecules is shown in combination with two rows of false-color ion images, one recorded in the absence of the Nd:YAG alignment laser and one recorded with the Nd:YAG alignment laser. These images were recorded under the coldest possible sample conditions and, for the aligned images, at the highest intensity of the Nd:YAG laser the molecules could withstand without ionizing. The middle row shows ion images recorded with the probe pulse alone. Circular symmetry is observed as expected, indicating random molecular orientation and that the probe polarization is well confined perpendicular to the plane of the detector. A very intense spot in the center of the iodobenzene, DBT and DBBP image has been removed for clarity. Since it is centered (i.e. has zero recoil kinetic energy) it must originate from a molecular ion. The spot in the DBT images consists of O₂ contamination in our high pressure system, delivering the helium buffer gas to the valve. Since the O₂⁺ ion has the same mass/charge ratio as S⁺ it can not be avoided. In the bottom row the ion images recorded with the Nd:YAG laser included are shown. Its polarization is along the vertical axis in these images. Very strong con-

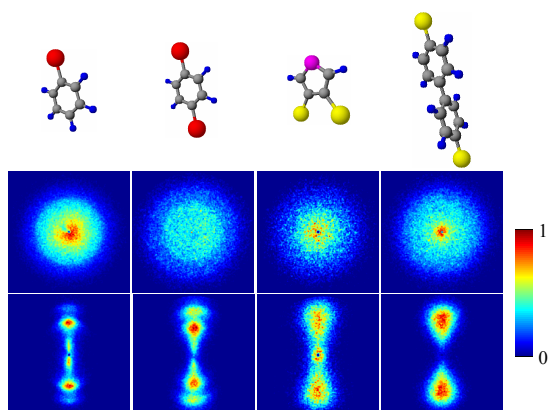


Figure 6.1: The top row shows the molecular structure of the examined molecular species. Iodobenzene, *p*-diiodobenzene, DBT and DBBP in the 1st, 2nd, 3rd and 4th column respectively. Ion images recorded with the Coulomb explosion probe alone, polarized perpendicular to the detector plane are shown in the middle row. In the bottom row the Nd:YAG laser has been added, polarized in the detector plane (vertically in the images). The color scale to the right indicate the relative number of ion hits.

finement of the recoiling ions along the Nd:YAG laser polarization axis is observed for all four molecular species investigated. As the probe is unbiased in the detector plane this confinement can only be attributed to strong alignment of the principal molecular symmetry axis, along the Nd:YAG laser polarization, prior to the arrival of the probe pulse.

To quantify the alignment $\langle \cos^2 \theta_{2D} \rangle$ is used. The iodobenzene and *p*-diiodobenzene ion images show two distinct radial channels, with center radii of 143 & 205 and 121 & 194 pixels respectively. For these molecules the outer channel is used to calculate $\langle \cos^2 \theta_{2D} \rangle$. For DBT and DBBP no distinct radial channels are observed and $\langle \cos^2 \theta_{2D} \rangle$ is calculated from ion hits in the radial range corresponding to the drop like shapes in the ion images. The radius ratio for the iodobenzene channels equals the square root of two, which corresponds nicely to generation of a singly charged iodine ion in combination with either a singly or doubly charged phenyl ion.

We are now ready to investigate how the alignment depends on the intensity of the Nd:YAG laser pulse and the rotational temperature of the sample. Figure 6.2 summarizes the results for all four molecular species. Experiments were conducted at stagnation pressures up to 100 bar for all molecular species, however, if the alignment did not improve further at pressures above the highest shown in Fig. 6.2 the data was omitted. In the experiments on iodobenzene and DBT the maximum alignment laser intensity was determined by the highest energy we dared sending through the vac-

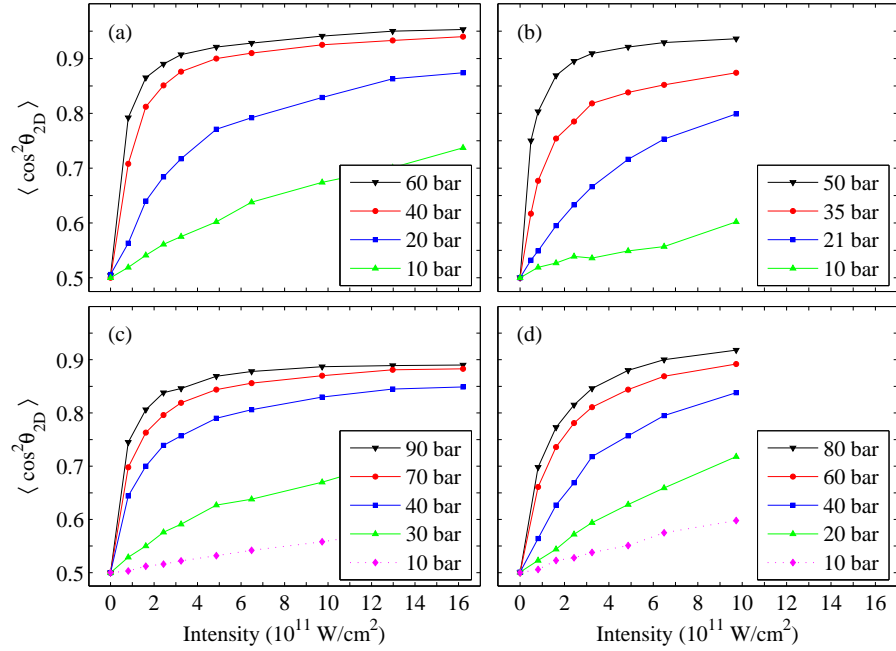


Figure 6.2: $\langle \cos^2 \theta_{2D} \rangle$ values recorded at different intensities of the Nd:YAG laser and different stagnation pressures of helium for (a) iodobenzene, (b) *p*-diiodobenzene, (c) DBT and (d) DBBP.

uum viewports, however for *p*-diiodobenzene and DBBP, ionization started to occur at intensities above $1 \times 10^{12} \text{ W/cm}^2$ and experiments were therefore not conducted at intensities higher than this limit.

From all four molecular species the crucial role of the temperature on the degree of alignment is observed. The alignment at the maximum intensity but lowest stagnation pressure is second to that measured at the highest stagnation pressure, at an order of magnitude lower intensity. For instance, in the case of iodobenzene at 60 bar stagnation pressure and an intensity of $1.6 \times 10^{11} \text{ W/cm}^2$ the degree of alignment is $\langle \cos^2 \theta_{2D} \rangle = 0.865$, however, if the stagnation pressure is decreased to 10 bar the degree of alignment does not go higher than 0.737, even at the maximum intensity of $1.6 \times 10^{12} \text{ W/cm}^2$.

The intensity dependence of the degree of alignment is similar to previously published results [53, 58]. Most noticeable is the saturation effect that is apparent for all four molecular species in the highest pressure results. Here even relatively weak fields ($\sim 2 \times 10^{11} \text{ W/cm}^2$) are able to produce very good alignment, which could

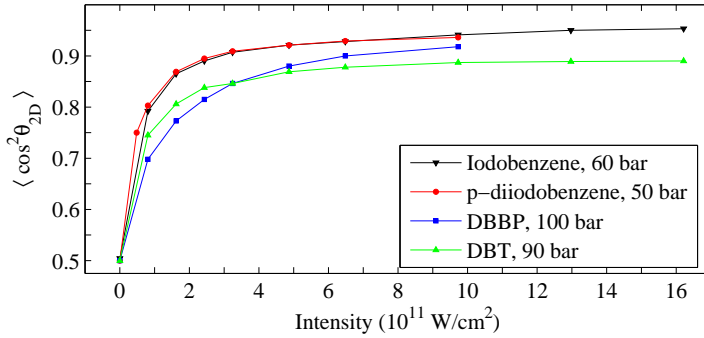


Figure 6.3: Measured degree of alignment at the optimum pressure conditions (i.e. lowest attainable rotational temperature). Saturation in the degree of alignment for DBT is observed around $3 \times 10^{11} \text{ W/cm}^2$ with a $\langle \cos^2 \theta_{2D} \rangle$ value of only 0.85.

be important for experiments where high degrees of alignment are desired, but disturbances from the alignment laser field must be minimized. The highest $\langle \cos^2 \theta_{2D} \rangle$ values obtained are 0.95, 0.94, 0.89 and 0.92 for iodobenzene, *p*-diiodobenzene, DBT and DBBP, respectively. These values show that exceptionally good alignment can be obtained by using adiabatic alignment techniques as long as the rotational temperature of the sample is low.

We can compare the results for iodobenzene with the results presented in Sec. 4.2.2, since a similar probe technique was used. The highest degree of field-free non-adiabatic alignment was $\langle \cos^2 \theta_{2D} \rangle = 0.760$, obtained immediately after the turn off of the 2.0 ps pulse. The highest measured degree of nonadiabatic alignment was $\langle \cos^2 \theta_{2D} \rangle = 0.834$, measured during the 2.0 ps pulse. Clearly the alignment obtainable in adiabatic alignment is far superior to that of nonadiabatic alignment.

From the iodobenzene results we have estimated the rotational temperature of the sample molecules to be below 1.5 K for the highest stagnation pressures and about 40 K for the lowest stagnation pressures [29], in very good agreement with what has previously been published for the Even-Lavie valve [37, 38]. These results show that we through this valve can control the rotational temperature of the sample in a large interval and that we can obtain rotational temperatures down to about 1 K.

When comparing the curve shapes for the lowest temperature experiments of the four molecular species the DBT results stand out (see Fig. 6.3). First of all the alignment starts saturating at a relatively low degree of alignment ($\langle \cos^2 \theta_{2D} \rangle \sim 0.85$), and furthermore the following curve flattening is more pronounced than for the other species. This results in a lower observed maximum degree of alignment ($\langle \cos^2 \theta_{2D} \rangle = 0.89$) than for the three other molecular species. The size of the DBT molecule is com-

parable to that of iodobenzene and *p*-diiodobenzene, so similar cooling is expected. As the polarizability of DBT is almost identical to that of iodobenzene [17, 59] we see no reason not to expect similar alignment for these two species. We believe that the lower readings for DBT are caused by nonaxial recoil of the S^+ ions in the Coulomb explosion process. The degree of alignment may very well be as high as for iodobenzene, however, the observed degree of alignment is limited by the recoil distribution. Nonaxial recoil is more likely to happen for DBT, than for the other molecular species investigated, since the sulphur atom is embedded in the aromatic ring, rather than connected to the molecule via a single bond.

6.2 Three Dimensional Adiabatic Alignment

The vast majority of alignment experiments so far were carried out on diatomic or linear triatomic molecules [46, 58, 60–62] where only one dimensional alignment is relevant. Very few studies have been conducted on asymmetric top molecules and hence three dimensional (3D) alignment is as of yet relatively unexplored. Larsen *et al.* [59] was first to report on 3D alignment in 2000; Here an elliptically-polarized Nd:YAG pulse was used to confine the two most polarizable molecular axes of 3,4-dibromothiophene molecules. Since the molecule is rigid the third, orthogonal, axis is automatically confined and consequently 3D alignment is obtained. This experiment was extended to 3D orientation by Tanji *et al.* [63] in 2005. Recently, 3D alignment was demonstrated both theoretically and experimentally using two orthogonally-polarized nonadiabatic alignment pulses [64, 65]. This approach enables 3D alignment under field-free conditions, however, the observed alignment was very weak.

To prepare for other 3D alignment experiments (see Chapter 7) we decided to redo the experiments of Larsen *et al.*, however with a few critical improvements. First of all, the Even-Lavie valve enables us to do experiments on very cold molecules, significantly improving the angular confinement. Also the new setup produces images of higher quality giving clearer evidence for alignment. Finally, as discussed earlier, 3,4-dibromothiophene is not an ideal candidate for ion imaging, since no clear Coulomb explosion channels are observed and, additionally, the degree of alignment is possibly underestimated due to nonaxial recoil. An asymmetric top molecule is naturally required for 3D alignment experiments, however, the molecule must also contain parts that can easily be identified and separated in the mass/charge spectrum. For these reasons none of the previously explored molecules were considered suitable for investigating 3D alignment on our experimental setup. As iodobenzene has proven itself as a good candidate due to its polarizability, rotational constants and vapour pressure at room temperature we decided to try 3,5-difluoroiodobenzene (DFIB) [$C_6H_3F_2I$], for which these parameters are expected to be quite similar. For this molecule I^+ and F^+ fragment ions are useful observables since they are expected to recoil along the

principal molecular symmetry axis (the C-I bond axis) and in the plane of the molecule, respectively. Also, we would expect to see Coulomb explosion channels with relatively well defined velocities, which help us to obtain ion images that are easily interpreted.

Experimentally, polarization control of the Nd:YAG laser was obtained with a half-wave plate positioned in front of a quarter-wave plate. The alignment was probed by a Coulomb explosion pulse with 30 fs duration (FWHM) and an intensity of 3×10^{14} W/cm². In order to only probe the best aligned molecules the focus of the probe was kept much smaller than the focus of the Nd:YAG laser (ω_0 of 30 μm and 50 μm respectively). All experiments were conducted at a 100 bar stagnation pressure to ensure maximum cooling.

Recorded mass/charge traces of DFIB are shown in Fig. 6.4. Each curve is obtained from averaging over 500 laser shots with extraction voltages of 4500 V and 3010 V for the repeller and extractor respectively. The time interval shown is truncated at 4.9 μs to focus on the fragment ions, however, the $\text{C}_6\text{H}_4\text{F}_2\text{I}^+$ ion is observed at 6.2 μs . Much knowledge of the Coulomb explosion probe can be extracted from these curves, in particular the detailed shape of a single ion peak can reveal information about the velocity distribution of the generated ions. Ions initially ejected backwards, away from the detector, will arrive later than ions ejected towards the detector. Naturally, ions ejected with velocities parallel to the detector will arrive in between. Clear differences are seen in the two iodine ion peaks (I^+ at 4.6 μs and I^{2+} at 3.4 μs) of Fig. 6.4 (a), revealing the selectivity of the probe. In the black curve (Coulomb explosion probe polarized perpendicular to the detector) the ion peak is split into two, indicating that most I^+ ions recoil either towards or away from the detector. In contrast, in the magenta curve (polarization parallel to the detector) the ion peak is a single centered peak, meaning that the ions recoil either uniformly or primarily in the detector plane. When comparing the two, the magenta is seen to be narrower than the black, indicating that fewer ions recoil perpendicular to the detector for this polarization. Since the molecular sample is uniformly distributed we can conclude that the nonuniform I^+ ion recoil distribution results from angular selectivity of the probe; The production of I^+ ions is a function of the angle between the probe polarization and the C-I axis, with the ion yield being maximized in the parallel geometry case [66, 67].

Turning to Fig. 6.4 (b), striking changes are observed when the Nd:YAG laser is included. In this spectrum the Coulomb explosion probe polarization is fixed perpendicular to the detector. When the Nd:YAG pulse is polarized parallel to the detector (red curve), a significant narrowing in the I^+ signal is observed. Since no ions are generated by the Nd:YAG laser alone this can only be a result of a molecular distribution where the C-I axis is primarily located parallel to the detector. When the polarization of the Nd:YAG laser is perpendicular to the detector (blue curve), the I^+ signal is observed to split up into two separated peaks. No signal is observed in between them meaning that the C-I axis is confined perpendicular to the detector. By comparing the iodine ion signals (I^+ , I^{2+} and I^{3+}) between the two different Nd:YAG pulse

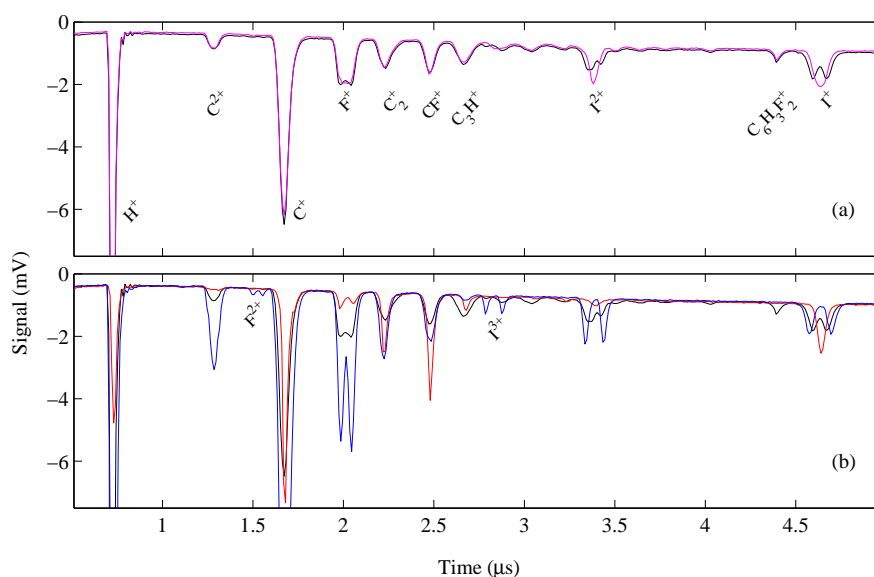


Figure 6.4: Mass/charge readout from the MCP of 3,5-difluoriodobenzene. All peaks are labeled with the corresponding ion. For increased resolution the molecular ion signal located at $6.2 \mu\text{s}$ is not included. (a) Coulomb explosion pulse only; Polarization is perpendicular and parallel to the detector for the black and magenta curve respectively. (b) Coulomb explosion pulse polarized perpendicular to the detector in all curves. The black curve is Coulomb explosion pulse alone. In the blue and the red curve the Nd:YAG laser is added and polarized perpendicular and parallel to the detector respectively.

polarizations we see that higher charge states are suppressed when the alignment is perpendicular to the probe polarization and increased when they are parallel. These changes in the mass/charge spectrum are a clear indication of alignment of the C-I axis along the polarization axis of the Nd:YAG pulse. In the F^+ ion signal (located at $2 \mu\text{s}$), we observe a much more dramatic angular dependency. Here a factor of 10 more ions are produced when the probe polarization is parallel to the molecular C-I axis (blue curve) as opposed to perpendicular (red curve), in fact the F^+ ion signal is nearly fully suppressed in the perpendicular geometry. From this we note that it can be quite tricky to use the Coulomb explosion probe for measuring the orientation of the molecular plane, since the F^+ ion yield is highly orientational dependent. Care must be taken to avoid probing an angular subset of molecules, which potentially could offset the measured degree of alignment. Based on our results from 1D adiabatic alignment in the previous section, we expect to obtain a high degree of angular confinement of the

C-I axis, even under the conditions where the Nd:YAG laser is elliptically polarized. When imaging F^+ ions we therefore keep the polarization of the Coulomb explosion laser parallel to the major axis of the Nd:YAG laser polarization, in order to minimize the effects of angular selectivity. For the I^+ ions, where the angular selectivity is less pronounced, we kept the polarization of the Coulomb explosion laser perpendicular to the detector plane as in the 1D adiabatic alignment experiments.

Even though the ion species arrive within a relatively short time interval the F^+ ion signal is sufficiently isolated for ion gating of the MCP with a 100 ns and 50 ns separation to the C^+ and C_2^+ ions. For imaging of I^+ ions lower extraction voltages were used to utilize more of the detector area, since these ions recoil with lower velocities. This has no effect on the iodine ion angular distribution, only the timing of the ion impact is changed.

As we move from 1D alignment to 3D alignment of molecules, cylindrical symmetry in the angular distribution of the molecules is lost and a single projection of ion velocities may therefore be misleading as out of projection-plane asymmetry will be hard to observe and quantify. To improve our observations we decided to record two different 2D ion velocity projections of the aligned distributions. Figure 6.5 shows examples on how we expect the aligned molecules to be distributed along with experimentally recorded images of I^+ and F^+ ions for two different 2D projections. The case of 1D alignment, where one molecular axis is confined and the molecule is free to rotate about this axis, is depicted in the left column. Our usual experiments where the Nd:YAG laser is polarized in the plane of the detector is depicted in the first row ($I_{\text{Nd:YAG}} = 7 \times 10^{11} \text{ W/cm}^2$). Here the recorded I^+ ion image, (a), shows the expected localization of the I^+ ions along the vertical axis. The F^+ ion image, (b), is at first sight harder to interpret. With perfect linear alignment one would expect a doughnut like shape in the F^+ velocity distribution as the molecules are free to rotate. This is indeed compatible with what is observed in image (b) as this image correspond to the projection of the doughnut from the side. The two horizontal line-like shapes originate from the "side" projection of the two doughnut shapes that we expect to see, from the two equally likely pointing directions of the sample molecule. Due to the strong confinement of the C-I axis along the vertical axis in the detector plane this projection can be regarded as a "side view" of the molecules. Note that the Coulomb explosion probe in the side view F^+ ion image is polarized in the detector plane, since it is kept parallel to the Nd:YAG laser polarization. If we instead set the polarization of the Nd:YAG laser perpendicular to the plane of the detector the molecules will be confined with their C-I axis perpendicular to the detector. Ion images recorded under these conditions will be referred to as "end views" since the "ends" of the molecules point towards the detector. In the end view projection the I^+ ion image should have a circular shape and be well confined to the center of the image, as the recoil for the I^+ ions is expected to be directly towards or away from the detector. The F^+ ion image should have a the circular doughnut shape with no signal near the center. From image

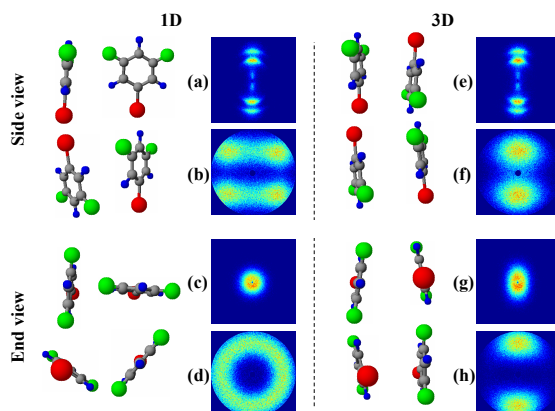


Figure 6.5: Ion images in combination with molecular models illustrating the spatial orientation. Side views (top row) are obtained by orienting the major polarization axis of the Nd:YAG laser in the detector plane and end views (bottom row) by orienting it perpendicular to the detector plane. In the left column the Nd:YAG laser is linearly polarized; In the right it is elliptically polarized with a 2:1 intensity ratio in the major and minor axis respectively. Image (a), (c), (e), (g) are I^+ ion images and (b), (d), (f), (h) are F^+ ion images.

(c) and (d) we see that the ion images indeed reveal the expected structure. An intense spot located at the very center of all our F^+ ion images, originating from water in the gas supply system, has been removed for clarity.

The real strength in the set of 2D projections of ion velocity distributions is revealed when 3D alignment is measured. The second column in Fig. 6.5 show the same projections as the first column, however with the Nd:YAG elliptically polarized with an intensity of $4.6 \times 10^{11} \text{ W/cm}^2$ and $2.3 \times 10^{11} \text{ W/cm}^2$ along the major and minor axis respectively (2:1 intensity ratio). When comparing the I^+ side view images [(a) and (e)] it is hard to see any difference. Clear differences are, however, observed in the I^+ end view images [(c) and (g)], where the Nd:YAG laser polarization has been rotated so that the major polarization axis is pointing into the detector and the minor axis is parallel to the detector along the vertical axis in the image. In image (g) the I^+ ions are no longer circularly symmetrically distributed as in image (c), instead, an elongated shape along the vertical direction is observed. The cylindrical symmetry in the angular distribution of the C-I axis is clearly broken. The asymmetry towards the vertical axis in the end view image is expected since it is the direction of the minor axis of the Nd:YAG laser polarization. The C-I axis is, however, still well confined as can be confirmed by comparison with an image from an unaligned sample [Fig. 6.6

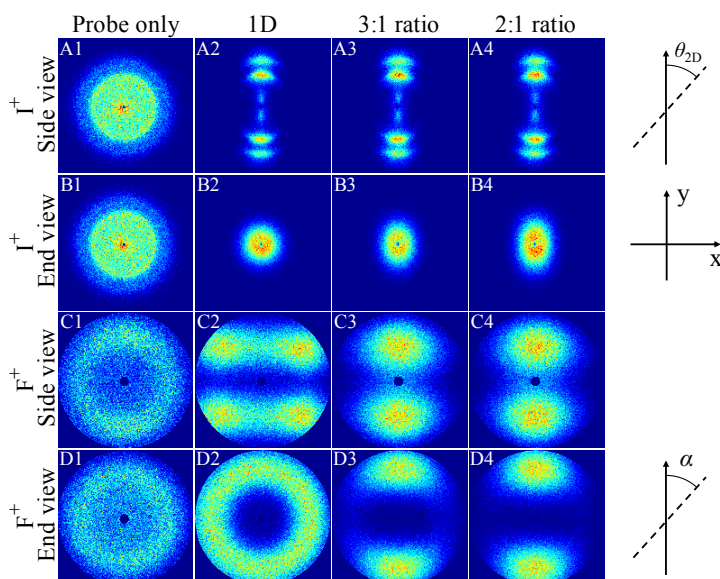


Figure 6.6: Ion images of I^+ and F^+ fragments in both side and end views. Column 1 (probe only) serve as reference images. The total Nd:YAG intensity in column 2-4 is fixed at 7×10^{11} W/cm², the eccentricity is however varied (linear (1D), 3:1 and 2:1 intensity ratio respectively).

(B1)]. Turning to the F^+ ion images [Fig. 6.5 image (f) and (h)] dramatic changes are observed. Most clearly the doughnut shape found in image (d) is replaced by localization along the vertical axis in image (h). This is a clear indication of confinement of the molecular plane to the plane spanned by the polarization of the Nd:YAG laser pulse. In combination with the high C-I axis confinement observed in image (g) we can conclude that good 3D alignment of the 3,5-difluoriodobenzene molecules has been established in the elliptically polarized Nd:YAG laser field. Images (e) and (f) supports the conclusion of good 3D alignment. Here the molecules are confined with their plane perpendicular to the detector plane and their C-I axis along an axis parallel to the detector, vertically in the images.

An additional experiment was conducted with a different polarization eccentricity for the Nd:YAG pulse. The total intensity was unchanged and the intensity ratio was set to 3:1. The results are shown in Fig. 6.6 together with the images from Fig. 6.5. A set of images taken with the Coulomb explosion probe alone is also included for reference. From the two sets of images recorded with elliptically polarized Nd:YAG laser (column 3 and 4) it is obvious that the increased confinement in the molecular plane comes at a cost in the confinement of the C-I axis (compare B3 and B4 with

	$\langle \cos^2 \theta_{2D} \rangle$	$\langle \cos^2 \alpha \rangle$	$\langle y \rangle$	$\langle x \rangle$
Probe only	0.504	0.502	84	84
1D	0.923	0.500	49	48
3:1 ratio	0.925	0.727	56	43
2:1 ratio	0.924	0.780	62	43

Table 6.1: Measures for the degree of alignment. Calculated from the images shown in Fig. 6.6. The uncertainties are estimated to ± 0.005 for $\langle \cos^2 \theta_{2D} \rangle$ and $\langle \cos^2 \alpha \rangle$ and ± 1 for $\langle y \rangle$ and $\langle x \rangle$.

B2). To quantify the degree of alignment of the molecular plane we use the angular distribution of the F^+ ion velocities from the end view projection. Here, the angle between the minor axis of the Nd:YAG polarization and the ion impact on the detector is termed α and the degree of alignment is quantified by the value of $\langle \cos^2 \alpha \rangle$. This measure is similar to $\langle \cos^2 \theta_{2D} \rangle$ where θ_{2D} is the angle in the side view projection. For an uniform distribution of the molecular plane the value of $\langle \cos^2 \alpha \rangle$ is 0.5, alignment of the molecular plane along (perpendicular to) the minor polarization axis will result in a value higher (lower) than 0.5. Our standard way of quantifying the alignment of the principal molecular symmetry axis via $\langle \cos^2 \theta_{2D} \rangle$, from the side view image, is not adequate for 3D alignment experiments, since it is insensitive to angles perpendicular to the detector (noncylindrical symmetry). From the end view projection any such deviations are however easily detected and must be included in order to evaluate the alignment. To quantify these deviations we evaluate the I^+ ion velocity components in the end view projection. The measure is given in the average pixel distance from the image center along the vertical $\langle y \rangle$ and horizontal $\langle x \rangle$ axis (see Fig. 6.6 for axes).

Table 6.1 contain the four measures for the degree of alignment obtained from the images in Fig. 6.6. $\langle \cos^2 \theta_{2D} \rangle$ is calculated from the outer I^+ ion channel in the side view images, $\langle \cos^2 \alpha \rangle$ from the range corresponding to the intense area in image D2 in the F^+ end view images and finally $\langle y \rangle$ and $\langle x \rangle$ from the whole of the I^+ end view images. The values extracted from the probe only images indicate good probe conditions as they, within the uncertainty, correspond to what is expected for a uniformly distributed sample. From the experiment with linearly polarized Nd:YAG laser (1D) a high degree of alignment is observed for the C-I axis ($\langle \cos^2 \theta_{2D} \rangle = 0.923$) and the molecular plane is indeed uniformly distributed ($\langle \cos^2 \alpha \rangle = 0.5$). Also no asymmetry is observed in the I^+ end view ion image ($\langle y \rangle \sim \langle x \rangle$). Turning to the images recorded with the elliptically polarized Nd:YAG laser we observe no degradation in the $\langle \cos^2 \theta_{2D} \rangle$ values however, the $\langle y \rangle$ and $\langle x \rangle$ values clearly indicate decreased confinement of the C-I axis. This confirms our initial assumption that one 2D projection of the recoil velocities is insufficient for characterizing alignment of the principal molecular symmetry axis in 3D alignment experiments. From the images in Fig. 6.6 and the values in Table 6.1 we conclude that good 3D alignment is achieved using adiabatic

alignment with elliptically polarized pulses. However, there is a trade off between the confinement of the principal molecular symmetry axis and the molecular plane. The improved confinement of the molecular plane, obtained by increasing the intensity in the minor axis of the polarization ellipse, comes at a cost in the confinement of the principal molecular symmetry axis.

CHAPTER 7

Experimental Results IV: 3D alignment by combining adiabatic and nonadiabatic alignment

From our experiments on adiabatic 3D alignment we observed a trade off between the confinement of the most polarizable molecular axis and the molecular plane. As the eccentricity was reduced in order to improve the confinement of the molecular plane, a decrease in the confinement of the most polarizable molecular axis was observed. As a new approach to reduce the impact on the confinement of the most polarizable molecular axis we suggest combining the techniques of adiabatic and nonadiabatic alignment. The idea is to adiabatically align the most polarizable molecular axis with the Nd:YAG laser and then excite rotation about the aligned axis with a nonadiabatic kick pulse. By having the two laser pulses linearly polarized perpendicular to each other, the most polarizable molecular axis will be fixed almost perpendicular to the kick pulse, due to the strong axial confinement along the Nd:YAG laser polarization axis. The perpendicular polarization geometry essentially eliminates the interaction between the kick pulse and the most polarizable molecular axis, leaving the 1D alignment virtually undisturbed. Instead, the kick pulse interacts with the axis of second highest polarizability and sets the molecule into controlled rotation about the aligned molecular axis. Just as for 1D nonadiabatic alignment this results in angular confinement shortly after the kick pulse, however, here it is the axis of second largest polarizability that aligns along the kick pulse polarization. As the most polarizable molecular axis remains confined along the Nd:YAG pulse polarization, 3D alignment is expected to occur shortly after the interaction with the kick pulse. Furthermore, 3D alignment revivals are expected due to the quantum nature of the rotational excitation,

reflecting the revolution about the most polarizable molecular axis. The cornerstone of this method is to combine the best properties from the two different laser induced alignment techniques; The exceptional 1D confinement obtainable only through adiabatic alignment and the ability to initiate controlled rotational motion with short pulses in the nonadiabatic limit. This is combined in an effort to avoid the relatively large impact on the confinement of the most polarizable molecular axis observed in adiabatic 3D alignment.

7.1 Preliminary experiments on 3,4-dibromothiophene

Preliminary experiments, completed prior to those presented in Chapter 6, were undertaken on 3,4-dibromothiophene (DBT). The experiments were conducted in the old vacuum system with the Jordan valve supplying the sample, this means that the 1D alignment from the Nd:YAG laser pulse would be good, however not as impressive as the results presented in Chapter 6. Three pulsed laser beams were used for this experiment. The first laser beam, originating from the Nd:YAG laser (1064 nm, 10 ns, 1.4×10^{12} W/cm², $\omega_0 = 35$ μ m), adiabatically aligns the most polarizable molecular axis (which for DBT is the C₂ symmetry axis) along its polarization axis. At the peak of the Nd:YAG pulse the kick pulse (800 nm, 0.7 ps, 10×10^{12} W/cm², $\omega_0 = 33$ μ m) is sent in to induce rotation about the aligned axis. The kick pulse is polarized perpendicular to the Nd:YAG laser pulse. The third laser pulse is the Coulomb explosion pulse (800 nm, 25 fs, 2.6×10^{14} W/cm², $\omega_0 = 23$ μ m) which is sent at a controllable delay, t , with respect to the kick pulse.

Ion images of S⁺ and Br⁺ were recorded in order to obtain information about the orientation of the molecular C₂ symmetry axis and the molecular plane respectively. An image series recorded at different delays is shown in Fig. 7.1. Images taken with the Coulomb explosion probe alone (Fig. 7.1 A1 and B1) and with Coulomb explosion probe and Nd:YAG pulse (Fig. 7.1 A2 and B2) are included for reference. For the S⁺ ion images the Nd:YAG and the Coulomb explosion laser were polarized in the plane of the detector (vertically in the images) and the kick pulse was polarized perpendicular to the plane of the detector. In the Br⁺ ion images all polarizations were rotated 90°, orienting the polarization of the Nd:YAG and the Coulomb explosion laser perpendicular to the plane of the detector and the kick pulses in the plane of the detector (vertically in the images). In case of good confinement of the molecular C₂ symmetry axis, the S⁺ ion images corresponds to side views of the molecules and the Br⁺ ion images to end views.

Figure 7.1 A1 shows the S⁺ ion image when only the Coulomb explosion probe is used. The minor angular localization along the probe polarization axis reflects the enhanced ionization rate for DBT molecules with their C₂ symmetry axis oriented along the probe polarization. When the Nd:YAG pulse is included (Fig. 7.1 A2), the angular localization sharpens, due to adiabatic alignment of the C₂ symmetry axis

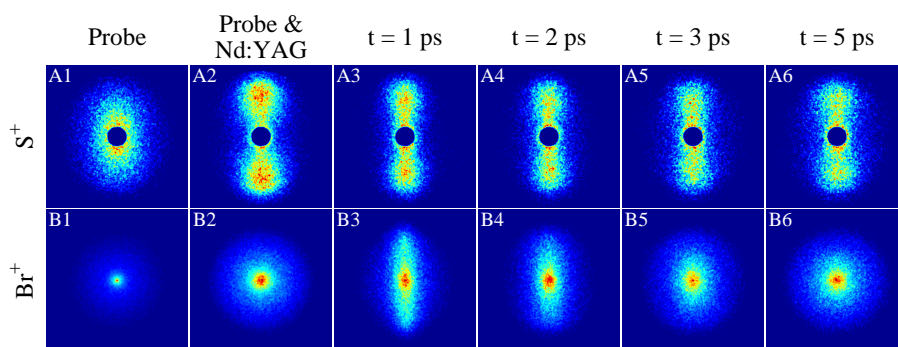


Figure 7.1: Ion images from DBT of S^+ and Br^+ . The intensities were 1.4×10^{12} W/cm², 10×10^{12} W/cm² and 2.6×10^{14} W/cm² for the Nd:YAG, kick and Coulomb explosion laser pulse respectively. The central part of the S^+ images has been removed to avoid displaying thermal O_2^+ ions, originating from ionization of chamber background.

along the Nd:YAG laser polarization. Turning to the Br^+ ions it is seen that the images with (Fig. 7.1 B2) and without (Fig. 7.1 B1) the Nd:YAG pulse are both circularly symmetric, showing that the molecular plane is free to rotate around the Nd:YAG polarization axis. As we include the kick pulse, the Br^+ images change dramatically. At very early times (Fig. 7.1 B3) the ion distribution emerges as a narrow line along the direction of the kick pulse polarization. At longer times this confinement quickly disappears and a circularly symmetric distribution is restored already around $t = 5$ ps. The observation at $t = 1$ ps is only compatible with the Br^+ ions being ejected in the plane defined by the Nd:YAG pulse and the kick pulse polarizations, i.e. alignment of the molecular plane to the space-fixed plane, spanned by the polarizations of the two laser pulses. The S^+ image at $t = 1$ ps shows that the C_2 symmetry axis is still aligned along the Nd:YAG laser polarization (Fig. 7.1 A3). Thus, we conclude that significant 3D alignment, corresponding to simultaneous confinement of the molecular plane and the C_2 symmetry axis to space-fixed axes, is achieved at $t = 1$ ps.

From the top row of Fig. 7.1 it is clear that the kick pulse disturbs the confinement of the C_2 symmetry axis, the changes are however hard to quantify since no distinct radial recoil channels are observed for the S^+ ions. In the bottom row we observe that the alignment of the plane peaks immediately after the kick pulse. This indicates that the total kick energy is quite high and that equal or nearly as good alignment can be obtained with lower kick energy. This would be an advantage since the disturbance in the confinement of the C_2 symmetry axis would be reduced and better 3D alignment may be obtained in this way.

While the images shown in Fig. 7.1 indicate 3D alignment, they are not as unambiguous as we had hoped. The fact that the Coulomb explosion channels are not well

confined radially, means that clear distinction between a planar aligned distribution^a and 3D alignment is hard to make. One way to eliminate this ambiguity is to perform similar experiments on a molecule with clearly resolved Coulomb explosion channels.

In the search for a more suitable candidate molecule several criteria needed to be fulfilled. As mentioned above clearly resolved Coulomb explosion channels are essential for extracting more information about the angular distribution of the molecules. Equally important is the inertia and polarizability tensors, that determine the molecular rotation following the nonadiabatic kick. Good 1D confinement in the Nd:YAG laser field requires that the polarizability of the most polarizable molecular axis is significantly higher than the other two. This is readily seen from Eq. (2.4) which, when averaged over χ , reduces to:

$$\hat{H}_{int} = -\frac{1}{4} \varepsilon^2(t) [\alpha_{zz} - \frac{1}{2}(\alpha_{xx} + \alpha_{yy})] \cos^2 \theta \quad (7.1)$$

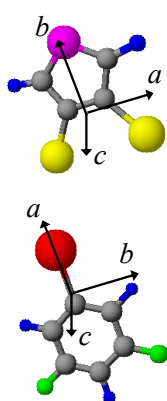
apart from an angle-independent term. For an effective alignment of the molecular plane through the kick pulse, there must also be a significant difference in the polarizabilities along the two lower polarizability axes. In the limit of perfect 1D alignment of the most polarizable axis along the Nd:YAG pulse polarization axis, the interaction with the kick pulse is:

$$\hat{H}_{int,\perp} = -\frac{1}{4} \varepsilon_{kick}^2(t) (\alpha_{yy} - \alpha_{xx}) \cos^2 \chi \quad (7.2)$$

This is derived from Eq. (6.3) in [30] by setting $\theta = \pi/2$ and $\phi = \pm\pi/2$ and only focusing on the field from the kick pulse [$E_X^2 = \varepsilon_{kick}^2(t)$]. As can be seen in Table 7.1 the polarizability tensor of DBT is indeed asymmetric in this way. When the inertia is considered we see that DBT is a less suited candidate. Classically the kick strength is inversely proportional to the inertia (see Sec. 2.2.1). Therefore, the inertia about the most polarizable axis should ideally be low compared to the inertia about the other two axes, ensuring relatively large rotational impact around the most polarizable axis while minimizing rotation of the axis itself. In Table 7.1 the moments of inertia about the principal molecular axes are listed for DBT and 3,5-difluoroiodobenzene (DFIB)^b. The orientation of the principal molecular axes can be seen from Fig. 7.2. We see that for DBT the inertia about the most polarizable axis (the *b*-axis) is comparable to the inertia about the *a*-axis. The moments of inertia for DFIB are much more suited. The position of the very heavy iodine atom on the most polarizable axis (the *a*-axis) makes the inertia about this axis much smaller than it is about the other two. The polarizability tensor of DFIB is expected to be very similar to that of iodobenzene and

^aIn planar alignment the molecular plane is confined to a space fixed plane. The molecules are, however, free to rotate about an axis perpendicular to the plane. Strictly speaking, this is in fact 1D alignment of the molecular axis that is perpendicular to the plane of the molecule.

^bThe moments of inertia of DFIB are estimated from a simple geometry optimization.

**3,4-dibromothiophene**

Axis	$I [\text{\AA}^2 u]$	$\alpha_{ii} [\text{\AA}^3]$
<i>a</i>	537	16.0
<i>b</i>	548	20.5
<i>c</i>	1080	10.1

3,5-difluoroiodobenzene

Axis	$I [\text{\AA}^2 u]$	$\alpha_{ii} [\text{\AA}^3]$
<i>a</i>	289	21.5
<i>b</i>	1050	15.3
<i>c</i>	1340	10.2

Figure 7.2: Molecular models including the principal inertia axes. Top: 3,4-dibromothiophene. Bottom: 3,5-difluoroiodobenzene.

Table 7.1: Inertia and polarizability volume for DBT and DFIB. For DFIB the values are only estimates; The inertia is computed from a very simple geometry optimization and the polarizability is estimated to be the same as for iodobenzene.

according to Eq. (7.1) and Eq. (7.2) it is ideal for 3D alignment experiments. As can be seen in the F^+ and I^+ ion images in Sec. 6.2 the Coulomb explosion channels for these ions are confined to narrow radial intervals. For these reasons DFIB is expected to be a good candidate molecule for the combination experiments.

7.2 Experiments on 3,5-difluoroiodobenzene

The combination experiment on DFIB was conducted right after the 3D adiabatic alignment experiments presented in Sec. 6.2. A schematic drawing of the optical setup used for this experiment is presented in Fig. 3.1. The experiment was conducted in the new vacuum system with the Even-Lavie valve. Due to the low inertia about the most polarizable molecular axis (the C-I axis), and consequently a need for only a rather modest fluence to excite rotation, we decided to use the direct output from the femto-second laser (800 nm, 150 fs, $2 \times 10^{13} \text{ W/cm}^2$, $\omega_0 = 50 \mu\text{m}$) as the kick pulse. A detailed analysis of the mass/charge spectrum, the Coulomb explosion probe and the 2D velocity projections for DFIB is given in Sec. 6.2 and will not be further addressed here.

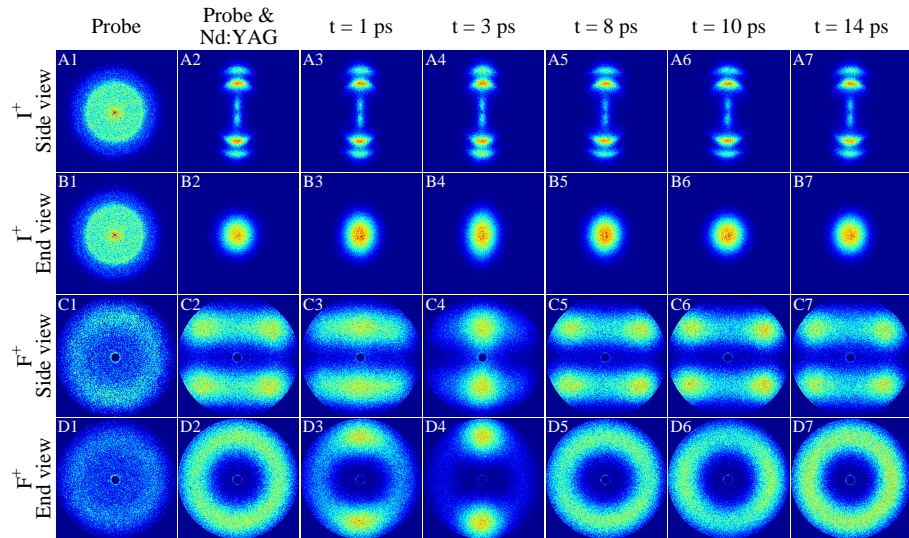


Figure 7.3: Ion images of I^+ and F^+ fragments recorded in both end and side view. Column 1 (Coulomb explosion probe only) and 2 (Coulomb explosion probe and Nd:YAG pulse) serve as reference images. Column 3-7, recorded at different times after the kick pulse, illustrate the alignment dynamics. The intensity of the Nd:YAG and kick pulse are $7 \times 10^{11} \text{ W/cm}^2$ and $2 \times 10^{13} \text{ W/cm}^2$.

7.2.1 Early dynamics

A series of ion images showing 2D ion velocity projections is presented in Fig. 7.3. Images recorded within the first 14 ps following the kick pulse are shown along with reference images for the Coulomb explosion probe (800 nm, 30 fs, $3 \times 10^{14} \text{ W/cm}^2$, $\omega_0 = 30 \mu\text{m}$) alone (column 1) as well as for the Coulomb explosion probe and the Nd:YAG pulse (1064 nm, 10 ns, $7 \times 10^{11} \text{ W/cm}^2$, $\omega_0 = 50 \mu\text{m}$) combined (column 2). Similar to the earlier adiabatic 3D alignment experiments on DFIB (Chapter 6) the Coulomb explosion probe was fixed perpendicular to the plane of the detector for the I^+ ion images and along the polarization of the Nd:YAG pulse for the F^+ ion images. Again both the end view and the side view are presented for both ion species.

As described in Sec. 6.2 strong 1D alignment of the C-I axis of DFIB is obtained from the linearly polarized Nd:YAG pulse. This manifests itself in confinement along the vertical axis in the I^+ side view image (Fig. 7.3 A2) and near the center in the end view image (Fig. 7.3 B2). From the circular shape of the F^+ end view image (Fig. 7.3 D2) it is clear that the molecular plane is not confined in 1D adiabatic alignment. When describing the dynamics following the kick pulse the end view images are best suited, since confinement of the molecular plane and distortions in the confinement of

the C-I axis are readily observed directly from the images. In the I^+ end view images we see that the tightly confined circular distribution in the image without the kick pulse (Fig. 7.3 B2) is changed as the kick pulse is included. After the interaction with the kick pulse an elongated shape towards the kick pulse polarization axis (the vertical axis in the end view images) start to appear. This occurs since perfect 1D adiabatic alignment is not achieved with the Nd:YAG pulse and the interaction between the kick pulse and the most polarizable molecular axis can therefore not be completely avoided. The distribution does, however, quickly return to a circular shape (at $t = 10$ ps) and stays tightly confined hereafter. Note that the distortion of the C-I axis is only minor and that the axis remains tightly confined throughout the experiment. This can be seen both by observing that all I^+ end view images following the kick pulse (Fig. 7.3 B3-B7) are much better confined radially than the image recorded for randomly oriented molecules (Fig. 7.3 B1). In addition, if the C-I axis was strongly misaligned the I^+ side view images would not be as confined as is the case (Fig. 7.3 A3-A7).

Having confirmed good confinement of the C-I axis throughout the experiment our attention turned to the F^+ ions in order to determine the orientation of the molecular plane. In the F^+ end view images (Fig. 7.3 row D) dramatic changes are observed immediately after the kick pulse, where a localization along the vertical axis (kick pulse polarization axis) is forming. At $t = 3$ ps (Fig. 7.3 D4) the localization peaks with two intense spots on the vertical axis and a low background with almost uniform intensity along a circular shape. Just as concluded in Sec. 6.2, this can only be compatible to 3D alignment of the molecules, where the C-I axis is pointing into the detector (along the Nd:YAG polarization) and the molecular plane is confined to the plane spanned by the Nd:YAG and kick pulse polarizations. At longer delays the localization along the vertical axis decrease and a nearly circular distribution is observed at $t = 8$ ps (Fig. 7.3 D5), hence 3D alignment is lost and only 1D alignment is preserved as confirmed by the I^+ images. Shortly hereafter, at $t = 10$ ps, localization in the F^+ end view image along the horizontal axis is observed, indicating alignment of the molecular plane perpendicular to the kick pulse polarization axis. Finally, at $t = 14$ ps the circular symmetry is restored. The evolution from alignment along the kick pulse polarization to perpendicular to the kick pulse polarization is perhaps even more pronounced in the F^+ side view. Here the planar alignment at $t = 3$ ps is seen as two localized areas centered along the vertical axis (Fig. 7.3 C4) as opposed to the double horizontal line like shape (Fig. 7.3 C2) discussed in Sec. 6.2. This is compatible with alignment of the molecular plane perpendicular to the detector plane and the C-I axis in the detector plane, along the vertical axis in the images. As the molecular plane aligns perpendicular to the kick pulse polarization axis it is confined to the detector plane and the F^+ ion velocity distribution shows up as a four-center image (Fig. 7.3 C6). The confinement of the molecular plane to the detector plane illustrate an advantage of the combination method, since this is not possible, in our experimental setup, with the use of a single elliptically polarized Nd:YAG pulse.

From Fig. 7.3 we conclude that a high degree of 3D alignment is obtained 3 ps

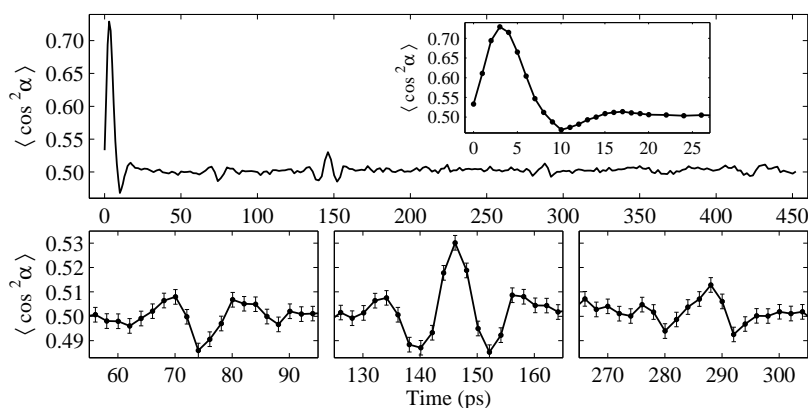


Figure 7.4: Alignment dynamics of the molecular plane, represented by $\langle \cos^2 \alpha \rangle$, as a function of time after the kick pulse. The laser intensities are the same as stated in Sec. 7.2.1. The insert and the three lower subfigures are magnified portions of the long scan.

after the interaction with kick pulse. The alignment quickly vanishes and is replaced by weak 3D alignment with the molecular plane orthogonal to the kick pulse polarization axis. At longer delays the molecular plane is no longer confined and its angular distribution seems to be nearly uniform. At all times, the confinement of the molecular symmetry axis remains high, although, a slight deviation towards the kick pulse polarization axis is observed around the time of the maximal planar confinement.

7.2.2 3D alignment revivals

Having established 3D alignment immediately following the kick pulse we decided to look for 3D alignment revivals. First we confirmed that the C-I axis continued to be confined along the Nd:YAG polarization by recording I^+ end view images at a series of delays following the kick pulse. After the initial distortion no changes were discovered and a distribution resembling the one recorded at $t = 14$ ps was observed at all following delays. Having confirmed that the C-I axis stays nicely confined after the initial distortion a search for changes in the angular distribution of the molecular plane was undertaken. To quantify the degree of alignment of the molecular plane we again use the average value of $\cos^2 \alpha$, where α now is the angle between the polarization of the kick pulse (vertical in the end view images) and the 2D projection of the F^+ ion velocity. A scan of F^+ end view ion images was recorded for the first 450 ps following the kick pulse with a 2 ps step size. For each F^+ ion image $\langle \cos^2 \alpha \rangle$ was determined and the results are shown in Fig. 7.4. The planar alignment peaks at $t = 3$ ps with $\langle \cos^2 \alpha \rangle = 0.73$, and at the point of anti-alignment ($t = 10$ ps) it decreases to 0.47.

Subsequently, $\langle \cos^2 \alpha \rangle$ remains essentially constant at a value of 0.50 except for four transients centered at 74 ps, 146 ps, 217 ps and 288 ps. At the strongest transient located at $t = 146$ ps the planar alignment is restored although with reduced strength ($\langle \cos^2 \alpha \rangle = 0.53$). End view images of I^+ ions, recorded in the time intervals around the revivals, revealed no dynamics and were essentially indistinguishable from those obtained without the kick pulse. The C-I axis of the molecules were thus strongly confined throughout the temporal range presented in Fig. 7.4. Therefore, we conclude that the 3D alignment exhibits revivals, however, with severely reduced planar confinement compared to the initial transient at $t = 3$ ps.

The transients located at 3, 146 and 288 ps have similar shape which suggest a repetition with a separation of ~ 143 ps. In fact, some structure is observed at $t = 432$ ps but a transient similar to the other three cannot be clearly isolated. Unfortunately we were not been able to find the rotational constants of 3,5-difluoriodobenzene in the literature and we therefore decided to conduct 1D nonadiabatic alignment experiments in order to obtain a good estimate of the rotational constants. These experiments, closely resembling rotational coherence spectroscopy (RCS) experiments [35], are discussed in App. C. The rotational constants were found to be: $A = 1740$ MHz, $B = 484$ MHz and $C = 379$ MHz. The periodicity observed in Fig. 7.4 corresponds well with $1/(4A) = 144$ ps, which has the significance of the period for a full rotation of the molecular plane about the a -axis, corresponding to A -type revivals using the terminology of RCS [68]. The positions of the weak transients observed between the major transients (at $t = 74$ ps and $t = 217$ ps) classify them as half revivals.

The combination experiments extends the rotational control presented in Sec. 4.2.2. In total three different types of alignment revivals have been observed for asymmetric top molecules and rotation about both the c -axis and a -axis has been isolated.

7.2.3 Theoretical calculation

To confirm our experimental results quantum mechanical simulations were conducted by Tamar Seideman and Edward Hamilton. Due to computational limitations the simulations were conducted at a reduced rotational temperature of 0.2 K and a reduced intensity of 1.5×10^{11} W/cm² and 5×10^{12} W/cm² for the Nd:YAG and the kick pulse. Alignment similar to that observed experimentally is, however, expected as long as strong 1D alignment is established with the Nd:YAG pulse, and the fluence of the kick pulse is not large enough to severely distort it.

Numerically, 1D alignment of the C-I axis is quantified by $\langle \cos^2 \theta \rangle$ and $\langle \cos^2 \phi \rangle$ [Fig. 7.5 (a) and (b)], where θ is the polar Euler angle between the space-fixed Z-axis (here defined as the axis perpendicular to the laser pulse polarizations, i.e. the laser beam propagation axis) and the molecular C-I axis, and ϕ is the azimuthal angle of rotation of the C-I axis about the space-fixed Z-axis, i.e. in the plane spanned by the two polarization axes. In the coordinate system used here ϕ is shifted by $\pi/2$ compared to the one presented by Zare [27], therefore perfect 1D alignment (which is

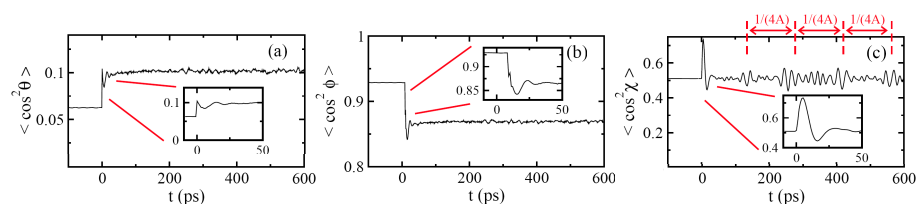


Figure 7.5: Numerical analysis of 3D alignment by a Nd:YAG pulse and a kick pulse. The intensities were 1.5×10^{11} W/cm² and 5×10^{12} W/cm² for the Nd:YAG and the kick pulse respectively, with a kick pulse duration (FWHM) of 150 fs. The rotational temperature was set at 0.2 K. Alignment of the C-I axis to the long pulse polarization direction, quantified by $\langle \cos^2 \theta \rangle$ and $\langle \cos^2 \phi \rangle$, is shown in (a) and (b). Alignment of the molecular plane to the plane spanned by the two polarizations and subsequent revolution about the C-I axis, quantified by $\langle \cos^2 \chi \rangle$, is shown in (c). The insets in panels (a), (b) and (c) magnify the short time dynamics, where the center of the kick pulse defines the origin of time. The arrows in panel (c) point to the periodic interval of $1/(4A)$ between revivals, illustrating rotation of the molecular plane about the C-I axis.

along the space-fixed Y-axis) corresponds to $\langle \cos^2 \phi \rangle = 1$ and $\langle \cos^2 \theta \rangle = 0$.

Prior to the arrival of the kick pulse, $t < 0$, $\langle \cos^2 \theta \rangle = 0.06$ and $\langle \cos^2 \phi \rangle = 0.93$, illustrating sharp 1D alignment of the molecular C-I axis along the Nd:YAG pulse polarization axis. For $t > 0$, $\langle \cos^2 \theta \rangle$ increases to 0.10 and $\langle \cos^2 \phi \rangle$ decreases to 0.87, illustrating a minor distortion of the initial 1D alignment due to the orthogonal kick pulse. This agrees well with the experimental observations in the I⁺ end view and side view images (Fig. 7.3).

Rotation about the C-I axis is rigorously described by $\langle \cos^2 \chi \rangle$, χ being the azimuthal Euler angle of rotation about the molecular z -axis (C-I axis). The numerical results show sharp 3D alignment shortly after the kick pulse with $\langle \cos^2 \chi \rangle = 0.735$ at $t = 5$ ps. The 3D alignment is followed by a series of partial-revivals at a period of about $1/(4A)$, corresponding to periodic reconstruction of the 3D alignment, however, with much reduced amplitude as compared to the initial peak. The numerical results agree with the experimental $\langle \cos^2 \alpha \rangle$ values in Fig. 7.4, illustrating that α makes a good approximation to the angle of rotation about the C-I axis. Note that α and χ are identical in the limit of perfect 1D alignment of the C-I axis along the Nd:YAG pulse polarization axis.

7.2.4 Importance of 1D alignment prior to the kick pulse

As stated previously high confinement of the most polarizable molecular axis is crucial in order to minimize rotation of this axis due to the kick pulse. To illus-

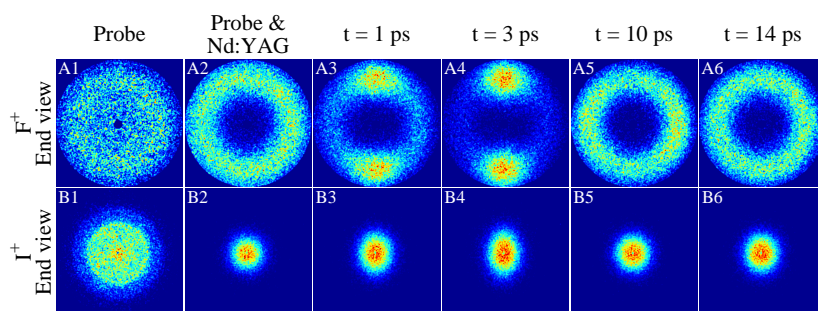


Figure 7.6: End view image series of F^+ and I^+ fragments. This series is recorded under "High" Nd:YAG intensity ($7 \times 10^{11} \text{ W/cm}^2$). The first column with the Coulomb explosion probe only is included for reference.

trate this the dynamics following the kick pulse was investigated with two different Nd:YAG pulse intensities. A set of ion images with a high degree of 1D alignment ($I_{\text{Nd:YAG}} = 7 \times 10^{11} \text{ W/cm}^2$, $\langle \cos^2 \theta_{2D} \rangle = 0.928$) and one with a weaker 1D alignment ($I_{\text{Nd:YAG}} = 1.4 \times 10^{11} \text{ W/cm}^2$, $\langle \cos^2 \theta_{2D} \rangle = 0.862$) was recorded. No changes were made for the kick and Coulomb explosion pulse. Note that the degree of alignment in the second set is quite high compared to what is obtained in nonadiabatic alignment, however, significantly lower than what is observed at high Nd:YAG intensity. In Fig. 7.6 the image series recorded at high Nd:YAG intensity is shown. Since the conditions are almost the same as in Sec. 7.2.1 we observe the same dynamics, where high confinement of the molecular plane is obtained while the C-I axis is relatively undisturbed.

As we reduce the intensity of the Nd:YAG pulse, the F^+ end view images look quite similar and the alignment dynamics seem to follow the same pace as at high intensity. The reduced radial confinement of the doughnut structure in the F^+ images (Fig. 7.7 A1-A6 compared to Fig. 7.6 A2-A6) does, however, show that the C-I axis is less confined. The I^+ end view images confirm this observation. From the 1D aligned images (Fig. 7.6 B2 and Fig. 7.7 B1) lower confinement of the C-I axis is clearly seen as an increased size of the I^+ ion distribution at the lower intensity. Following the kick pulse a severe impact in the confinement of the C-I axis is observed in the I^+ end view images at the low Nd:YAG intensity (Fig. 7.7 B2-B5). Since the kick pulse parameters are unchanged the increased distortion can only result from lower initial confinement of the C-I axis. When comparing the most distorted ion images (Fig. 7.7 B3-B5) to the image recorded on the isotropically distributed sample (Fig. 7.6 B1) the confinement of the C-I axis along the Nd:YAG polarization axis seems to have been almost lost. To obtain more insight into this an I^+ side view image series was recorded (Fig. 7.7 C row). The significantly lower initial 1D alignment ($\langle \cos^2 \theta_{2D} \rangle = 0.862$) is apparent in the first image (Fig. 7.7 C1). Following the kick pulse the severe distortion observed

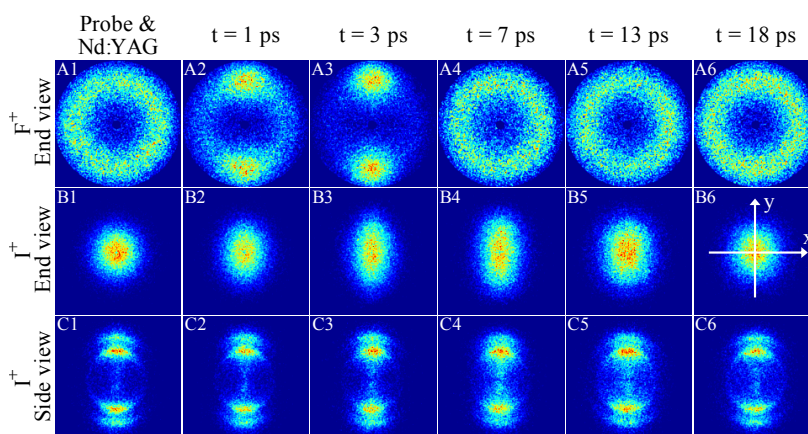


Figure 7.7: End view images of F^+ fragments and both end and side view images of I^+ fragments. This series is recorded under "Low" Nd:YAG intensity ($1.4 \times 10^{11} \text{ W/cm}^2$). The x and y-axis shown in B6 bisect the image center and are used to quantify the degree of alignment (see text).

in the end view images is confirmed, however, no C-I axis alignment along the kick pulse polarization axis is observed as the ion signal near the center is still very low.

Quantitative measures for the degree of alignment from both the high and the low Nd:YAG intensities have been determined and are presented in Fig. 7.8. The bottom graph shows the confinement of the molecular plane. Only small changes are observed as the intensity of the Nd:YAG pulse is changed, the position of the initial alignment peak and the revival is unchanged and the degree of alignment is very similar for the two curves. Moving to the confinement of the C-I axis we do however observe large differences. The top graph in Fig. 7.8 depicts the average pixel distance, from the center of the image to the ion hits, along the y-axis and x-axis (see axis on Fig. 7.7 B6 and explanation in Sec. 6.2). If the kick pulse is not added the average distance to the center at the high Nd:YAG intensity is around 44 pixels for both directions whereas for the low Nd:YAG intensity it is 61 and 58 pixels along the vertical (y) and horizontal (x) axis respectively (values extracted from Fig. 7.6 B2 and Fig. 7.7 B1). The asymmetry in the low intensity case is due to a slightly elliptical Nd:YAG polarization, originating from the finite extinction ratio in the thin film polarizer that is used to control the Nd:YAG intensity. The increased average distance at the low Nd:YAG intensity, results from lower confinement of the C-I axis as seen in Fig. 7.7. Following the kick pulse the average distances remain relatively well controlled at high Nd:YAG intensity, with a maximum increase of 10 pixels along y at $t = 4 \text{ ps}$. For the low intensity case the impact is significantly higher, peaking along y at $t = 7 \text{ ps}$

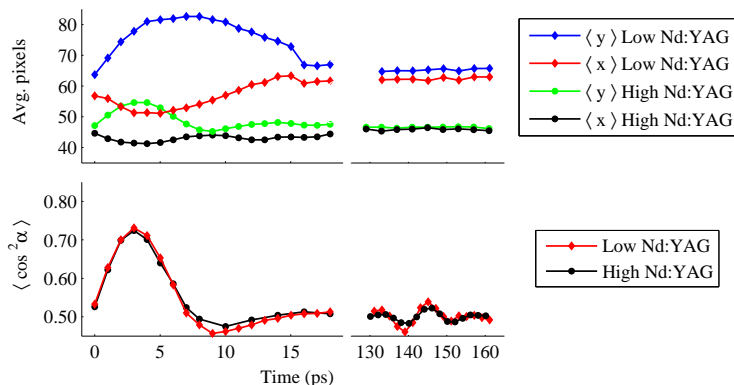


Figure 7.8: Top: Average distance to center along vertical axis (y) and horizontal axis (x) for each ion hit in the I^+ end view images. Bottom: $\langle \cos^2 \alpha \rangle$ calculated from F^+ end view images. The intensity of the kick pulse is fixed at 2×10^{13} W/cm², the Nd:YAG intensity is 7×10^{11} W/cm² in the "High Nd:YAG" series (black and green curves, circles) and 1.4×10^{11} W/cm² in the "Low Nd:YAG" series (red and blue curves, diamonds).

with an increase of 22 pixels. This shows that the interaction between the kick pulse and the C-I axis is not negligible. In fact at $t = 7$ ps the average distance along y is 1 pixel higher than for the unaligned case (Coulomb explosion probe only, Fig. 7.6 B1). Direct comparison can, however, not be made since the Coulomb explosion probe possess angular selectivity and the angular distributions are very different for the two images. For both the high and the low Nd:YAG intensity a decrease in the average distance is observed along the x axis.

As stated earlier no structure is seen in the I^+ end view at long delays, which is clearly seen in the depicted interval around the revival at $t = 146$ ps. Here the average distances are constantly 3 to 4 pixels higher than the value recorded in the absence of the kick pulse.

From Fig. 7.6, Fig. 7.7 and Fig. 7.8 we conclude that high confinement of the most polarizable molecular axis, prior to the kick pulse, is essential for obtaining a high degree of 3D alignment. At lower initial confinement of the most polarizable molecular axis 3D alignment can still be obtained, however, at a considerable cost in the confinement of the most polarizable molecular axis.

7.2.5 Kick pulse alignment dependency

Next we decided to reduce the intensity of the kick pulse to see how it would affect the alignment. The intensity of the Nd:YAG pulse was fixed at 7×10^{11} W/cm² (corresponding to "High Nd:YAG" in Sec. 7.2.4) and the kick pulse was reduced to half the intensity (1×10^{13} W/cm²). For comparison a series was also recorded at the full kick intensity. The average pixel distances to the center and $\langle \cos^2 \alpha \rangle$ is presented in Fig. 7.9. Without the kick pulse the values were: $\langle y \rangle = 50$ pixels, $\langle x \rangle = 47$ pixels and $\langle \cos^2 \alpha \rangle = 0.512$. The asymmetric average pixel distances and the elevated $\langle \cos^2 \alpha \rangle$ value result from slight misalignment of the polarization controlling wave plates. The Nd:YAG pulse was therefore not perfectly linear but rather slightly elliptically polarized. The recorded ion images are not shown here. From Fig. 7.9 we see that the impact on the alignment of the C-I axis is only slightly reduced when the kick pulse intensity is lowered by a factor of two. For both intensities the asymmetry peaks a $t = 4$ ps with an average pixel distance along y at 57 and 59 pixels for the low and high kick power respectively. At the low kick intensity a slightly slower evolution in the confinement of the molecular plane is observed from the F⁺ end view images, however, the trace looks quite similar to what is observed at the high kick intensity. Since the alignment of the molecular plane hardly improves as the kick intensity is doubled a saturation in the degree of alignment must have been reached [32]. From these results we conclude that at very high confinement of the most polarizable molecular axis the 3D alignment is less prone to distortions due to the kick pulse.

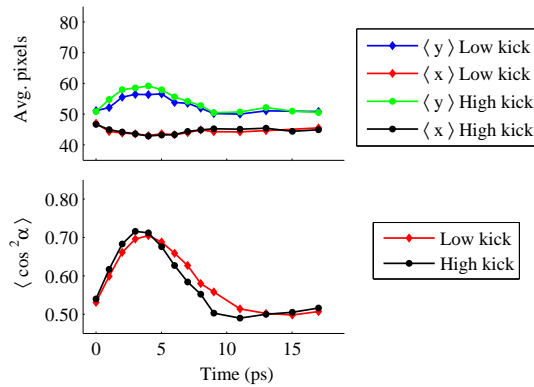


Figure 7.9: Top: Average distance to center along vertical axis (y) and horizontal axis (x) for each ion hit in the I⁺ end view images. Bottom: $\langle \cos^2 \alpha \rangle$ calculated from F⁺ end view images. The intensity of the Nd:YAG was fixed at 7×10^{11} W/cm² while the intensity of the kick pulse was 2×10^{13} W/cm² in the "High kick" series (black and green curves, circles) and 1×10^{13} W/cm² in the "Low kick" series (red and blue curves, diamonds)

7.2.6 Elliptically polarized Nd:YAG pulse

We know from our experiments on two-pulse 1D nonadiabatic alignment (Chapter 5) and from experiments by Poulsen *et al.* [69] that very high degrees of alignment can be obtained if the molecules are weakly aligned prior to the interaction with the kick pulse. Further we have seen (Sec. 6.2) that relatively good planar confinement can be obtained, without too much loss in confinement of the most polarizable axis, when an elliptically polarized Nd:YAG pulse with a 3:1 intensity ratio is used. With this in mind it would be interesting to combine an elliptically polarized Nd:YAG pulse with the kick pulse in order to obtain improved 3D alignment. A series of I^+ and F^+ end view images were recorded, on a sample prealigned with an elliptically polarized Nd:YAG pulse, following the interaction with a kick pulse. The intensity of the kick pulse was $2 \times 10^{13} \text{ W/cm}^2$ and the Nd:YAG pulse intensity was $5.2 \times 10^{11} \text{ W/cm}^2$ along the major polarization axis and $1.7 \times 10^{11} \text{ W/cm}^2$ along the minor axis (3:1 ratio). The calculated measures of the degree of alignment are presented in Fig. 7.10. Most noticeable is the very high degree of confinement of the molecular plane peaking at $\langle \cos^2 \alpha \rangle = 0.849$ at $t = 2$ ps. At the same time the C-I axis is still relatively well confined to the major axis of the Nd:YAG polarization. The distortion of the C-I axis peaks around $t = 4$ ps with a total increase of 10 pixels along the vertical (y) axis. The images recorded at $t = 2$ ps can be seen in the fourth column of Fig. 7.11.

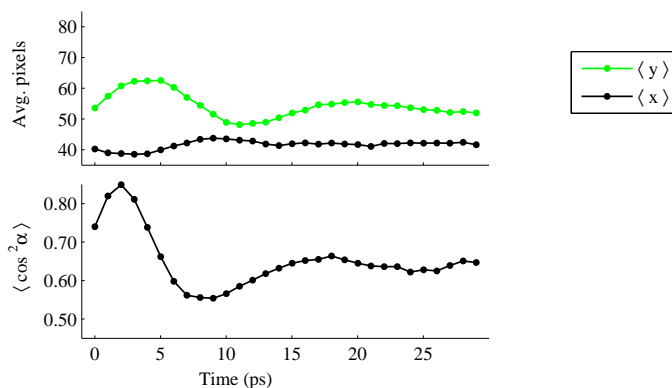


Figure 7.10: Top: Average distance to center along vertical axis (y) and horizontal axis (x) for each ion hit in the I^+ end view images. Bottom: $\langle \cos^2 \alpha \rangle$ calculated from F^+ end view images. The intensity of the Nd:YAG was $5.2 \times 10^{11} \text{ W/cm}^2$ along the major polarization axis and $1.7 \times 10^{11} \text{ W/cm}^2$ along the minor axis while the intensity of the kick pulse was $2 \times 10^{13} \text{ W/cm}^2$.

7.2.7 3D alignment comparison

During the last two chapters many different pulse parameters and schemes have been used in order to align DFIB molecules three dimensionally in space. To sum up our findings and to evaluate the alignment achieved I have collected the images and alignment data from the most optimum conditions in Fig. 7.11. Throughout these images the total intensity of the Nd:YAG pulse is kept fixed at 7×10^{11} W/cm². The kick pulse intensity is also identical in the two combination experiments shown in the third and fourth column (2×10^{13} W/cm²).

From the quantitative numbers in Fig. 7.11 the alignment achieved in the 3:1 adiabatic experiment and the combination experiment look almost identical, however, as can be seen from the graphs in the third row of Fig. 7.11 (C1 and C3), the angular distributions of the molecular planes are quite different. In the combination experiment (C3) a narrow distribution is obtained near $\alpha = 0, \pi$, however, some signal is observed at angles far from 0 and π . This means that alignment of the molecular plane is not obtained for a non negligible fraction of the molecules. This angular distribution is expected since we know that the interaction with the kick pulse is weak at large angles (near $\pi/2, 3\pi/2$). For this reason molecules with their molecular plane initially located at angles close to $\alpha = \pi/2, 3\pi/2$ (horizontal axis in the end view images) will not align shortly after the pulse and instead contribute to the signal at large angles. For the purely adiabatic case (C1) a wider distribution around $\alpha = 0, \pi$ is observed and much less signal is seen at large angles.

When the elliptically polarized Nd:YAG pulse (3:1 ratio) is combined with the kick pulse (fourth column in Fig. 7.11) the weakness in the interaction with the kick pulse is overcome by prealigning the molecular plane to angles near $\alpha = 0, \pi$. From the angular distribution (C4) it is clear that the signal near $\pi/2$ is almost completely depleted and an improved angular confinement along the vertical axis is obtained. When comparing the I⁺ end view image we see that the increased confinement of the molecular plane comes at a cost in confinement of the C-I axis.

From Fig. 7.11 we see that good 3D alignment can be obtained using adiabatic alignment techniques. As the nonadiabatic kick pulse is added, significant improvements can be made to the alignment, however, at a cost in confinement of the most polarizable molecular axis and with some additional complexity in the experiment.

In experiments where 3D aligned molecules are needed under field-free conditions our combination method has to be extended by rapid truncation of the Nd:YAG pulse [70] upon establishment of the 3D alignment. This truncation can be conducted on a timescale of about 100 fs, fast enough to avoid considerable reductions in the 3D alignment. The experiments by Lee *et al.* [65] relied on two linearly polarized kick pulses to obtain 3D alignment of SO₂ molecules under field-free conditions. The first kick pulse would align the molecular O-O axis (termed O-axis) along its polarization axis (space X-axis) and the second pulse, polarized perpendicular to the first, would align

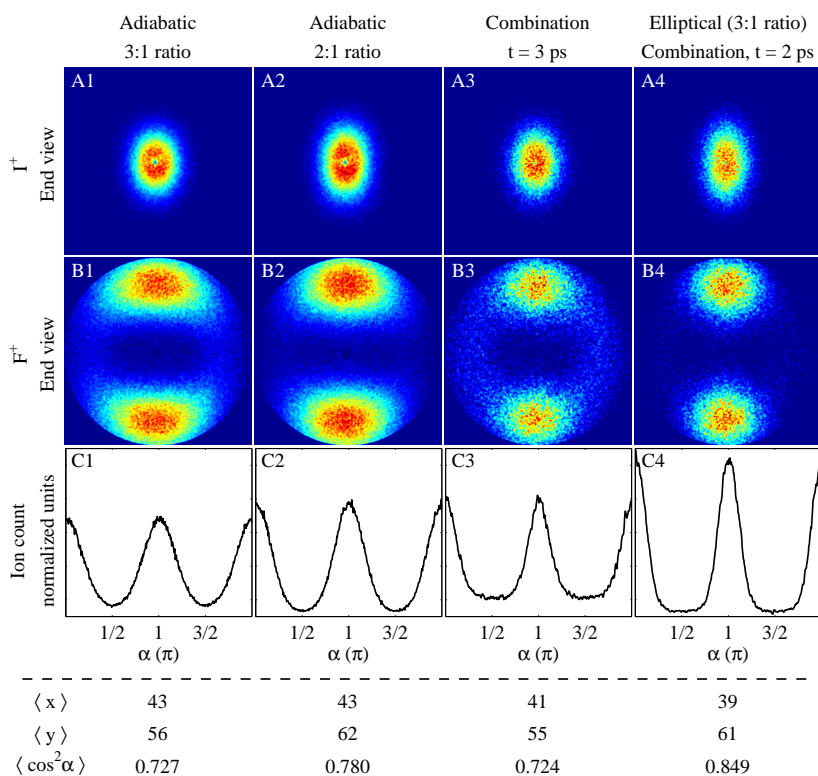


Figure 7.11: I^+ and F^+ end view images for different pulse parameters and schemes. The third row shows the angular distribution of F^+ ions in the region used to calculate $\langle \cos^2 \alpha \rangle$. The total intensity of the Nd:YAG pulse is the same for all four columns ($7 \times 10^{11} \text{ W/cm}^2$) and in the third and fourth column the kick pulse intensity is $2 \times 10^{13} \text{ W/cm}^2$.

the molecular C_2 -symmetry axis (termed S-axis) along its polarization axis (space Y-axis). To quantify the degree of alignment they measured the angle between the Y-axis and the S-axis in the Y,Z plane, θ_S , and the angle between the X-axis and the O-axis in the X,Y plane, θ_O , for each molecule. From these angles they calculated $\langle \cos^2 \theta_S \rangle$ and $\langle \cos^2 \theta_O \rangle$ as measures of the degree of alignment. These measures are quite similar to $\langle \cos^2 \alpha \rangle$, having a value of 0.5 for a random distribution and 1 for a perfectly aligned distribution (α is also a projection of an axis onto a plane). Their best 3D alignment peaked with values of $\langle \cos^2 \theta_S \rangle \sim \langle \cos^2 \theta_O \rangle \sim 0.58$. Due to a different detection method and a different sample molecule, direct comparison between these and our results cannot be made, however, it is clear that their obtained alignment is

much lower than what we observe. The limiting factor in the dual kick approach is the weak alignment of the most polarizable molecular axis (O-axis) obtainable with the initial kick pulse. Based on our experiences with weaker confinement of the C-I axis prior to the kick pulse (Sec. 7.2.4, $\langle \cos^2 \theta_{2D} \rangle = 0.862$), I believe that our approach to 3D alignment is superior to the dual kick pulse method applied by Lee *et al.*, even when reduced confinement during truncation of the Nd:YAG pulse is considered. The 1D alignment obtained after a kick pulse is simply too weak, and high distortion in the alignment of the most polarizable molecular axis by the second pulse is unavoidable.

CHAPTER 8

Perspectives

The combination of adiabatic and nonadiabatic alignment techniques described in Chapter 7 enables a high degree of 3D alignment and gives control over new rotations. Also the use of two different ion velocity projections opens up for new insight in the molecular angular distributions. As the next step in rotational control we would like to use these tools to address internal rotations of molecules.

Biphenyl [$C_{12}H_{10}$] is a good candidate molecule for such an experiment, since we already have experimental experience with this type of molecule and since it consists of two rigid phenyl rings connected by a single C-C bond. It would be interesting to record the dihedral angle (the twist angle between the planes of the two phenyl rings) for this molecule and see if we are able to change it by inducing rotation of one phenyl plane with respect to the other, i.e. induce internal rotation. Biphenyl is known to have a dihedral angle, ϕ_d , of about 42° and rotational barriers of about 2 kcal/mol^a at $\phi_d = 0^\circ$ (parallel phenyl planes) and about 1.5 kcal/mol at $\phi_d = 90^\circ$ (perpendicular phenyl planes) [71]. Substitution of the hydrogens in the ortho position (next to the bond connecting the two phenyls) is known to increase the dihedral angle and raise the rotational barrier substantially whereas para and meta substitution hardly change these properties [71].

In this chapter I will present the first experimental results aimed at causing internal rotation of a substituted biphenyl due to laser induced torques. This can be seen as an extension of all previous works on laser induced alignment where only the axes of rigid molecule was controlled with respect to space-fixed axes. Although not achieved

^a1 kcal/mol is 0.0434 eV.

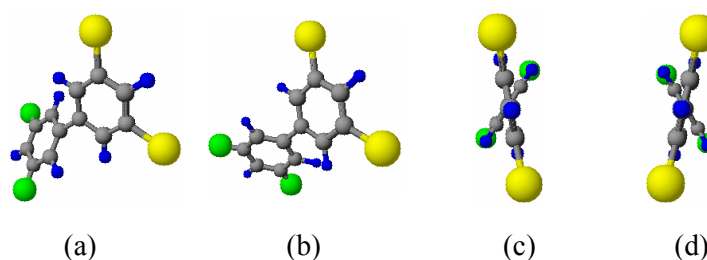


Figure 8.1: Molecular model of 3,5-difluoro-3',5'-dibromobiphenyl. The bromine and fluorine atoms are indicated as yellow and green, respectively. (a) and (b) depicts the two different enantiomers and they are shown from the bromine phenyl end in (c) and (d).

yet our preliminary results point to the possibility for overcoming rotational barriers of molecules by short laser pulses and thus for control of molecular conformations.

We can not learn much from work on unsubstituted biphenyl since markers for velocity map imaging are required in our experimental setup. In analogy to DFIB substitution in the meta positions is desirable, since it would enable detection of the orientation of the molecular planes through velocity map imaging. We decided to do preliminary experiments on 3,5-difluoro-3',5'-dibromobiphenyl^b (DFDBrBP), where the two fluorines identify the orientation of one phenyl ring plane (the F-plane) and the two bromines the orientation of the other (the Br-plane). Molecular models of DFDBrBP are shown in Fig. 8.1. When comparing Fig. 8.1 (a) and (b) it is apparent that this molecule is chiral. There is no way that the molecule in (a) can be rotated so that it completely overlap with the one in (b). This may be easier to see from Fig. 8.1 (c) and (d), where the molecule is viewed from the bromine phenyl end. The two different enantiomers are identified by opposite dihedral angles.

Laser induced alignment will always be obtained in accordance with the polarizability tensor. For DFDBrBP with a dihedral angle of 42° the polarizabilities are^c: $\alpha_{xx} = 30.5 \text{ \AA}^3$, $\alpha_{yy} = 15.9 \text{ \AA}^3$, $\alpha_{zz} = 37.8 \text{ \AA}^3$, where the z -axis is along the C-C bond connecting the two phenyls, the x -axis bisects the small angle between the two phenyl planes at an angle of $\theta_{\text{Br}-x} = 11^\circ$ from the Br-plane. The y -axis is naturally perpendicular to the other two. Due to the high polarizabilities the interaction with the laser field will be strong, however, the 1D confinement in the Nd:YAG field will most likely not be as high as observed for iodobenzene or 4,4'-dibromobiphenyl in Sec. 6.1 since the polarizability tensor of DFDBrBP is less asymmetric (see Eq. (7.1)). As the axis

^bThis molecule is not commercially available and was synthesized by Thomas Poulsen from the Department of Chemistry, University of Aarhus.

^cCalculation by Mikael Johansson from the Department of Chemistry, University of Aarhus, private communication.

of second highest polarizability is not coinciding with any of the two phenyl planes, 3D alignment of this molecule will be less ordered than what we have observed for planar molecules. At perfect 3D alignment the z -axis will align along the Nd:YAG polarization axis and x -axis along the kick pulse polarization axis, this means that the Br-plane will be confined to angles of $\theta_{\text{Br}-x} = 11^\circ$ to *either* side of the kick pulse polarization axis and similarly the F-plane to angles of $\theta_{\text{F}-x} = \theta_d - \theta_{\text{Br}-x} = 31^\circ$ to *either* side of the kick pulse polarization axis. End view ion images of both Br^+ and F^+ are thus expected to have four ion impact regions. However, due to a finite degree of alignment and the low angle between the Br-plane and the axis of second highest polarizability we do not expect to be able to resolve the four regions in the Br^+ ion images.

Ion images from preliminary experiments on DFDBrDP are shown in Fig. 8.2. Each column contains end view F^+ and end view Br^+ ion images recorded both with (at $t = 2.6$ ps) and without the kick pulse. In the left column (1) the Nd:YAG polarization is linear and in the next two it is elliptical with an intensity ratio of 9:1 (2) and 3:1 (3), respectively. The intensities were 1×10^{12} W/cm², 5×10^{12} W/cm² and 4×10^{14} W/cm² for the Nd:YAG pulse (10 ns), the kick pulse (0.7 ps) and the Coulomb explosion pulse (30 fs), respectively. As expected the doughnut shaped ion distribution previously observed for the F^+ ions in 3,5-difluoriodobenzene (see Fig. 6.5) is reproduced in the F^+ ion images from DFDBrBP (Fig. 8.2 C1), however, the Br^+ ion images (A and B row) look completely different. This can be attributed to less confined Coulomb explosion channels for the Br^+ ions. When comparing with the results from adiabatic alignment presented in Sec. 6.1 we saw the same effect in the Br^+ ion images from 4,4'-dibromobiphenyl. In all ion images the center has been cut out due to a very high ion count. In the F^+ ion images this partly consists of thermal H_2O^+ originating from chamber background and is therefore not well confined to the center. The blind spot just "North West" of the ion distribution center (visible in the Br^+ ion images), is the center of the detector which due to prolonged use has become nonresponsive. For unknown reasons the whole ion distribution moved during the recording of these data and was therefore not centered on the detector. From the F^+ images, which fill up most of the detector area, it is clearly seen that the ion distribution is not centered on the detector. Ion angular distributions extracted from the above images are shown in the two bottom rows. The blue curves represents the distribution when only the Nd:YAG pulse is used and the red curves represents the distribution when the kick pulse is included. For Br^+ the values are extracted from the radial range corresponding to the droplet like shape in the ion images (most pronounced in B2 and B3), the centermost part of the ion distribution is not included. For F^+ the radial range corresponding to the doughnut like shape of Fig. 8.2 C1 is used.

For the case of adiabatic alignment (row A and C) a confinement of both the Br^+ and F^+ ions is observed along the vertical axis of the images as the the field from the Nd:YAG pulse becomes elliptically polarized (the vertical axis is coinciding with the minor polarization axis of the Nd:YAG pulse). The Br^+ ions are clearly more confined

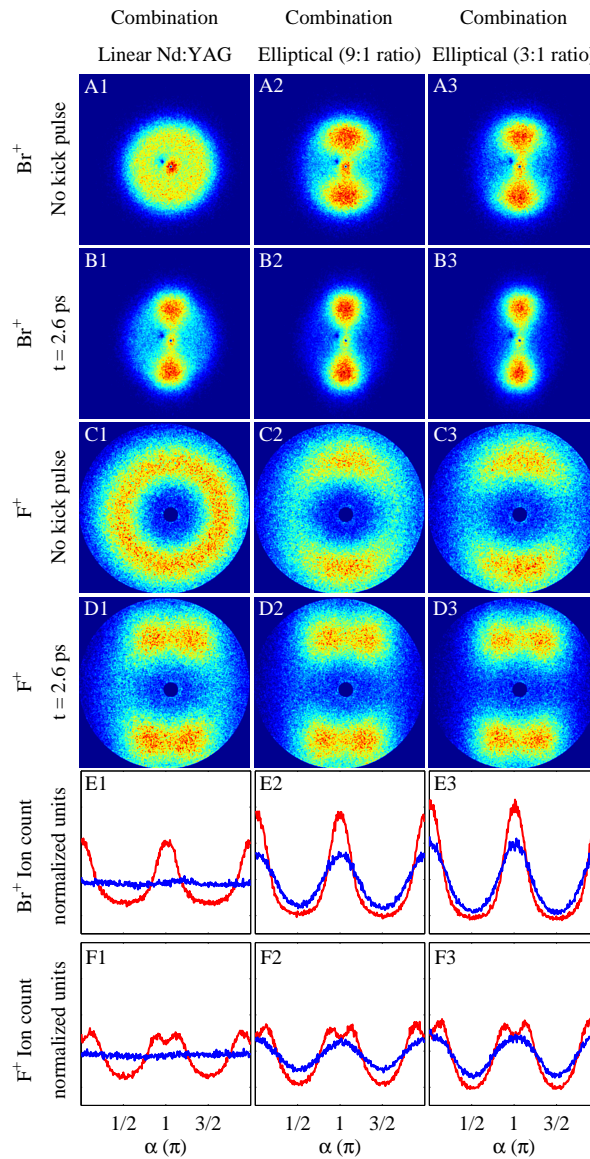


Figure 8.2: End view ion images of Br^+ ions (row A and B) and F^+ ions (row C and D) with (B and D) and without (A and C) the kick pulse. For the images in the first column the Nd:YAG pulse is linearly polarized. In the following two columns it is elliptically polarized with an intensity ratio of 9:1 and 3:1 respectively. The curves in the graphs (row E and F) represents the ion angular distributions extracted from the above images (see text).

than the F^+ ions in good agreement with the axis of second highest polarizability being closest to the Br-plane ($\theta_{Br-x} < \theta_{F-x}$). Contrary to our expectations, the four ion impact regions are not observed in the F^+ ion images as the molecule is 3D aligned in the elliptically polarized Nd:YAG laser field.

When the kick pulse is included we observe rotation about the molecular z -axis. The images shown are recorded 2.6 ps after the center of the kick pulse (row B and D) near the time where the confinement of the Br^+ ions peak. Both directly from the Br^+ ion images (row B) and from the angular distributions (red curves in row E) it is clear that a significant improvement in the Br^+ ion confinement is obtained by the combination technique. As expected, particular high confinement of the Br^+ ions along the polarization axis of the kick pulse (vertical axis in the images) is observed when the Nd:YAG pulse is elliptically polarized (image B2 and B3). For all three Nd:YAG polarizations we observe a splitting in the F^+ ion signal (row D) when the kick pulse is included. The four different ion impact regions are resolved in these images and are clearly visible in the F^+ ion angular distributions (row F) as a splitting of the peaks near $\alpha = 0, \pi$. The splitting between the F^+ ion impact regions is observed to be small and hence very good alignment of the axis of second highest polarizability must be obtained in order to resolve it. I suspect that this splitting is not observed for the adiabatic case due to low angular confinement of the axis of second highest polarizability. Additionally, the difference between the alignment characteristics of adiabatic alignment and the combination technique may also play an important role. As discussed in Sec. 7.2.7 the angular distribution near the alignment axis tends to be more narrow for the combination technique than for adiabatic alignment. The wider distribution near the alignment axis for adiabatic alignment prevents the resolving of the four F^+ ion impact regions. In contrast, the weakness of the combination technique (with linear Nd:YAG polarization), where a relatively high amount of molecules are located at large angles with respect to the kick pulse polarization, is less important here since this adds a background over the whole 2π circle and therefore only results in minimal blurring of the structure near the alignment axis. When comparing the Br^+ ion angular distributions (row E) from the adiabatic alignment (blue curve) and the combination experiment (red curve) it is apparent that the distributions are narrower for the combination experiments.

To find an estimate for the angular splitting in the F^+ ion images a curve fitting was conducted. From studies on the DFIB results presented in Chapter 7, we found that the angular distributions of the F^+ ions have almost perfect gaussian shapes (sum of two gaussian functions centered at $\alpha = 0, \pi$). Therefore, a sum of four gaussians was fitted to the red curves of Fig. 8.2 F1, F2 and F3. In Fig. 8.3 the best fit for the 9:1 intensity ratio is shown (black curve) together with the measured distribution (red curve). The centers of the gaussians are: 26.3° , 157.2° , 205.6° and 338.0° corresponding to an

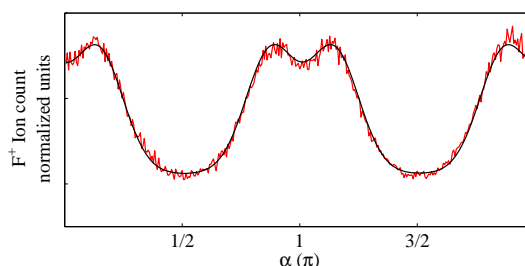


Figure 8.3: F^+ ion angular distribution (red curve) from the combination experiment with an elliptically polarized Nd:YAG pulse (9:1 intensity ratio). The black curve is the sum of the four Gaussians fitted to the experimental curve.

angle of:

$$\theta_{F-x} = \frac{(205.6^\circ - 157.2^\circ)/2 + (26.3^\circ + 360^\circ - 338.0^\circ)/2}{2} = 24.2^\circ \quad (8.1)$$

From the linear and the 3:1 Nd:YAG polarization cases the angle was found to be 23.7° and 24.4° respectively. Although these angles indicate a trend for increasing angle with decreasing eccentricity, the uncertainty in these estimates is larger than the difference in the angles. From additional experiments (not presented here) with a linearly polarized Nd:YAG pulse at lower intensities it was found that the angle increases as the intensity of the Nd:YAG increases. At the lowest Nd:YAG pulse intensity ($4 \times 10^{11} \text{ W/cm}^2$) the angle was found to be only 21.5° .

As stated above we expected to observe an angle of $\theta_{F-x} = 31^\circ$ in the F^+ ion images. Our measured angles are clearly smaller indicating a reduced dihedral angle. Whether this is due to laser induced internal rotation we can not conclude from these experimental data alone, but with the help of numerical simulations we hope to get more insight into this. In analogy to the experiments presented in Chapter 5 two or more kick pulses could be used to enhance the rotational excitation. Such an experiment may reveal an even lower θ_{F-x} angle and thus strongly indicate that internal rotations are indeed excited by the kick pulse.

For future experiments it would be interesting to work on a molecule with a lower rotational barrier. A possible candidate molecule is diphenylacetylene which consists of two phenyls connected via a pair of triple bonded carbon atoms. The increased distance between the phenyls significantly reduce the steric hindrance between the meta components on the phenyls. Due to a favorable π -orbital overlap and the low steric hindrance the molecule is planar in the ground state with a rotational barrier of 0.86 kcal/mol at a dihedral angle of 90° [72]. This molecule is one of the smallest conjugated oligomers, which are particularly interesting due to their electric conductivity properties. In the planar geometry the conductivity of diphenylacetylene is rela-

tively high, however, it drops considerably as the molecule is twisted ($\theta_d \neq 0^\circ$) [72]. For this reason conjugated oligomers have been suggested as possible components in molecular scale electronics as molecular wires [73] and switches [74]. Our laser based methods could potentially be used to induce internal rotations in such systems. This could be advantageous since the induced rotations are very fast (timescale of a few picoseconds) and thus fast switching is possible.

CHAPTER 9

Summary

Most bimolecular and photochemical reactions are influenced by molecular orientation. For experiments on gas phase molecules, who are normally randomly oriented, averaging over all orientations will severely reduce the amount of information that can be extracted. This averaging can be avoided if the molecules are brought into alignment with the laboratory-fixed frame, i.e. the molecular axis are confined to space-fixed axis. In this thesis the use of lasers to control molecular orientation have been investigated and the ability to induce rotation of asymmetric top molecules around different molecular axes has been demonstrated.

Laser induced alignment is a general applicable tool since it only requires an anisotropic polarizability. Through interaction with short laser pulses high angular confinement of molecular axis to space-fixed axis can be achieved, however, orientation ("head" versus "tail" order) can in general not be obtained.

The duration of the alignment laser pulse determines the evolution of the alignment process. When the laser pulse is short compared to the rotational period of the molecule, the molecule will get a rotational kick and rotate into alignment along the laser pulse polarization axis. Alignment is usually obtained after the laser pulse turn off under field free conditions. The alignment will be brief as the molecule will keep rotating under the field-free conditions. The achieved alignment can be improved by increasing the fluence (intensity times duration) of the alignment laser pulse or by reducing the rotational temperature of the molecule. If alignment under field-free conditions is desired the pulse must be short enough that the laser field is gone when the the alignment peaks. The intensity is limited by the onset of multiphoton ionization

of the molecules. Often the degree of alignment is, however, limited by saturation at intensities lower than the multiphoton ionization level.

As molecular rotational energy is quantized recurrences in alignment are expected since the components of the laser induced wave packet will rephase. For symmetric top molecules the alignment revivals are separated by a rotational period and the degree of alignment is reproduced at the revivals. For asymmetric top molecules the alignment on the revivals is reduced since only parts of the wave packet rephase. Two different types of revivals are found and control over their relative strength was demonstrated experimentally, by varying the fluence of the alignment pulse. Revivals similar to the ones observed for symmetric top molecules were dominant at low fluence. As the fluence was increased a different kind of revival, unique to asymmetric top molecules, began to dominate. The periodicity of this revival indicates pure rotation about the molecular *c*-axis.

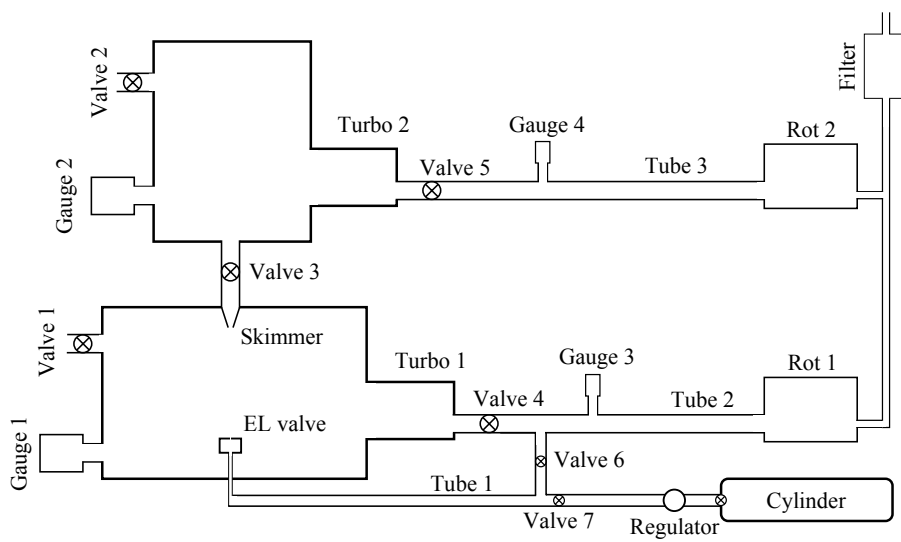
As a way to improve the field-free alignment it has been proposed to use several short alignment pulses. Experimentally we have shown that the best degree of alignment obtainable with a single alignment pulse, limited by saturation and onset of multiphoton ionization, can be significantly improved by using two laser pulses with appropriate duration, relative intensity and timing. This was confirmed for both a symmetric top and an asymmetric top molecule.

If laser pulses that are long compared to molecular rotation are used to align molecules, then the alignment will be obtained only during the laser pulse. This type of laser induced alignment depends critically on the rotational temperature of the molecule, being most effective at low rotational temperature. The degree of alignment can be very high, exceeding that obtainable with short pulses by far, however, the alignment is obtained during the presence of the laser pulse and thus not under field-free conditions. For many applications of alignment the presence of the laser field is not desired as it perturbs the molecules.

A new approach to obtain 3D alignment and to access new rotations has been presented in this thesis. It combines the best properties of alignment by long and short laser pulses: The exceptional 1D alignment obtainable only with long pulses and the ability to induce rotations with short pulses. The long pulse is used to tightly align the most polarizable molecular axis and the short pulse induces rotation about the aligned axis. We have shown that very good 3D alignment can be obtained shortly after the interaction with the short pulse. Periodic 3D alignment revivals were observed and their time separation corresponded well with rotations around the most polarizable molecular axis.

APPENDIX A

Schematic drawing of the new vacuum system



Abbreviations:

Item	Description
Cylinder	200 Bar helium cylinder
EL valve	Even-Lavie valve
Filter	Oil mist filter, EMF20, BOC Edwards
Gauge 1	Compact FullRange BA Gauge PBR 260, Pfeiffer Vacuum
Gauge 2	Compact FullRange BA Gauge PBR 260, Pfeiffer Vacuum
Gauge 3	Compact Pirani TPR 265, Pfeiffer Vacuum
Gauge 4	Compact Pirani TPR 265, Pfeiffer Vacuum
Regulator	0-100 Bar regulator, AIR LIQUIDE
Rot 1	Rotary vane pump, E2M28, BOC Edwards, 32 m ³ /h
Rot 2	Rotary vane pump, DUO 012A, Pfeiffer Vacuum, 12 m ³ /h
Skimmer	Molecular beam skimmer, Ø3 mm orifice, Beam Dynamics Inc.
Tube 1	1/4" stainless steel tube
Tube 2	5 m Ø50 mm copper tube and 2 × 0.5 m Ø50 mm bellows
Tube 3	5 m Ø40 mm copper tube and 2 × 0.5 m Ø40 mm bellows
Turbo 1	Turbovac 361, Leybold, 400 l/s
Turbo 2	CompactTurbo TMU 521P with TC600 drive, Pfeiffer Vacuum, 500 l/s
Valve 1	Manual venting valve, FVB 010, Pfeiffer Vacuum
Valve 2	Manual venting valve, SS-4H, Swagelok
Valve 3	Gate valve, Mini UHV gate valve 010, VAT
Valve 4	Pneumatic angle valve (safety valve), EVB 040, Pfeiffer Vacuum
Valve 5	Pneumatic angle valve (safety valve), EVB 040, Pfeiffer Vacuum
Valve 6	Valve, 1/4" tube, SS-4P4T, Swagelok
Valve 7	Valve, 1/4" tube, SS-4P4T, Swagelok

APPENDIX B

LabVIEW

On the following pages screen shots of the LabVIEW code for the data acquisition (Frame) and image analysis (Centroid14) is presented. Due to the size of the data acquisition program the screen shot has been cut into three parts.

The Frame program first has an initialization part where the camera and all needed parameters are initialized (Fig. B.1), after this the main part of the program is run (Fig. B.2 and Fig. B.3). This part is divided into two, a graphical user interface (GUI) where all parameters can be set and an acquisition part. In the acquisition part a delay stage, controlling the relative timing of the laser pulses, first moves to the desired position, then the selected number of frames are acquired and analyzed (Fig. B.4) and finally the found ion impact coordinates are stored together with a log file. If selected, the delay stage automatically moves to a new position and the acquisition cycle repeats itself, otherwise the program returns to the GUI where new parameters can be entered.

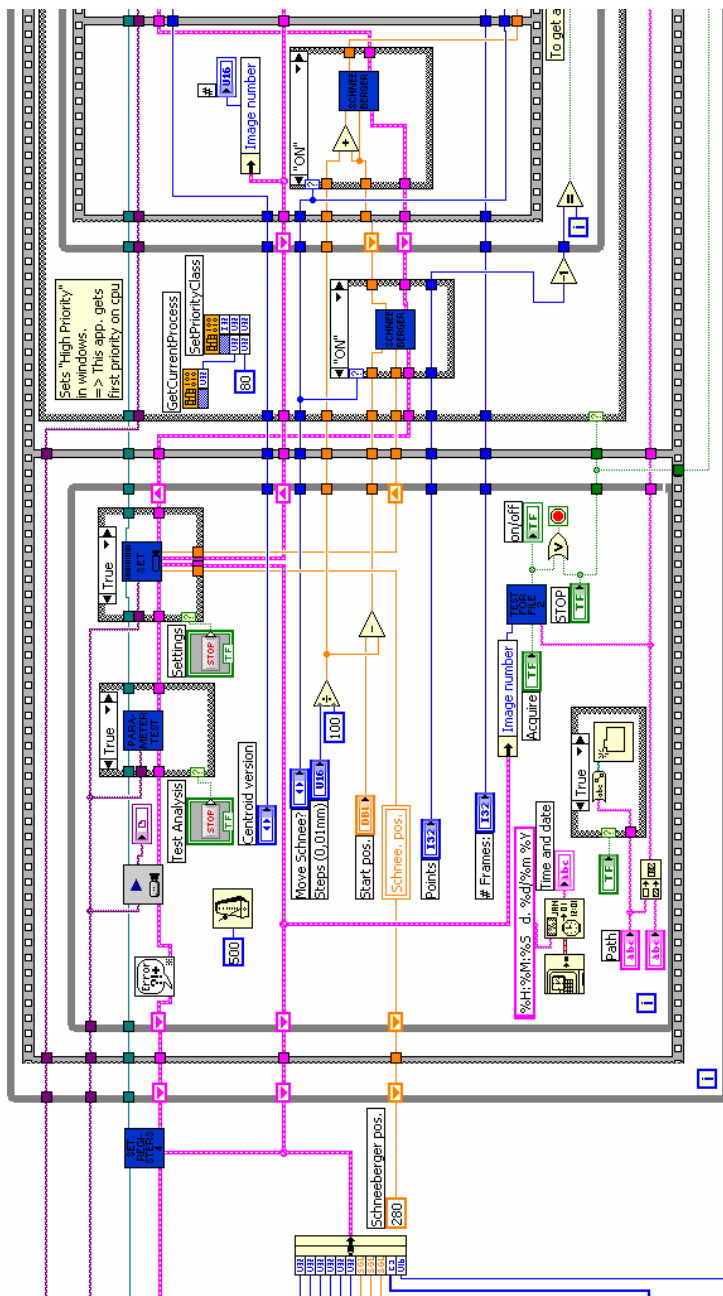


Figure B.2: Frame part B.

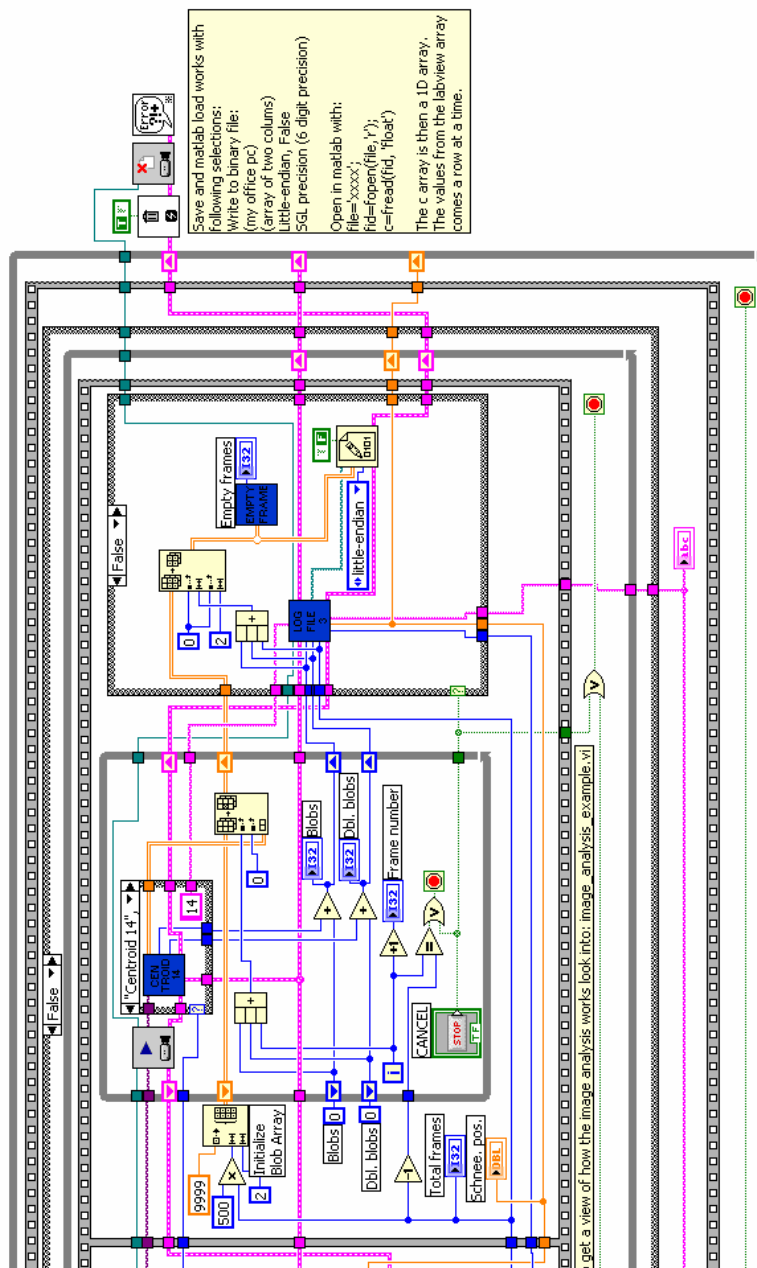


Figure B.3: Frame part C.

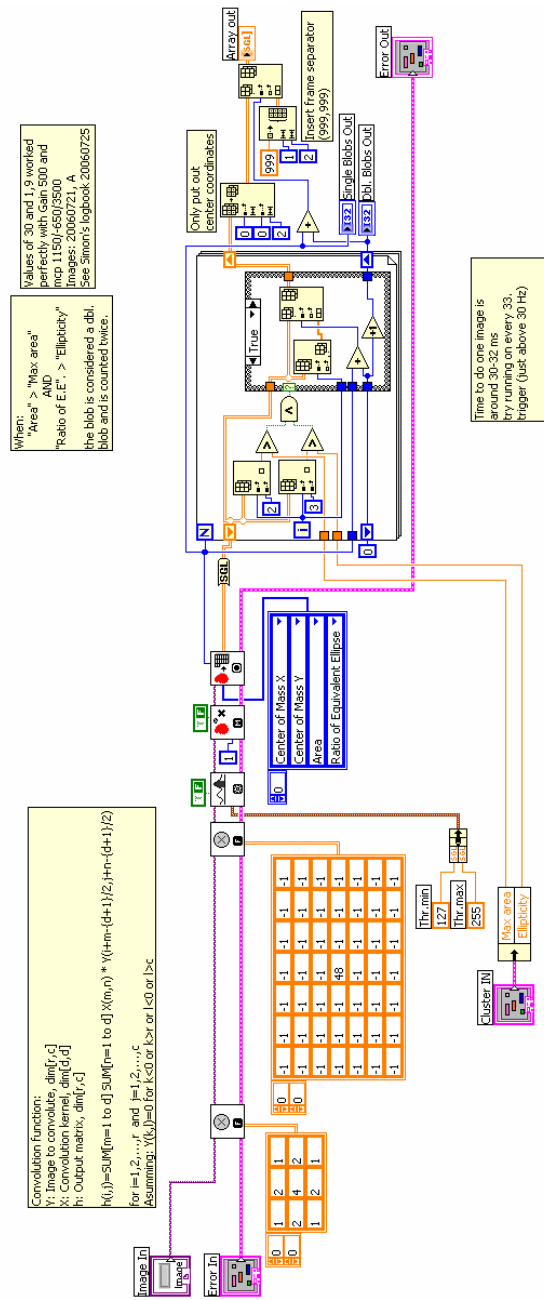


Figure B.4: Centroid 14.

APPENDIX C

Determination of the rotational constants of 3,5-difluoroiodobenzene

In rotational coherence spectroscopy rotational revivals, similar to the ones we record in nonadiabatic alignment, are used for determining the rotational constants of molecules. As shown in Chapter 4 the time separation of the C -type (t_C) and the J -type (t_J) revivals correspond well to the expected for iodobenzene [35]:

$$t_C = (4C)^{-1} \quad (\text{C.1})$$

$$t_J \leq \left(2(B + C) + \frac{(C - B)^2}{2A - B - C} \right)^{-1} \quad (\text{C.2})$$

$$t_J \sim (2(B + C))^{-1} \quad (\text{C.3})$$

We found that as the fluence was increased the time separation of the J -type revivals approached the expected value from Eq. (C.2). From similar experiments on 3,5-difluoroiodobenzene we hope to be able to extract the B and C rotational constants.

When writing up the principal moments of inertia for a planar object it is simple to see that $I_c = I_a + I_b$, where $I_a < I_b < I_c$ by definition. Since 3,5-difluoroiodobenzene is planar and the rotational constants are inversely proportional to the moments of inertia any rotational constant can be calculated from the other two, in particular:

$$A = \frac{C \cdot B}{B - C} \quad (\text{C.4})$$

With these equations and the time separation of the C -type and J -type revivals at hand we are able to calculate an estimate for the rotational constants. The experimentally observed distances between the first and second full revivals of 3,5-difluoriodobenzene are summarized in Table C.1. We see that the distance between the two C -type revivals remain constant while the distance between the J -type revivals increase with increasing fluence. Just as for iodobenzene a saturation effect is seen in the J -type revival distance and we assume that $t_J = 578$ ps will be good for estimating the rotational constants.

Fluence [J/cm^2]	C -type distance (t_C)	J -type distance (t_J)
0.81	660 ps	572 ps
1.6	660 ps	575 ps
3.2	660 ps	577 ps
14.2	660 ps	578 ps

Table C.1: Measured distances between subsequent revivals of C -type and J -type respectively, recorded at different fluences of the kick pulse.

We determined the rotational constants by calculating C from the C -type revival [Eq. (C.1)] and then B^* from the J -type revival using the approximate expression [Eq. (C.3)]. Through the moment of inertia relation [Eq. (C.4)] a first guess for A^* was found. This A^* value was then used together with full expression for the J -type revival [Eq. (C.2)] to calculate B . Finally A was found in the same manner as before. The computed values are presented in Table C.2 including uncertainties, estimated from the accuracy in the measurement of the revival distances (± 1 ps).

Rotational constant	Value [MHz]	Uncertainty [MHz]
C	378.79	
B^*	486.26	
A^*	1713.78	
B	484	± 2
A	1740	± 20
C	379	± 1

Table C.2: Rotational constants calculated from the revival distances in Table C.1.

BIBLIOGRAPHY

- [1] D. H. Parker and R. B. Bernstein, *Oriented molecule beams via the electrostatic hexapole: Preparation, characterization, and reactive scattering*, *Ann. Rev. Phys. Chem.* **40** (1989), 561–595.
- [2] B. Friedrich, D. P. Pullman, and D. R. Herschbach, *Alignment and orientation of rotationally cool molecules*, *J. Phys. Chem.* **95** (1991), 8118.
- [3] H. J. Loesch and A. Remscheid, *Brute force in molecular reaction dynamics: A novel technique for measuring steric effects*, *J. Chem. Phys.* **93** (1990), 4779.
- [4] B. Friedrich and D. Herschbach, *Alignment and trapping of molecules in intense laser fields*, *Phys. Rev. Lett.* **74** (1995), 4623.
- [5] T. Seideman, *Rotational excitation and molecular alignment in intense laser fields*, *J. Chem. Phys.* **103** (1995), 7887.
- [6] T. Seideman and E. Hamilton, *Nonadiabatic alignment by intense pulses. Concepts, theory, and directions*, *Adv. At., Mol., Opt. Phys.* **52** (2006), 289.
- [7] H. Stapelfeldt and T. Seidemann, *Colloquium: Aligning molecules with strong laser pulses*, *Rev. Mod. Phys.* **75** (2003), 543.
- [8] J. C. H. Spence and R. B. Doak, *Single molecule diffraction*, *Phys. Rev. Lett.* **92** (2004), 198102.
- [9] J. Itatani, J. Levesque, D. Zeidler, H. Niikura, H. Pépin, J. C. Kieffer, P. B. Corkum, and D. M. Villeneuve, *Tomographic imaging of molecular orbitals*, *Nature* **432** (2004), 867.

- [10] N. L. Wagner, A. Wuest, I. P. Christov, T. Popmintchev, X. Zhou, M. M. Murnane, and H. C. Kapteyn, *Inaugural Article: Monitoring molecular dynamics using coherent electrons from high harmonic generation*, PNAS **103** (2006), 13279–13285.
- [11] T. Kanai, S. Minemoto, and H. Sakai, *Quantum interference during high-order harmonic generation from aligned molecules*, Nature **435** (2005), 470.
- [12] C. Vozzi, F. Calegari, E. Benedetti, J.-P. Caumes, G. Sansone, S. Stagira, M. Nisoli, R. Torres, E. Heesel, N. Kajumba, J. P. Marangos, C. Altucci, and R. Velotta, *Controlling two-center interference in molecular high harmonic generation*, Phys. Rev. Lett. **95** (2005), 153902.
- [13] K. Hoki, D. Kroner, and J. Manz, *Selective preparation of enantiomers from a racemate by laser pulses: model simulation for oriented atropisomers with coupled rotations and torsions*, Chemical Physics **267** (2001), 59 – 79.
- [14] O. Gessner, A. M. D. Lee, J. P. Shaffer, H. Reisler, S. V. Levchenko, A. I. Krylov, J. G. Underwood, H. Shi, A. L. L. East, D. M. Wardlaw, E. t. H. Chrysostom, C. C. Hayden, and A. Stolow, *Femtosecond multidimensional imaging of a molecular dissociation*, Science **311** (2006), 219.
- [15] V. Bingelyte, J. Leach, J. Courtial, and M. Padgett, *Optically controlled three-dimensional rotation of microscopic objects*, Appl. Phys. Lett. **82** (2003), 829 – 831.
- [16] T. Seideman, *Revival structure of aligned rotational wave packets*, Phys. Rev. Lett. **83** (1999), 4971.
- [17] M. Poulsen, E. Peronne, H. Stapelfeldt, C. Bisgaard, S. Viftrup, E. Hamilton, and T. Seideman, *Nonadiabatic alignment of asymmetric top molecules: Rotational revivals*, J. Chem. Phys. **121** (2004), 783 – 791.
- [18] E. Hamilton, T. Seideman, T. Ejdrup, M. Poulsen, C. Bisgaard, S. Viftrup, and H. Stapelfeldt, *Alignment of symmetric top molecules by short laser pulses*, Phys. Rev. A **72** (2005), 043402.
- [19] M. Leibscher, I. S. Averbukh, and H. Rabitz, *Enhanced molecular alignment by short laser pulses*, Phys. Rev. A **69** (2004), 013402.
- [20] C. Bisgaard, M. Poulsen, E. Peronne, S. Viftrup, and H. Stapelfeldt, *Observation of enhanced field-free molecular alignment by two laser pulses*, Phys. Rev. Lett. **92** (2004), 173004.
- [21] C. Bisgaard, S. Viftrup, and H. Stapelfeldt, *Alignment enhancement of a symmetric top molecule by two short laser pulses*, Phys. Rev. A **73** (2006), 053410.

- [22] L. Holmegaard, S. Viftrup, V. Kumarappan, C. Bisgaard, H. Stapelfeldt, E. Hamilton, and T. Seideman, *Control of rotational wave-packet dynamics in asymmetric top molecules*, Phys. Rev. A **75** (2007), 051403.
- [23] D. J. Griffiths, *Introduction to Quantum Mechanics*, Prentice Hall, 1995.
- [24] J. Ortigoso, M. Rodríguez, M. Gupta, and B. Friedrich, *Time evolution of pendular states created by the intereaction of molecular polarizability with a pulsed nonresonant laser field*, J. Chem. Phys. **110** (1999), 3870–3875.
- [25] R. Torres, R. de Nalda, and J. P. Marangos, *Dynamics of laser-induced molecular alignment in the impulsive and adiabatic regimes: A direct comparison*, Phys. Rev. A **72** (2005), 023420.
- [26] B. Friedrich and D. Herschbach, *Polarization of molecules induced by intense nonresonant laser fields*, J. Chem. Phys. **99** (1995), 15686.
- [27] R. N. Zare, *Angular Momentum*, Wiley-Interscience, New York, 1988.
- [28] M. D. Poulsen, *Alignment of molecules induced by long and short laser pulses*, PhD thesis, Department of Chemistry, University of Aarhus, 2005.
- [29] V. Kumarappan, C. Bisgaard, S. Viftrup, L. Holmegaard, and H. Stapelfeldt, *Role of rotational temperature in adiabatic molecular alignment*, J. Chem. Phys. **125** (2006), 194309.
- [30] J. J. Larsen, *Laser Induced Alignment of Neutral Molecules*, PhD thesis, Institute of Physics and Astronomy, University of Aarhus, 2000.
- [31] I. S. Averbukh and R. Arvieu, *Angular focusing, squeezing, and rainbow formation in a strongly driven quantum rotor*, Phys. Rev. Lett. **87** (2001), 163601.
- [32] M. Leibscher, I. S. Averbukh, and H. Rabitz, *Molecular alignment by trains of short laser pulses*, Phys. Rev. Lett. **90** (2003), 213001.
- [33] C. Z. Bisgaard, *Laser Induced Alignment, Towards Fixed-In-Space Molecules*, PhD thesis, Institute of Physics and Astronomy, University of Aarhus, Denmark, 2006.
- [34] P. Felker, *Rotational coherence spectroscopy: studies of the geometries of large gas-phase species by picosecond time-domain methods*, J. Phys. Chem. **96** (1992), 7844.
- [35] P. M. Felker and A. H. Zewail, *Molecular structures from ultrafast coherence spectroscopy*, in *Femtosecond Chemistry*, J. Manz and L. Wöste, eds., VCH (Weinheim), 1995, pp. 193–260.

- [36] G. Scoles, ed., *Atomic and molecular beam methods*, Vol. I, Oxford University Press, 1988.
- [37] U. Even, J. Jortner, D. Noy, N. Lavie, and C. Cossant-Magos, *Cooling of large molecules below 1 K and He clusters formation*, J. Chem. Phys. **112** (2000), 8068.
- [38] M. Hillenkamp, S. Keinan, and U. Even, *Condensation limited cooling in supersonic expansions*, J. Chem. Phys. **118** (2003), 8699.
- [39] A. Eppink and D. Parker, *Velocity map imaging of ions and electrons using electrostatic lenses: Application in photoelectron and photofragment ion imaging of molecular oxygen*, Rev. Sci. Instrum. **68** (1997), 3477 – 3484.
- [40] S. Backus, C. G. Durfee, M. M. Murnane, and H. C. Kepteyn, *High power ultrafast lasers*, Rev. Sci. Instrum. **69** (1998), 1207–1223.
- [41] L. Holmegaard *Control of alignment dynamics of asymmetric top molecules*, Master's thesis, Department of Chemistry, University of Aarhus, 2006.
- [42] J. Olsen *Generation of sub 20 femtosecond laser pulses and coulomb explosion studies of D₂*, Master's thesis, Department of Chemistry, University of Aarhus, 1999.
- [43] J. E. Freitas, H. J. Hwang, and M. A. El-Sayed, *Molecular rotation clocking of the subpicosecond energy redistribution in molecules falling apart. 2. excess energy dependence of the rates of energy redistribution in the two photodissociation channels of iodobenzene*, J. Phys. Chem. **97** (1993), 12481.
- [44] E. Péronne, M. D. Poulsen, H. Stapelfeldt, C. Z. Bisgaard, E. Hamilton, and T. Seideman, *Nonadiabatic laser-induced alignment of iodobenzene molecules*, Phys. Rev. A **70** (2004), 63410.
- [45] M. J. J. Vrakking, *An iterative procedure for the inversion of two-dimensional ion/photoelectron imaging experiments*, Rev. Sci. Instrum. **72** (2001), 4084.
- [46] M. D. Poulsen, E. Skovsen, and H. Stapelfeldt, *Photodissociation of laser aligned iodobenzene: Towards selective photoexcitation*, J. Chem. Phys. **117** (2002), 2097.
- [47] S. S. Viftrup *New imaging, image analysis and control programs*, private communication, 2007.
- [48] W. J. O. Thomas, J. T. Cox, and W. Gordy, *Millimeter wave spectra and centrifugal stretching constants of the methyl halides*, J. Chem. Phys. **22** (1954), 1718.

- [49] F. Rosca-Pruna and M. J. J. Vrakking, *Revival structures in picosecond laser-induced alignment of I_2 molecules. I. Experimental results*, J. Chem. Phys. **116** (2002), 6567.
- [50] V. Kumarappan, S. Viftrup, L. Holmegaard, C. Bisgaard, and H. Stapelfeldt, *Aligning molecules with long or short laser pulses*, accepted by Physica Scripta.
- [51] P. W. Dooley, I. V. Litvinyuk, K. F. Lee, D. M. Rayner, M. Spanner, D. M. Villeneuve, and P. B. Corkum, *Direct imaging of rotational wave-packet dynamics of diatomic molecules*, Phys. Rev. A **68** (2003), 023406.
- [52] B. J. Sussman, J. G. Underwood, R. Lausten, M. Y. Ivanov, and A. Stolow, *Quantum control via the dynamic stark effect: Application to switched rotational wave packets and molecular axis alignment*, Phys. Rev. A **73** (2006), 053403.
- [53] J. J. Larsen, H. Sakai, C. P. Safvan, I. Wendt-Larsen, and H. Stapelfeldt, *Aligning molecules with intense nonresonant laser fields*, J. Chem. Phys. **111** (1999), 7774.
- [54] T. Seideman, *On the dynamics of rotationally broad, spatially aligned wave packets*, J. Chem. Phys. **115** (2001), 5965.
- [55] A. M. Mirri and W. Caminati, *Quadrupole hyperfine structure in the rotational spectrum of iodobenzene*, Chem. Phys. Lett. **8** (1971), 409–412.
- [56] A. Rouzée, S. Guérin, V. Boudon, B. Lavorel, and O. Faucher, *Field-free one-dimensional alignment of ethylene molecule*, Phys. Rev. A **73** (2006), 033418.
- [57] W. Kim and P. M. Felker, *Spectroscopy of pendular states in optical-field-aligned species*, J. Chem. Phys. **104** (1996), 1147.
- [58] H. Sakai, C. P. Safvan, J. J. Larsen, K. M. Hilligsøe, K. Hald, and H. Stapelfeldt, *Controlling the alignment of neutral molecules by a strong laser field*, J. Chem. Phys. **110** (1999), 10235.
- [59] J. J. Larsen, K. Hald, N. Bjerre, H. Stapelfeldt, and T. Seideman, *Three dimensional alignment of molecules using elliptically polarized laser fields*, Phys. Rev. Lett. **85** (2000), 2470–2473.
- [60] F. Rosca-Pruna and M. J. J. Vrakking, *Experimental observation of revival structures in picosecond laser-induced alignment of I_2* , Phys. Rev. Lett. **87** (2001), 153902.
- [61] R. Velotta, N. Hay, M. B. Mason, M. Castillejo, and J. P. Marangos, *High-order harmonic generation in aligned molecules*, Phys. Rev. Lett. **87** (2001), 183901.

- [62] R. A. Bartels, T. C. Weinacht, N. Wagner, M. Baertschy, C. H. Greene, M. M. Murnane, and H. C. Kapteyn, *Phase modulation of ultrashort light pulses using molecular rotational wave packets*, Phys. Rev. Lett. **88** (2002), 013903.
- [63] H. Tanji, S. Minemoto, and H. Sakai, *Three-dimensional molecular orientation with combined electrostatic and elliptically polarized laser fields*, Phys. Rev. A **72** (2005), 063401.
- [64] J. Underwood, B. Sussman, and A. Stolow, *Field-free three dimensional molecular axis alignment*, Phys. Rev. Lett. **94** (2005), 143002.
- [65] K. Lee, D. Villeneuve, P. Corkum, A. Stolow, and J. Underwood, *Field-free three-dimensional alignment of polyatomic molecules*, Phys. Rev. Lett. **97** (2006), 173001.
- [66] E. Constant, H. Stapelfeldt, and P. B. Corkum, *Observation of enhanced ionization of molecular ions in intense laser fields*, Phys. Rev. Lett. **76** (1996), 4140.
- [67] T. Seideman, M. Y. Ivanov, and P. B. Corkum, *Role of electron localization in intense-field molecular ionization*, Phys. Rev. Lett. **75** (1995), 2819.
- [68] P. Joireman, L. Connell, S. Ohline, and P. Felker, *Characterization of asymmetry transients in rotational coherence spectroscopy*, J. Chem. Phys. **96** (1992), 4118 – 4130.
- [69] M. D. Poulsen, T. Ejdrup, H. Stapelfeldt, E. Hamilton, and T. Seideman, *Alignment enhancement by the combination of a short and a long laser pulse*, Phys. Rev. A **73** (2006), 033405.
- [70] J. G. Underwood, M. Spanner, M. Y. Ivanov, J. Mottershead, B. J. Sussman, and A. Stolow, *Switched wave packets: A route to nonperturbative quantum control*, Phys. Rev. Lett. **90** (2003), 223001.
- [71] F. Grein, *Twist angles and rotational energy barriers of biphenyl and substituted biphenyls*, J. Phys. Chem. A **106** (2002), 3823 – 3827.
- [72] J. Seminario, A. Zacarias, and J. Tour, *Theoretical interpretation of conductivity measurements of a thiotolane sandwich. a molecular scale electronic controller*, J. Am. Chem. Soc. **120** (1998), 3970 – 3974.
- [73] L. Bumm, J. Arnold, M. Cygan, T. Dunbar, T. Burgin, L. Jones, D. Allara, J. Tour, and P. Weiss, *Are single molecular wires conducting?*, SCIENCE **271** (1996), 1705 – 1707.

- [74] J. Tour, M. Kozaki, and J. Seminario, *Molecular scale electronics: A synthetic/computational approach to digital computing*, J. Am. Chem. Soc. **120** (1998), 8486 – 8493.